Study of Nitrogen-Vacancy Centers in Diamond Schottky Diode by Optical Detection Magnetic Resonance

Muhammad Hafiz bin Abu Bakar

October 2022

Study of Nitrogen-Vacancy Centers in Diamond Schottky Diode by Optical Detection Magnetic Resonance

Muhammad Hafiz bin Abu Bakar

Doctoral Program in Applied Physics

Submitted to the Graduate School of
Pure and Applied Sciences
in Partial Fulfillment of the Requirements
for the Degree of Doctor of Philosophy in
Engineering

at the
University of Tsukuba

Abstract

Nitrogen vacancy (NV) centers in diamonds are attractive and promising candidates as solid-state systems for broad applications. The NV centers can be implanted in a sensitive nanoscale sensor to detect small system change such as a weak magnetic field, electric field, and temperature. Quantum computing based on NV centers also gained interest in research because of its outstanding properties such as extremely long-spin coherence times at room temperature. Because it solid-state-based material, the NV center can be fabricated closed with other NV centers or coupled to proximal ^{13}C, forming a small quantum-register. NV center can exist in two states, a neutral nitrogen-vacancy (NV^0) and negatively charged nitrogen-vacancy (NV^-). However, all the applications mentioned above require a NV^- because its electron spin state can be manipulated and read using an optical methods. For the NV^- to be used in practical applications, it should be located near the material surface for easy manipulation and readout, but this cause uncontrollable interconversion between NV^0 and NV^- due to several factors such as surface band-bending, surface defects and laser illumination.

To tackle this problem, the electrical control of the polarities of NV centers using diamond solid-state devices is proposed. The polarities of NV centers implanted into diamond solid-state devices (devices active layer) can be converted to NV^- or NV^0 by the injected (or depleted) holes in the active layer of the devices. Moreover, this electrical control structure opens a new possibility of integrating diamond devices based on NV centers into electronic control circuitry. This study investigates, the photoionization dynamics and spin state of the NV center polarity inside the depletion region of the Schottky diode are being investigated using photoluminescence and optically detected magnetic resonance (OMDR) techniques.

For sample preparation, p-type vertical diamond Schottky diode (VDSDs) were fabricated on a highly conductive $3 \times 3 \times 0.7$ mm^3 high-pressure high-temperature (HPHT) IIb diamond substrate (001). A nitrogen ion was then implanted in the epitaxial layer with an energy of 80 keV and implantation depth of 100 nm. The sample was annealed at 600°C to fabricate NV centers. Finally, optically transparent 10-nanometer-thick Molybdenum (Mo) Schottky electrodes (300-μm in diameter) were fabricated on the top side of the sample.

The ODMR characterization was performed using a homemade confocal microscope system. The hardware consisted of three main components. First, an optical excitation that uses a 532 nm laser generated by a pumped solid-state laser (Nd:YVO4 diode). Second, the PL was detected by ANDOR charged-coupled device camera. And third, a microwave signal was generated by using R&S SMB100A with a maximum output power of 25 dBm. The CCD camera and the microwave generator instruments were controlled by LabVIEW software that was developed in-house. The microwave signal was delivered to the sample by using copper wire that was soldered onto the printed circuit board.

measurement was done on a 1B diamond substrate. ODMR spectrum was observed with a resonance frequency dip at 2.87 GHz as shown in fig. 1 (b). The observation of this resonance dip shows that the home-built system can function well. The system is run by using continuous wave (CW) mode.

The target area of measurement was the NV center located below the semi-transparent Mo electrode because this is where the NV center is directly under influence of the electric field. At 0 V condition, both NV^0 and NV^- photoluminescence (PL) appear at the same measurement location. Upon applying $Vr > 0$, the NV^0 PL and its PBS spectrum decreased while the NV^- ZPL and its PBS increased steadily. This conversion was related to the shift of the Fermi level towards the NV^- energy transition level, thus leading to the ionization of NV^0 into NV^-. An ODMR measurement at the same location where the PL measurement was taken. Under high Vr, the ODMR contrast increased, and two distinct resonance dips were observed. Moreover, the resonance contrast was related to the NV^- PL intensitity. The ODMR spectrums exhibited resonance dips for $Vr \geq 10$ V. The existence of these two resonance dips was ascribed to the Stark effect since no magnetic field was applied during the ODMR measurements. the increase of the Vr and so the internal electric field of diamond Schottky diodes enhanced the Stark Effect thus leading to the splitting of the ODMR dip. On the other hand, the width of the splitting increased with Vr**.** The electric field calculated from the Stark effect has a slight value compared to the electric field calculated from the CV measurement.

It is also interesting to study the effect of electric fields on NV centers at low temperatures. For this experiment, the sample needs to be placed inside the small cryostat. But the problem is normal wire-type antenna cannot be used inside the cryostat since the wiring system inside the cryostat will reduce the MW power to the sample. Thus, a new microwave delivery system is needed. With the help of a colleague, the new type of MW delivery system was designed by using the combination of the microwave antenna and resonator. The concept is MW signal is delivered from the antenna that was placed outside of the cryostat and the signal will be coupled to the resonator that was placed inside the cryostat which is an LC circuit. The MW radiation is the strongest in proximity to the antenna and makes the MW coupling to the resonator much stronger. When the $Vr = 20V$ is applied, the NV^- PL characteristic is enhanced much more. The ODMR is performed at low temperatures but there is no resonance spectrum is observed even though the signal is enhanced by applying Vr. Several reasons are that compared to the 1B substrate, the number of NV center in the diode is much lower and the luminesce is covered by noise. Other factors such as the metal electrode somehow interfere with the distribution of the MW radiation near the NV center location.

In summary, we performed ODMR on nitrogen ion implanted VDSDs simple structure. Vertical type Schottky diode can control the NV center charge state and thin electrode design can allow excitation laser and PL signal to pass through. The vertical type also has several advantages such as effective usage of the device. The NV^0 is converted into NV^- at a higher bias thus contributing to more PL intensity. We observed ODMR splitting because of the electric field that exists inside the VDSDs depletion region. The estimated electric field value calculated from ODMR splitting show an almost

similar value to the C-V measurement. The small difference may be caused by the nitrogen and vacancy being diffused into deeper depths. We also performed PL and ODMR at low temperatures to study the effect of temperature. PL is enhanced at low temperatures, but we are unable to obtain the ODMR spectrum.

Table of Contents

Chapter 1

Introduction to Nitrogen-Vacancy Center in Diamond

1.1 Introduction

Quantum technologies have progressed in the last twenty years. These technologies are being developed by using quantum physics that utilizes quantum properties such as entanglement and superposition [1]. These properties can boost the processing speed to solve certain computational problems more efficiently than a typical classical computer [2]. Computing giants such as Google [3] and Microsoft [4] have invested in the development of quantum computing, transitioning from pure theoretical science to engineering. Google has begun research on the type of quantum computing that utilizes superconductivity. Conversely, Microsoft is exploring a new concept of topological quantum computing that uses Majorana fermion [5]. Companies that specialize in nanoelectronics and nanotechnology, such as IBM [6] and Intel [7], are also conducting research on building their quantum computers.

A quantum bit or "qubit" is a building block of quantum information, which is different from the bit of a classical computer. A classical computer stores information as bits that can be in two states, which are ground and excited states normally represented by "0" or "1". In contrast, a qubit can either be in the ground state, excited state, or both simultaneously[8]. A quantum computer operates based on the distinct properties of a qubit, "quantum superposition" and "quantum entanglement". Because the qubit can be in superposition, it enables a quantum computer to execute many calculations simultaneously, and for each additional qubit, the calculation is doubled leading to an exponential speed-up [9]. A famous physicist, Richard Feynman, proposed a method to harness quantum mechanics efficiently for simulating quantum systems. In his paper, published in 1982, he mentioned that it is difficult for classical computers to simulate quantum mechanical systems, and he suggested building a computer that uses a quantum mechanics principle to avoid those limitations Peter Shor proposed an algorithm, Shor's quantum algorithm, for factoring large numbers, which contributed toward development of quantum computers [11]. The quantum algorithm allows quantum computers to outperform the classical supercomputer by solving the integer-factorization problem in polynomial time, which is important for data encryption [12][13]. Like quantum computing, quantum metrology uses quantum mechanics, such as squeezing and entanglement to overcome the classical method. Nowadays, techniques for trapping, controlling, and counting neutral atom are advanced, and many experiments have successfully generated entangled states of trap ions and ultracold gases of these neutral atoms.

These atoms can be coupled to external fields and forces, which makes them suitable for ultrasensitive sensing and timekeeping [14]. The quantum technology has simplified measurements, making it useful in many important applications such as gravitational wave detection, remote sensing, temperature monitoring, magnetic field measurements, etc.[15].

For quantum computing or quantum metrology to be realized, quantum "hardware" needs to be developed. There are several ways to fabricate qubits. Certain quantum hardware operates using qubits that are made from the smallest form of matter such as ions of ytterbium or rubidium trapped in a vacuum chamber. There is also a system that uses a superconducting circuit that is cooled at millikelvin temperatures in a dilution refrigerator. Researchers have developed alternatives to quantum bit or "qubit" such as superconducting qubits [16], quantum dots [17], trapped ions [18], topologically protected systems [19], and colour centers [20]. Even though the quantum technology exhibits potential for improving computational power or high-sensitivity sensors, this technology still has some challenges. One of the main problems is that the quantum system has to operate in a low-temperature environment or vacuum to isolate the system from external noise that will affect the coherence time.

Diamond is believed to be a good alternative material for tackling this problem. Diamonds are normally used to produce jewelry. However, scientists and engineers discovered that diamonds can also be used as solid-state-based devices, owing to their extraordinary properties, such as high thermal conductivity and hardness. Diamonds consist of more than 500 color centers and these centers can be observed and addressed at room temperature [21]. Although they have more than 500 color centers, less than ten have been identified as bright, stable single-photon emitters such as nickel-related centers [22], silicon-related centers (SiV)[23], nitrogen-vacancy (NV) center [24], and chromium-related center [25]. The main strong point of NV centers is that the quantum processing can be operated at ambient temperature. In recent years, there has been progress in developing NV center-based quantum information processing (QIP). A study has successfully achieved electron spin coherence times that exceeded 1 ms at room temperature [26]. Additionally, the NV center was converted into an efficient single-photon source that can act like a qubit; optical and microwave qubit gate operation were also demonstrated using an optical readout [27][28]. Because a diamond is a solid-state material, many techniques have been proposed and developed to couple the NV center to optical microcavities [27][29] and waveguides [29]. The integrated photonic platform is desirable for QIP because of the interaction between optically entangled NV centers through optical microstructures. Optical/photonic nanosensors also benefit from the highly efficient performance of NV centers. NV centers are sensitive and can respond to the small perturbations near their surroundings, such as magnetic and electric fields, temperature, and pressure [30]. Because NV centers have the same size as atoms, a single NV center can be located in the sensor tip and be placed close to the sample to achieve magnetic surface mapping through the nanometric spatial resolution [31] [32]. Because the NV center is very sensitive to its surrounding, it can detect individual charges under ambient conditions [33]. Additionally, diamond is inert to the environment, and the NV centers in nanodiamonds are being used as markers for living cells.

1.2 Research motivation

All the applications mentioned above require a negatively charged nitrogen-vacancy (NV^-) center because its electron spin state can be manipulated and read using the optical method. For NV^- to be utilized in applications, it should be placed near the material surface for easy manipulation and readout, but this caused uncontrollable interconversion between NV^0 and NV^- due to several factors such as Ṅ, surface defects, and laser illumination [34][2].

To tackle this problem, the electrical control of the charge states of NV centers using diamond solid-state devices was established. The charge states of NV centers implanted into diamond solid-state devices (devices active layer) can be converted to NV^- or NV^0 by the injected (or depleted) holes in the active layer of the devices. This electrical control structure opens a new possibility of integrating diamond devices based on NV centers into electronic control circuitry. In this research, the photoionization dynamics, and the spin state of the polarities of NV centers inside the depletion region of the Schottky diode are investigated through photoluminescence and ODMR techniques.

1.3 Thesis overview

This thesis consists of five chapters.

Chapter 1 discusses a basic overview of the NV center

Chapter 2 2 explains the physical and electronic properties of the NV center in diamond and how it can be used as a building block for quantum applications. This chapter also discusses the reasons for the instabilities of the charge states of NV centers near the diamond surface.

Chapter 3 discusses the vertical diamond Schottky diode fabrication process and the development of an in-house optically detected magnetic resonance (ODMR) setup.

Chapter 4 discusses the electrical method used to control of charge states of NV centers. This chapter also demonstrates the determination of the charge states of the NV center and the spin state of NV^- through photoluminesce and ODMR measurements.

Chapter 5 explains the development of wireless microwave-signal transmission for low-temperature experiments.

1.4 References:

[1] A. Acín *et al.*, "The quantum technologies roadmap: A European community view," *New J. Phys.*, vol. 20, no. 8, 2018.

[2] C. Schreyvogel, V. Polyakov, R. Wunderlich, J. Meijer, and C. E. Nebel, "Active charge state control of single NV centres in diamond by in-plane Al-Schottky junctions," *Sci. Rep.*, vol. 5, pp. 1–12, 2015.

[3] F. Arute *et al.*, "Quantum supremacy using a programmable superconducting processor," *Nature*, vol. 574, no. 7779, pp. 505–510, 2019.

[4] S. Frolov, "Quantum computing's reproducibility crisis: Majorana fermions," *Nature*, vol. 592, no. 7854, pp. 350–352, 2021.

[5] C. Monroe, "Quantum computers ready," *Nat. News Focus News Focus*, 2017.

[6] Y. Wang, Y. Li, Z. qi Yin, and B. Zeng, "16-qubit IBM universal quantum computer can be fully entangled," *npj Quantum Inf.*, vol. 4, no. 1, pp. 1–6, 2018.

[7] L. Petit *et al.*, "Universal quantum logic in hot silicon qubits," *Nature*, vol. 580, no. 7803, pp. 355–359, 2020.

[8] F. Jazaeri, A. Beckers, A. Tajalli, and J. M. Sallese, "A Review on quantum computing: From qubits to front-end electronics and cryogenic mosfet physics," *Proc. 26th Int. Conf. "Mixed Des. Integr. Circuits Syst. Mix. 2019*, pp. 15–25, 2019.

[9] C. Monroe, "To Leap Out of the Lab," 2017.

[10] R. P. Feynman, "Simulating physics with computers," *Int. J. Theor. Phys.*, vol. 21, no. 6–7, pp. 467–488, 1982.

[11] P. W. Shor, "Polynomial-time algorithms for prime factorization and discrete logarithms on a quantum computer," *SIAM J. Comput.*, vol. 26, no. 5, pp. 1484–1509, 1997.

[12] M. Rossi *et al.*, "Using Shor's algorithm on near term Quantum computers: a reduced version," pp. 1–8, 2021.

[13] P. W. Shor, "Algorithms for quantum computation: Discrete logarithms and factoring," *Proc. - Annu. IEEE Symp. Found. Comput. Sci. FOCS*, pp. 124–134, 1994.

[14] L. Pezzè, A. Smerzi, M. K. Oberthaler, R. Schmied, and P. Treutlein, "Quantum metrology with nonclassical states of atomic ensembles," *Rev. Mod. Phys.*, vol. 90, no. 3, 2018.

[15] D. Braun *et al.*, "Quantum-enhanced measurements without entanglement," *Rev. Mod. Phys.*, vol. 90, no. 3, p. 35006, 2018.

[16] I. L. Chuang *et al.*, "Superconducting Circuits for Quantum," no. March, pp. 1169–1175, 2013.

[17] D. Kim *et al.*, "Microwave-driven coherent operation of a semiconductor quantum dot charge qubit," *Nat. Nanotechnol.*, vol. 10, no. 3, pp. 243–247, 2015.

[18] H. Levine *et al.*, "High-Fidelity Control and Entanglement of Rydberg-Atom Qubits," *Phys. Rev. Lett.*, vol. 121, no. 12, pp. 1–6, 2018.

[19] C. Nayak, S. H. Simon, A. Stern, M. Freedman, and S. Das Sarma, "Non-Abelian anyons and topological quantum computation," *Rev. Mod. Phys.*, vol. 80, no. 3, pp. 1083–1159, 2008.

[20] F. Jelezko and J. Wrachtrup, "Single defect centres in diamond: A review," *Phys. Status Solidi Appl. Mater. Sci.*, vol. 203, no. 13, pp. 3207–3225, 2006.

[21] I. Aharonovich, S. Castelletto, D. A. Simpson, C. H. Su, A. D. Greentree, and S. Prawer, "Diamond-based single-photon emitters," *Reports Prog. Phys.*, vol. 74, no. 7, 2011.

[22] T. Gaebel, I. Popa, A. Gruber, M. Domhan, F. Jelezko, and J. Wrachtrup, "Stable single-photon source in the near infrared," *New J. Phys.*, vol. 6, pp. 1–7, 2004.

[23] C. Wang, C. Kurtsiefer, H. Weinfurter, and B. Burchard, "Single photon emission from SiV centres in diamond produced by ion implantation," *J. Phys. B At. Mol. Opt. Phys.*, vol. 39, no. 1, pp. 37–41, 2006.

[24] F. Jelezko and J. Wrachtrup, "Single defect centres in diamond: A review," *Phys. Status Solidi Appl. Mater. Sci.*, vol. 203, no. 13, pp. 3207–3225, 2006.

[25] I. Aharonovich, S. Castelletto, D. A. Simpson, A. D. Greentree, and S. Prawer, "Photophysics of chromium-related diamond single-photon emitters," *Phys. Rev. A - At. Mol. Opt. Phys.*, vol. 81, no. 4, pp. 1–7, 2010.

[26] G. Balasubramanian *et al.*, "Ultralong spin coherence time in isotopically engineered diamond," *Nat. Mater.*, vol. 8, no. 5, pp. 383–387, 2009.

[27] K. G. Fehler, A. P. Ovvyan, N. Gruhler, W. H. P. Pernice, and A. Kubanek, "Efficient Coupling of an Ensemble of Nitrogen Vacancy Center to the Mode of a High-Q, Si3N4 Photonic Crystal Cavity," *ACS Nano*, 2019.

[28] F. T. Charnock and T. A. Kennedy, "Combined optical and microwave approach for performing quantum spin operations on the nitrogen-vacancy center in diamond," *Phys. Rev. B - Condens. Matter Mater. Phys.*, vol. 64, no. 4, pp. 1–4, 2001.

[29] J. Riedrich-Möller *et al.*, "One-and two-dimensional photonic crystal microcavities in single crystal diamond," *Nat. Nanotechnol.*, vol. 7, no. 1, pp. 69–74, 2012.

[30] A. M. Wojciechowski *et al.*, "Optical magnetometry based on nanodiamonds with nitrogen-vacancy color centers," *Materials (Basel).*, vol. 12, no. 18, pp. 1–10, 2019.

[31] K. Bian *et al.*, "Nanoscale electric-field imaging based on a quantum sensor and its charge-state control under ambient condition," *Nat. Commun.*, vol. 12, no. 1, pp. 1–9, 2021.

[32] P. Maletinsky *et al.*, "A robust scanning diamond sensor for nanoscale imaging with single nitrogen-vacancy centres," *Nat. Nanotechnol.*, vol. 7, no. 5, pp. 320–324, 2012.

[33] F. Dolde *et al.*, "Electric-field sensing using single diamond spins," *Nat. Phys.*, vol. 7, no. 6, pp. 459–463, 2011.

[34] H. Kato *et al.*, "Tunable light emission from nitrogen-vacancy centers in single crystal diamond PIN diodes," *Appl. Phys. Lett.*, vol. 102, no. 15, pp. 1–5, 2013.

Chapter 2

Nitrogen-vacancy center in diamond

2.1 Introduction

This chapter explains the basic properties of a diamond and the reason it is an excellent host for quantum applications. Subsequently, it explains the spin dynamics of the nitrogen-vacancy (NV) center and how it is manipulated. Finally, applications of NV centers are discussed.

2.2 Diamond as a host material

This chapter starts by explaining the properties of diamonds, diamond classification, and the type of impurities in a diamond lattice.

Natural diamonds are formed under extreme conditions at high pressures in a range of 70–80 kbar and high temperatures in a range of 1400–1600 °C [1]. These extreme conditions can be found at a depth of 200 km into the earth's core, and it takes more than one billion years for a natural diamond to form [2]. Owing to volcanic activity, diamonds formed at this depth are transported to the surface, and this makes it easier to mine them. At ambient pressure and temperature, graphite is the most stable form of carbon, and diamond is metastable [3]. Carbon atoms in diamond form tetrahedral shapes and are covalently bonded to four nearest neighbours to create a cubic crystal structure [4]. The diamond's strength comes from its strong covalent bond, which gives the diamond its hardness [1].

Another interesting characteristic of diamond is its high thermal conductivity at room temperature, compared to other materials. This high thermal conductivity is from a phonon. The thermal conductivity of diamonds at room temperature is 2200 W m^{-1} K^{-1}, which is five times more than that of copper, and because of this properties, diamonds are preferred in several applications such as mirrors for high-power lasers and for cutting tools [1][5]. Diamonds also have excellent optical properties. They possess a high refractive index of 2.4, which gives them their “brilliance” or “sparklines” [6]. They have a wide bandgap of is 5.5 eV, which makes them transparent to spectra below the ultraviolet spectrum [7].

2.3 Types of diamond

Diamonds are not always perfect because there are always impurities contained in the diamond crystal lattice. Depending on the type and concentration of the impurity, diamonds be classified into two types, type I and type II. This classification is based on the absorption in infrared spectroscopy measurements; type I have a high nitrogen concentration (hundreds or thousands of ppm) [8]. Depending on how the nitrogen forms in the lattice, type I can be further categorized into two subgroups, type Ia and Ib. Conversely, type II contains very low nitrogen atoms that cannot be detected in infrared spectroscopy measurements (less than 20 ppm)[9]. Like type I, type II diamonds can be further categorized into two subgroups. The details of the diamond classification are summarized in Table 2.1 [10].

Table 2.1 Diamond classification based on impurity type and concentration

Diamond types	
Type I Have a high nitrogen concentration (Hundreds or thousands of ppm)	Type Ia High nitrogen (N) atoms that tend to aggregate together Type Ib High nitrogen atoms in the lattice which become single substitutional N atoms
Type II Have a low nitrogen concentration (Less than 20 ppm)	Type IIa Low boron and nitrogen atoms which makes this form the purest diamond crystal Type IIb Low nitrogen but the boron concentration is very high

2.4 Diamond growth method

Normally, diamond is mined in the earth's crust, but with the current technology, it is possible to synthesize diamond in a laboratory. This manmade diamond is known as a synthetic diamond. The physical properties and the chemical structure of synthetic and natural diamonds are similar. The classification of natural diamonds, which was mentioned earlier, also applies to synthetic diamonds.

The earliest method for synthesizing diamonds was the high-pressure high-temperature method. However, recently, chemical vapor deposition (CVD) has been an effective way to produce diamonds. Both methods are described briefly.

2.4.1 High pressure high temperature (HPHT) method

Natural diamonds are formed from carbon under a harsh environmental conditions, which are extreme pressure and temperature in the earth's core. The first successful manmade diamond was produced in 1955 by Bundy *et al.* through the HPHT method. They successfully developed a chamber that achieved a maximum pressure of 100 000 kgm/cm^2 and a maximum temperature of 2000 °C [11]. In the HPHT method, diamond crystallization can proceed due to thermodynamic stability [11]. The main ingredient for HPHT growth is carbon sources such as graphite or diamond powder [12]. However, a synthetic diamond produced through the HPHT method produces a yellowish color, and it is classified as type Ib because high nitrogen impurities reach a concentration between 50–100 and 1000 ppm incorporated during the growth process [13]. The main source of nitrogen in the HPHT process was the presence of air pores in the cell during assembly.

2.4.2 Chemical vapor deposition (CVD) method

While the HPHT method simulates the earth's condition for crystal growth, the CVD method uses a different approach. The process is kinetically driven and not thermodynamically. The growth condition of the CVD method is lesser than that of the HPHT method, in which the pressure inside the chamber is approximately 20-30 Torr and the substrate temperature is in the range of 700–900 °C [14]. CVD requires a chemical reaction in the gas phase, generally methane and hydrogen, and deposition onto the substrate surface [8] [14]. The substrate can be bulk diamond, which is synthetic or natural diamond. For the reaction to happen, the gas that contains precursor molecules is heated until it becomes plasma. There are several methods for plasma generation, such as the thermal method (e.g. hot filament), electric discharge (e.g. DC, RF, or microwave), and combustion flame (oxyacetylene torch) [14].

The carbon atoms are mainly from methane [8] [15]. Moreover, atomic hydrogen plays several roles in the CVD method. First, during the bulk diamond crystal growth, the diamond surface contains a dangling bond that should be terminated. The reactive hydrogen atoms can make a bond with the dangling bonds to prevent any surface graphitization. Second, the hydrogen atoms can etch any graphitic structure that may form on the surface exposing the diamond cluster. Last, hydrogen atoms can stop the build-up of polymers in the gas phase, which can be deposited on the growing surface and inhibit diamond growth [14]. The CVD method can produce more pure diamonds than the HPHT method.

2.5 Nitrogen-vacancy center defect

The NV center is a promising material to be used in various applications because of its long coherent times at room temperature. The next subsection discusses the basic properties of the NV center that exist in the diamond host and spin dynamics regarding the spin manipulation and readout of the negatively charged NV (NV^-) center.

2.5.1 Atomic structure of the NV center

There is several colors that exist in a diamond lattice, but among them, the NV center exhibits promising properties such as a stable single-photon source and low toxicity. The diamond crystal structure consists of carbon atoms that are covalently bonded. However, sometimes imperfections can happen to the crystal structure, and certain carbon atoms can be replaced by atomic impurities such as nitrogen, boron, silicon, which can alter the diamond's properties. Nitrogen is a major component of the atmosphere, and it is also a common cause of defects in diamonds [1]. In the periodic table, the nitrogen atom belongs to group V, meaning that it has five valence electrons. When it replaces one carbon atom in the diamond lattice, it becomes an electron donor. This defect is known as the P1 center [2]. When a vacancy moves closer to the P1 center, the defects become NV color center, which is optically active. Three electrons from the nitrogen atom form a covalent bond with the nearest three carbon atoms while the remaining two electrons become lone pairs.

The NV center is a point defect that consists of a substitutional nitrogen atom and couples to an adjacent vacancy in the diamond lattice as shown in figure 2-1. This has a trigonal C_{3v} symmetry, meaning it can rotate for 120° along the nitrogen-vacancy axis, and it can have four different orientations along the crystallographic direction, which are [111], $[\bar{1}\bar{1}1]$, $[1\bar{1}\bar{1}]$, and $[\bar{1}1\bar{1}]$, as shown in figure 2-1. The NV center is constructed from four molecular orbitals (MOs) from a linear combination of the atomic orbitals that come from the nitrogen atom and three carbons atoms. The resulting MOs are represented by $a1'$, $a1$, e_x, and e_y levels [16][17]. The $a1'$ level is situated in the valence band and the other three MOs levels $a1$, e_x, and e_y are situated in the diamond bandgap as shown in figure 2-2. The MOs of the NV center are filled with the six electrons from the lowest to the highest energy level following Hund's rule. In the ground state of the NV center, $a1'$ and $a1$ levels are filled with four electrons while the other two unpaired electrons fill the degenerate e_x and e_y levels, respectively, and form a spin triplet S = 1. In the excitation state of the NV center, the $a1'$ level is not involved in the process. Only an electron from the $a1$ level can be promoted to either e_x or e_y levels, and only these levels are expected to show detectable properties of the NV center. The spin-to-spin interaction between the unpaired electrons results in the splitting of the ground triplet state at zero magnetic fields [18].

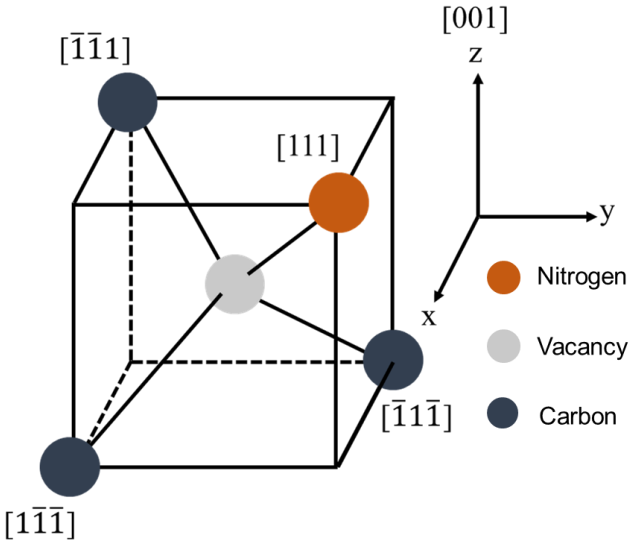

Figure 2-1. shows NV center axis orientation along four crystallographic axes which are [111], [$\bar{1}\bar{1}$1], [1$\bar{1}\bar{1}$] and [$\bar{1}$1$\bar{1}$].

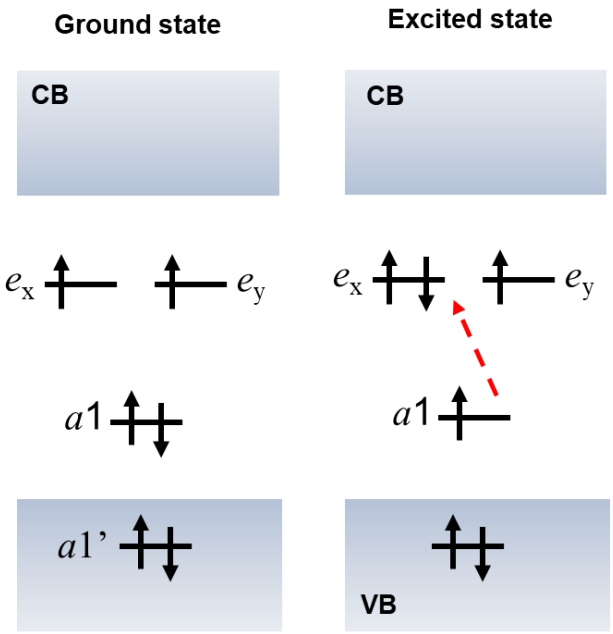

Figure 2-2. Axis orientation of the NV center along four crystallographic axes, [111], [$\bar{1}\bar{1}$1], [1$\bar{1}\bar{1}$], and [$\bar{1}$1$\bar{1}$].

Experimental data show that NV center defects can exist in two charge states, neutral (NV^0) and negatively charged (NV^-). The charge state is determined by the number of electrons surrounding this defect as shown in figure 2-3. NV^0 has 5 electrons, of which two are from nitrogen atoms and the

other three are from dangling carbon atoms. In this state, the electron has a total spin of S = ½, which is in the singlet state. When the NV^0 captures one electron from the lattice (from another P1 center), there will be six dangling electrons, and this will convert NV^0 to NV^-. For the NV^- state the electron has a total spin of S = 1, which is a spin triplet.

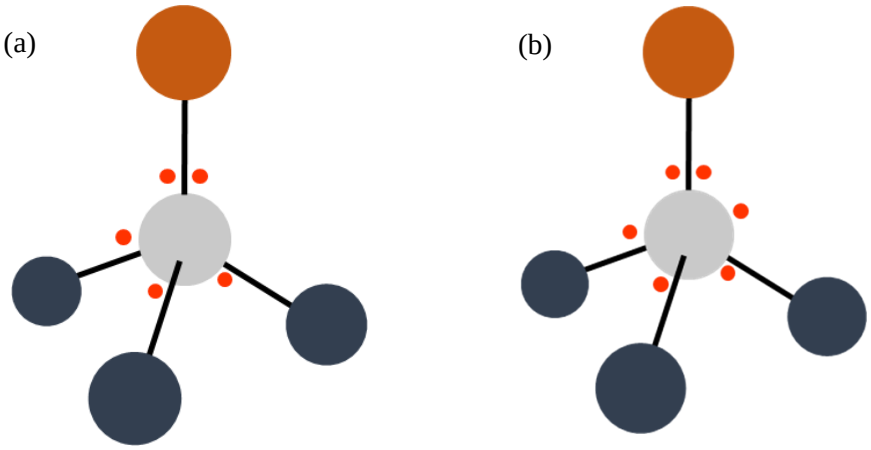

Figure 2-3 (a) NV^0 with five electrons and (b) NV^- with six electrons; the red circles are electrons, gray circle is the vacancy, and black circles are carbon atoms

2.5.2 Optical properties of the NV center

The NV^0 and NV^- states have an electronic structure like the atomic energy level. Both charge state energy levels reside in the diamond band gap (shown in figure 2-4 (a)) and exhibit a strong optical transition between ground and excited states. NV^0 has a (ZPL) at 575 nm (2.156 eV) while NV^- has a ZPL at 637 nm (1.945 eV). Figure 2-4 (b) shows a typical NV^0 and NV^- photoluminescence spectrum, and from the spectrum, only a small percentage is emitted into ZPL, and most of the photon is emitted into PBS. This contributes to a broad PL signal at room temperature. The most common excitation for both charge states is performed with a 532 nm laser.

The PL is emitted from a single NV center by using a confocal setup, and it is photostable at room temperature, compared to optically excited fluorophores, including dye molecules [19], and in nanomaterials such as quantum dots [20]. Because of this photostability, the NV center is a perfect candidate for the developing an efficient single-photon source.

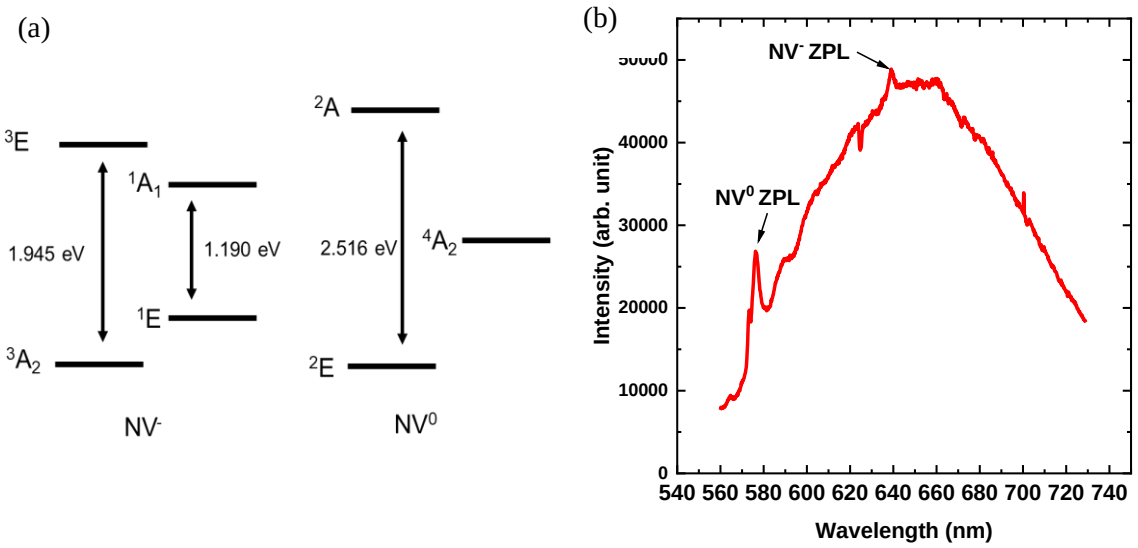

Figure 2-4 (a) Optical transition level of the NV center inside the diamond bandgap for NV^0 and NV^-. (b) PL spectrum showing NV^0 and NV^- ZPLs at 575 nm and 637 nm, respectively.

2.5.3 Spin properties

This section will explain the NV^- electronics levels. From figure 2-5, the NV^- electronic state consists of triplet ground and excited states, denoted as $^3A_2$ and ^3E, respectively [21]. Between the triplet ground and excited states, another intermediate metastable state, the singlet state, exists and it is denoted as ^1A and ^1E. The energy level diagrams of these states are represented in figure 3-3. The triplet state is represented by m_S, which is the projection of the spin along the quantization NV center axis, and it is split into three energy sublevels known as $m_S = \pm 1$ states, which are degenerate, and $m_S = 0$, which has a lower energy. Conversely, for the ground triplet state, the zero field splitting is $D_g \sim 2.87$ GHz between $m_S = 0$ and $m_S = \pm 1$ sublevels, and for the excited state, the zero field splitting is $D_g \sim 1.47$ GHz between the $m_S = 0$ and $m_S = \pm 1$ sublevel.

NV^- can be optically excited from the ground state to the excited state by using a suitable wavelength (for example 532 nm) [22]. From the excited state, NV^- can move directly to the ground state through the same radiative transition and simultaneously emit red photons. This direct transition between the ground state and excited state is spin-conserving, meaning that the spin state does not change during the transition. However, a second decay path also exists, which is the metastable singlet state. This state is nonradiative. These are the interesting properties that allow spin initialization and readout [23].

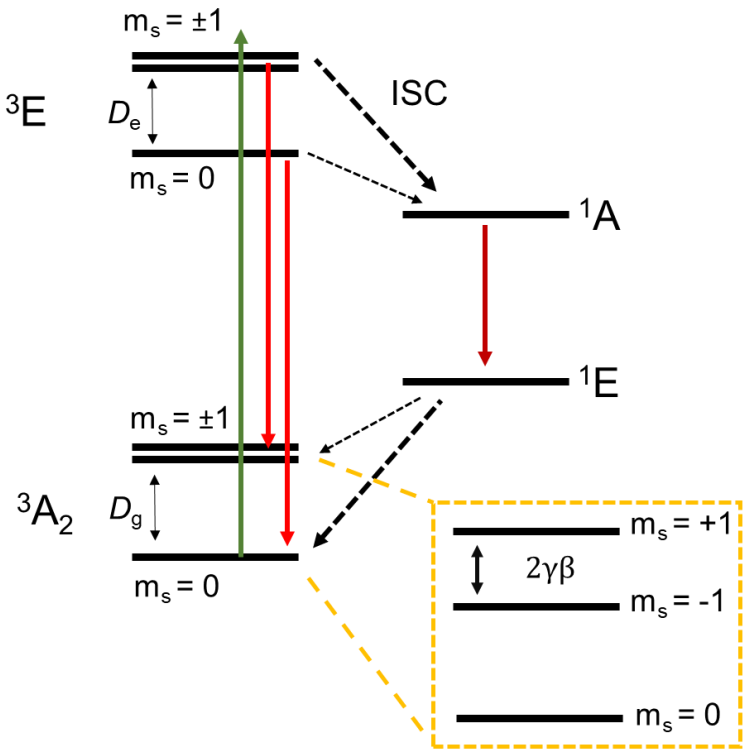

Figure 2-5 Details of the NV^- energy level scheme. The electron can be easily excited using a 532 nm laser (green arrow). From the excited state, the electron can move directly to the ground state (red arrow) or the singlet state using intersystem crossing (thick dash arrow).

When the MW frequency is off resonance, the electron in the $^3A_2$ $m_S = 0$ state is excited to the ^3E $m_S = 0$ state and relaxes radiatively back to the $^3A_2$ state, which are spin-conserving. If the microwave frequency resonates with the ground state ZFP, which is $D_g = 2.87$ GHz, the electron can be manipulated to be in-between $^3A_2$ $m_S = 0$ and $m_S = \pm1$ states. When the electron populates the $^3A_2$ $m_S = \pm1$ state, it will be excited to the ^3E $m_S = \pm1$ state, and from this sublevel, the electron will have a larger probability to decay to a nonradiative metastable singlet state through intersystem crossing (ISC), compared to ^3E $m_S = 0$ states [24]. This decay path is spin-selective, meaning the decays take a longer time resulting in fewer photons being emitted from the NV center. From this singlet state, the electron will decay to $^3A_2$ $m_S = 0$ states. By comparing the photon intensity during MW off and on resonances, the NV^- spin state can be determined, and this is the basic principle of ODMR. As mentioned before, the spin sublevels of the $m_S = \pm1$ state are degenerate, and this degeneracy can be lifted by applying a magnetic field. This will cause the $m_S = \pm1$ state to split and shift away in the opposite direction. The splitting will increase linearly with a stronger magnetic field, and this is the basis of magnetic sensing applications [24].

The changes in the NV center energy levels are explained by a mathematical equation known as the NV center Hamiltonian, which describes the total energy of the NV center. By disregarding the hyperfine interaction between the electronic spin and nearby nuclear spin in the lattice and choosing the quantization axis of the NV as the z-axis, the spin Hamiltonian of the ground triplet states of the NV center is written as follows [25]:

$$\hat{\mathrm{H}} = hDS_z^2 + hE\left(S_x^2 - S_y^2\right) + g\mu_B \boldsymbol{B} \cdot \boldsymbol{S} \qquad 3\text{-}1$$

where, z is the NV center quantization axis, $h = 6.626 \times 10^{-34}$ m^2 kg/s is the Planck constant, $D \approx 2.87$ GHz is the zero field splitting (ZFS) of the e_x and e_y MOs, E is the strain-induced splitting between the $m_s = \pm 1$ levels of the ground state triplet states, $g = 2.0$ is the Lande factor, μ_B is the Bohr magneton, $\boldsymbol{B}$ is the magnetic field applied to the NV center, and $S = (S_x, S_y,$ and $S_z)$ are the Pauli matrices for the spin = 1 operator. Their components are given as follows:

$$S_x = \frac{1}{\sqrt{2}}\begin{pmatrix} 0 & 1 & 0 \\ 1 & 0 & 1 \\ 0 & 1 & 0 \end{pmatrix} \quad S_y = \frac{1}{\sqrt{2}}\begin{pmatrix} 0 & -i & 0 \\ i & 0 & -i \\ 0 & i & 0 \end{pmatrix} \quad S_z = \begin{pmatrix} 1 & 0 & 0 \\ 0 & 0 & 0 \\ 0 & 0 & -1 \end{pmatrix} \qquad 3\text{-}2$$

The first term in the equation refers to the ZFS caused by the interaction between the spins of the two unpaired electrons of the e_x and e_y MOs. According to reference [26][27], the ZFS only happened for nonspherical spin densities. The ZFS has a bigger impact on the S_z spin component compared with S_x and S_y, which are only affected when the axial symmetry is broken by electric fields or transversal strain.

The last term refers to the interaction of the NV center with the external magnetic field $\boldsymbol{B}$. When the applied magnetic field is parallel to the NV center symmetry z-axis, the $m_s = \pm 1$ level will split linearly and the separation energy between $m_s = +1$ and $m_s = -1$ becomes $g\mu_B\boldsymbol{B}$, as shown in figure 2-6 (a). [27][28] According to reference [27][28] when $\boldsymbol{B} \approx 102$ mT. If $\boldsymbol{B}$ is not parallel to the NV center z-axis, the $m_s = \pm 1$ level splitting will not be linear, and the result will be depended on the angle between the NV z-axis and applied $\boldsymbol{B}$ (figure 2-6 (b)). there will be a level of anticrossing (LAC), at which the ZFS is compensated by the Zeeman shift and strong level mixing occurs.

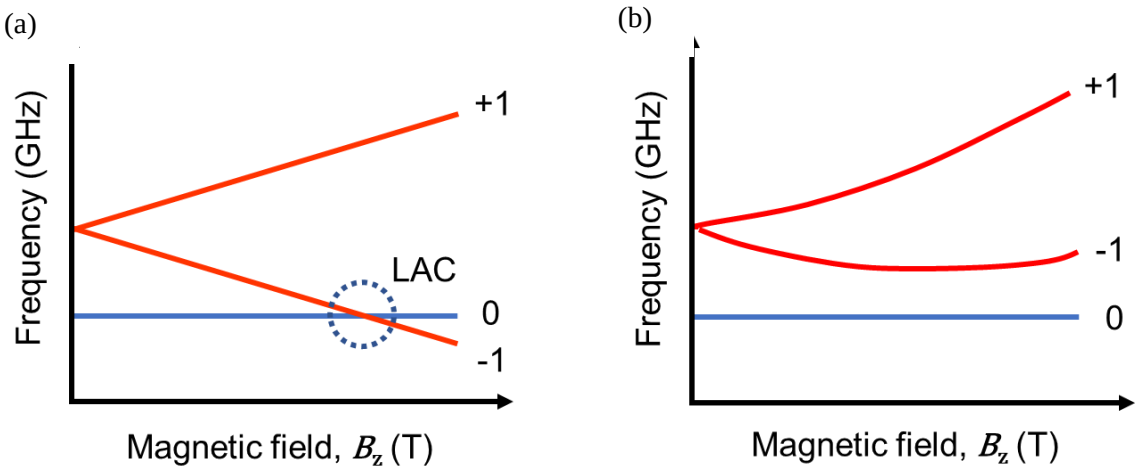

Figure 2-6 Splitting of the m_s = +1 and m_s = -1 ground state levels when the magnetic field is (a) parallel to NV center axis and (b) not parallel to the NV center axis.

The electric field is known to induce a shift in the optical resonance line for a single atom, the gas phase, and a single molecule and quantum dots in the solid state [29]. The NV center is also sensitive to electric fields. Like the Zeeman effect, when the NV center is subjugated to the electric field, m_s = ±1 will be split, and this phenomenon is known as the Stark effect. Several studies observed the Stark shift in the ground state of NV ensembles [30] and the excited triplet state of single defect centers [29][31]. The triplet state of the NV center-spin Hamiltonian under a magnetic field, strain, and the electric field is written as follows:

$$\hat{\mathrm{H}} = \left(hD_{gs} + d_{gs}^{\parallel}\Pi_z\right)\left[S_z^2 - \frac{1}{3}S(S+1)\right] + g_e\mu_B \boldsymbol{B}\cdot\boldsymbol{S} - d_{gs}^{\perp}\left[\Pi_X\left(S_xS_y - S_yS_x\right) + \Pi_y\left(S_x^2 - S_y^2\right)\right] \quad 3\text{-}3$$

where, $d_{gs}^{\parallel}$ = 0.35 ± 0.02 Hz cm V^{-1} and $d_{gs}^{\perp}/h$ = 17 ± Hz cm V^{-1} (ref) are the measured axial and nonaxial components of the ground triplet state's permanent electric dipole moment of d_{gs}, h is the Planck constant, μ_B is the Bohr magneton, g_e is the electron g-factor, $\boldsymbol{B}$ is the applied magnetic field, and $\boldsymbol{S}$ is the electron spin operator. Here, $\Pi = \mathrm{E} + \sigma$ is the total effective electric field experienced by the NV center, where the crystal strain σ inside the diamond can be considered a local static electric field, and E is the applied electric field. Like the Zeeman effect, the magnitude of the electric field affect the splitting width of the ODMR spectrum.

As mentioned in the previous subsection, the NV center can be used as a two-level system for quantum applications. The difference in the PL intensity when MW is applied can be used to determine the NV^- electron spin state. Rabi oscillation is a cyclic behavior of the two-level quantum system under the influence of an oscillatory driving field; if the system is prepared at one of these levels, the applied resonance microwave field will make the population oscillate between these two levels, and this is known as the Rabi frequency [32].

To perform Rabi measurements on the NV center, a magnetic field is applied along the NV center axis. This causes the $m_s = +1$ and $m_s = -1$ degeneracy to be lifted by the Zeeman effect. Subsequently, the transition between $m_s = 0 \leftrightarrow m_s = +1$ and $m_s = 0 \leftrightarrow m_s = -1$ will have their transition frequency depending on the magnitude of the applied magnetic field. When this happens, the system becomes a two-level system, also known as a qubit, and the electron spin can be represented as spin up $|0\rangle$ or spin down $|1\rangle$ [33]. A laser pulse is applied to prepare the NV^- center electron spin in the $m_s = 0$ states, then the laser is turned off. A microwave pulse is then applied for time τ. A second laser pulse is applied to probe the NV^- spin state. The microwave τ is varied and the NV^- spin state is read out for each τ. The duration of the applied microwave pulse will prepare the electron spin in any coherent superposition of $|0\rangle$ and $|1\rangle$. A Rabi frequency protocol is shown in figure 2-7. The plot of NV^- fluorescence versus the microwave pulse duration shows an oscillation pattern. If the spin system is exposed to noise from the environment and experiences decoherence, the oscillation will decay exponentially

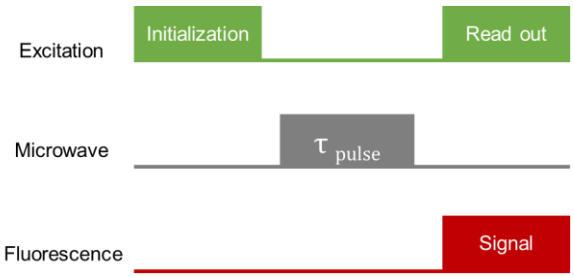

Figure 2-7 Rabi measurement protocol.

When a polarized NV center spin interacts with the environment, it experiences decoherence, meaning it goes back to its original state. The relaxation time of a polarized spin system is characterized by two categories: longitudinal electron spin relaxation time (T_1) and transverse-spin phase-coherence time (T_2).

T_1 can be affected by several factors such as temperature and NV center concentration [34][35]. T_1 is mainly affected due to the interaction of the spin system with the phonon from the lattice or other types of impurities. T_1 can be measured in milliseconds at room temperature and can take longer at low temperatures. To measure T_1, the NV center is polarized, then after time τ the NV center signal is read

as shown in figure 2-8 (a). By using this method, the population in the $m_s = 0$ level can be determined at different times after the polarization. Sometimes, the relaxation rate (1/ T) is reported.

Conversely, T_2 is measured by first polarizing the NV center. Second, a π/2 microwave pulse is applied, then after time τ has elapsed, a π refocusing wave is applied. Third, after time τ has elapsed, a π/2 microwave pulse is applied, and the NV center state is read out as shown in figure 2-8 (b). The purpose of refocusing is to cancel out the static magnetic field [36]. It is possible to extend T_2 by applying dynamical decoupling sequences to decouple the NV center spin state from the spin bath [37]. T_2 can also be improved by measuring the spin state at low temperatures or using a sample that has a low number of P1 centers [37].

T_1 is shorter for the NV center located near the diamond surface, but T_2 is the shortest. For the NV center that exists in the ultrapure diamond crystal, T_1 is mainly limited by phonons, and T_2 is mainly limited by the interaction with the ^{13}C isotope in the lattice [38].

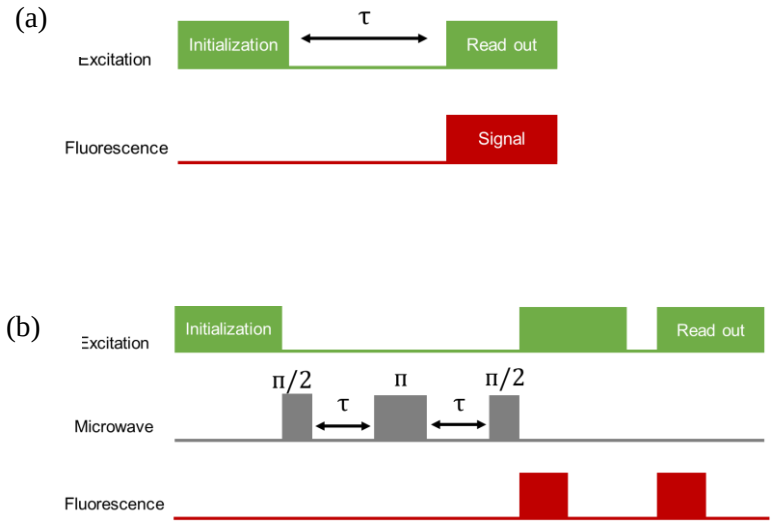

Figure 2-8 measurement protocol for (a) T_1 and (b) T_2.

2.6 Charge state control of the NV center

For most applications, the NV center needs to be in its negatively charged state because of its preferred spin-manipulation readout properties. Sometimes the charge of the NV center is unstable near the diamond surface, and charge conversion between NV^0 and NV^- is possible. The NV center should always be in its negatively charged state during any kind of application. There are two methods used to control the charge state of NV center: passive (chemical) and active (electrical or optical). The following section briefly discusses the charge state control methods.

2.6.1 Passive (chemical) method

A shallow NV center is vulnerable to charge state instability, meaning that the NV center can be easily ionized into the NV^0 state. This transition leads to the upward-band bending near the diamond surface due to impurities or other surface acceptors [39]. The charge state of the NV center depends on the Fermi level concerning the charge-transition level. This charge-transition level determines whether the NV center will lose or accept an electron. The $NV^{0/-}$ transition level corresponds to the transition from a positively charged state to a negatively charged state, meaning if the Fermi level is shifted above this transition level, the NV center will accept an electron and vice versa. The position of the $NV^{+/0}$ transition level is below the $NV^{+/0}$ transition level [40].

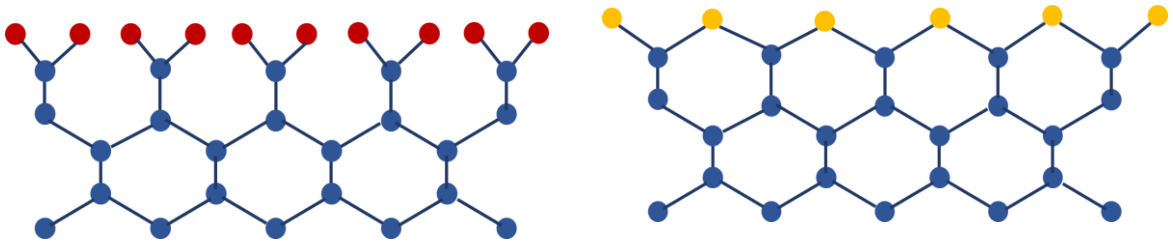

(a) (b)

Figure 2-9 (a) Hydrogen- and (b) oxygen-terminated diamond.

To suppress this upward-band bending near the surface, an accurate surface termination is required. There are two types of surface terminations, hydrogen and oxygen terminations. For the hydrogen termination (figure 2-9 (a)), the adsorbates provide energy levels that act as an acceptor state for electrons, and this shifts the Fermi energy level. This leads to the upward-band bending, and a two-dimensional gas is formed at the diamond surface. The band bending causes the accumulation of holes, and that makes the NV center to become positively charged [39][40]. Therefore, hydrogen termination is not suitable for NV^- charge stabilization. Conversely, oxygen terminations (figure 2-9 (b)) are preferable for NV^- stabilization because they suppress the upward bending. According to reference [41],

compared to the C-H bond from hydrogen termination, an oxygen-terminated surface with a C-O bond can efficiently pin the Fermi level near the midgap to suppress the upward-band bending and avoid surface potential fluctuations, thus making NV^- near the surface more stable.

2.6.2 Active method

Active control is the ability to freely control the charge state conversion of the NV center in real-time. Optical and electrical methods are normally used. Based on reference [42], the charge state of the NV center depends on the wavelength and power of the excitation laser. They also found that a shorter wavelength induces q single-photon process, compared to a two-photon process at a longer wavelength.

For the electrical control method, the principle used to control the charge state of the NV center is similar to passive control, which is the Fermi level modulation. To achieve electrical control, a device structure is needed. Several reports have used several types of device structures such as the Schottky, PIN, and NIN diodes [43][44][45]. By applying external biases to the diode, band bending in the diode depletion region can be modulated, and the Fermi level can be shifted. When the Fermi level crosses the NV center's charge-transition level, as mentioned in Section 2.5.1, the NV center can be converted into NV^- by applying a reverse bias and converted back into NV^0 by applying a forward bias.

2.7 NV center applications

The outstanding properties of the NV center, such as long coherence time even at room temperature, have motivated scientists and engineers to develop a technology based on the NV center, which can perform at higher speeds and with sensitive sensors. As mentioned in Section 2.2, NV^- can be easily manipulated and readout through an optical method. By developing and designing an optical and MW excitation protocol, it is possible to use the NV center to store and process information or to use it as a sensitive sensor that can detect small changes in the environment.

Recently, quantum computing has become a hot topic. By exploiting quantum mechanics, it is now possible to develop a quantum processor that utilizes superposition and entanglement to enhance particular algorithms such as factorization, optimization, and simulation [46][47][48]. [48]. A quantum computer has more computing power and speed than traditional computers. "Classical computing" uses bits, which use binary digits denoted as "0" and "1" [49]. Similar to classical bits, quantum bits or "qubits" also have "1" and "0" states, but these states can be in superposition, and this is the reason a quantum computer can make fast calculations [50] and the NV center uses these criteria. Because the NV center is a defect that resides in the diamond bandgap, which results in its wavefunction being localized and not interacting with the conduction and valence bands, protects it from external

disturbances that can cause decoherence. An NV center coherence time of more than 1 s has been reported [51] [52]. A longer coherence time is required for the quantum system to retain its information long enough to be able to perform a calculation. As mentioned before, the NV center can have a longer spin coherence even at room temperature because of its high Debye temperatures and low spin-orbit coupling, which results in long-spin lifetimes [53] [54]. When the system can be operated at room temperature, there is no need to cool the system with a complex and expensive cooling system at any point. Because the NV center exists in a diamond solid-state host, is it possible to fabricate wiring and waveguides for each qubit [55][56]. The photonic structure on the diamond sample can also be designed to couple with the NV center [57] [58].

A secure communication can make use of the quantum mechanics phenomena. Currently, sensitive data are encrypted and then delivered through fiber-optic cables, and a "key" is used to decipher the information. These data and keys are based on classical bits, and they are vulnerable to hacking. Quantum communication can protect these sensitive communications. A quantum network can be constructed by utilizing "entanglement" to connect local processing nodes, which contain long-lived qubits of which the NV center can be a prime candidate [59]. In 2013, a study succeeded in establishing entanglements between two NV^- spins separated by 3 m [60].

The NV center is sensitive to its surroundings and can detect significantly small changes. This is another reason the NV center can be used as a sensor, such as a magnetometer, used to sense magnetic fields. Through the Zeeman interaction and ODMR measuring system, a sensitive magnetometer can be realized [61][25][62]. A single NV center can be combined with the atomic force microscope (AFM) onto the tip. By combining this tip with the laser and MW excitation, the system can become an atomic size, non-destructive, scanning probe under ambient conditions [25]. When the AFM tip is in close contact with the target sample, the NV center will detect a magnetic signal radiated from the sample and cause changes in the resonance spectrum. Based on the resonance spectrum, it is possible to determine the quantitative value of the magnetic field produced from the target sample. Other than the magnetic field, certain studies have reported that the NV center can be used to measure the electric field and temperature [63][64].

2.8 References:

[1] R. S. Balmer *et al.*, "Chemical vapour deposition synthetic diamond: Materials, technology and applications," *J. Phys. Condens. Matter*, vol. 21, no. 36, 2009.

[2] S. Mandal, "Nucleation of diamond films on heterogeneous substrates: a review," *RSC Adv.*, vol. 11, no. 17, pp. 10159–10182, 2021.

[3] V. N. Mochalin, O. Shenderova, D. Ho, and Y. Gogotsi, "The properties and applications of nanodiamonds," *Nat. Nanotechnol.*, vol. 7, no. 1, pp. 11–23, 2012.

[4] J. E. Field, "The mechanical and strength properties of diamond," *Reports Prog. Phys.*, vol. 75, no. 12, 2012.

[5] H. A. Atikian *et al.*, "Diamond mirrors for high-power continuous-wave lasers," *Nat. Commun.*, vol. 13, no. 1, p. 2610, 2022.

[6] P. Koidl and C. P. Klages, "Optical applications of polycrystalline diamond," *Diam. Relat. Mater.*, vol. 1, no. 10–11, pp. 1065–1074, 1992.

[7] Z. Liu *et al.*, "Fabrication of UV Photodetector on TiO 2 /Diamond Film," *Sci. Rep.*, vol. 5, pp. 1–7, 2015.

[8] D. Araujo, M. Suzuki, F. Lloret, G. Alba, and P. Villar, "Diamond for electronics: Materials, processing and devices," *Materials (Basel).*, vol. 14, no. 22, 2021.

[9] F. V. Kaminsky and G. K. Khachatryan, "Characteristics of nitrogen and other impurities in diamond, as revealed by infrared absorption data," *Can. Mineral.*, vol. 39, no. 6, pp. 1733–1745, 2001.

[10] N. Donato, N. Rouger, J. Pernot, G. Longobardi, and F. Udrea, "Diamond power devices: State of the art, modelling, figures of merit and future perspective," *J. Phys. D. Appl. Phys.*, vol. 53, no. 9, 2020.

[11] F. P. Bundy, H. T. Hall, H. M. Strong, and R. H. Wentorf, "Man-Made diamonds," *Nature*, vol. 176, no. 4471, pp. 51–55, 1955.

[12] M. N. R. Ashfold, J. P. Goss, B. L. Green, P. W. May, M. E. Newton, and C. V. Peaker, "Nitrogen in Diamond," *Chem. Rev.*, vol. 120, no. 12, pp. 5745–5794, 2020.

[13] V. Sonin *et al.*, "The composition of the fluid phase in inclusions in synthetic HPHT diamonds grown in system Fe–Ni–Ti–C," *Sci. Rep.*, vol. 12, no. 1, pp. 1–9, 2022.

[14] J. E. Butler, Y. A. Mankelevich, A. Cheesman, J. Ma, and M. N. R. Ashfold, "Understanding

the chemical vapor deposition of diamond: Recent progress," *J. Phys. Condens. Matter*, vol. 21, no. 36, 2009.

[15] A. Tallaire, J. Achard, F. Silva, O. Brinza, and A. Gicquel, "Growth of large size diamond single crystals by plasma assisted chemical vapour deposition: Recent achievements and remaining challenges," *Comptes Rendus Phys.*, vol. 14, no. 2–3, pp. 169–184, 2013.

[16] M. W. Doherty, N. B. Manson, P. Delaney, and L. C. L. Hollenberg, "The negatively charged nitrogen-vacancy centre in diamond: The electronic solution," *New J. Phys.*, vol. 13, 2011.

[17] V. M. Acosta, "Optcial Magnetometry with Nitrogen-Vacancy Centers in Diamond," University of California Berkeley, 2011.

[18] M. W. Doherty *et al.*, "Measuring the defect structure orientation of a single NV- centre in diamond," *New J. Phys.*, vol. 16, 2014.

[19] E. M. S. Stennett, M. A. Ciuba, and M. Levitus, "Photophysical processes in single molecule organic fluorescent probes," *Chem. Soc. Rev.*, vol. 43, no. 4, pp. 1057–1075, 2014.

[20] S. F. Lee and M. A. Osborne, "Brightening, blinking, bluing and bleaching in the life of a quantum dot: Friend or foe?," *ChemPhysChem*, vol. 10, no. 13, pp. 2174–2191, 2009.

[21] M. W. Doherty *et al.*, "Measuring the defect structure orientation of a single NV- centre in diamond," *New J. Phys.*, vol. 16, 2014.

[22] E. Abe and K. Sasaki, "Tutorial: Magnetic resonance with nitrogen-vacancy centers in diamond - Microwave engineering, materials science, and magnetometry," *J. Appl. Phys.*, vol. 123, no. 16, pp. 3–14, 2018.

[23] J. Wrachtrup and A. Finkler, "Single spin magnetic resonance," *J. Magn. Reson.*, vol. 269, pp. 225–236, 2016.

[24] R. Schirhagl, K. Chang, M. Loretz, and C. L. Degen, "Nitrogen-Vacancy Centers in Diamond: Nanoscale Sensors for Physics and Biology," *Annu. Rev. Phys. Chem.*, vol. 65, no. 1, pp. 83–105, 2014.

[25] L. Rondin, J. P. Tetienne, T. Hingant, J. F. Roch, P. Maletinsky, and V. Jacques, "Magnetometry with nitrogen-vacancy defects in diamond," *Reports Prog. Phys.*, vol. 77, no. 5, 2014.

[26] A. Schweiger and G. Jeschke, *Principles of Pulse Electron Paramagnetic Resonance*. Oxford University Press, 2005.

[27] E. O. Schafer-Nolte, "Development of a Diamond-based Scanning Probe Spin Sensor

Operating at Low Temperature in Ultra High Vacuum," Universitat Stuttgart, 2014.

[28] X.-F. He, N. B. Manson, and F. Peter T.H., "Paramagnetic resonance of photoexcited N-V defects in diamond. I. Level anticrossing in the 3A ground state," *Phys. Rev. B*, vol. 47, pp. 8809–8815, 1993.

[29] P. Tamarat *et al.*, "Stark shift control of single optical centers in diamond," *Phys. Rev. Lett.*, vol. 97, no. 8, pp. 1–4, 2006.

[30] E. Van Oort and M. Glasbeek, "Electric-field-induced modulation of spin echoes of N-V centers in diamond," *Chem. Phys. Lett.*, vol. 168, no. 6, pp. 529–532, 1990.

[31] F. Dolde *et al.*, "Electric-field sensing using single diamond spins," *Nat. Phys.*, vol. 7, no. 6, pp. 459–463, 2011.

[32] D. Zheng, "Study and manipulation of photoluminescent NV color center in diamond Study and Manipulation of Photoluminescent NV Color Center in Diamond Étude et Manipulation des Propriétés de Spin du Centre Coloré PhD of Physics of École Normal Supérieure de Cachan," Ecole Normal Superieure de Cachan, 2010.

[33] M. Lesik, D. E. L. E. Normale, S. D. E. Cachan, and M. Lesik, "Engineering of NV color centers in diamond for their applications in quantum information and magnetometry To cite this version : HAL Id : tel-01158995 Domaine : Engineering of NV color centers in diamond for their applications in quantum information and m," 2015.

[34] A. Jarmola, V. M. Acosta, K. Jensen, S. Chemerisov, and D. Budker, "Temperature- and magnetic-field-dependent longitudinal spin relaxation in nitrogen-vacancy ensembles in diamond," *Phys. Rev. Lett.*, vol. 108, no. 19, pp. 1–5, 2012.

[35] M. Mrózek, D. Rudnicki, P. Kehayias, A. Jarmola, D. Budker, and W. Gawlik, "Longitudinal spin relaxation in nitrogen-vacancy ensembles in diamond," *EPJ Quantum Technol.*, vol. 2, no. 1, 2015.

[36] N. E. K. Chisholm, "Single spin magnetometry with nitrogen vacancy centers in diamond," Harvard University, 2015.

[37] L. T. Hall, C. D. Hill, J. H. Cole, and L. C. L. Hollenberg, "Ultrasensitive diamond magnetometry using optimal dynamic decoupling," *Phys. Rev. B - Condens. Matter Mater. Phys.*, vol. 82, no. 4, pp. 1–5, 2010.

[38] C. Jeson, "Quantum Enginering in Diamond," Texas A&M University, 2015.

[39] M. V. Hauf *et al.*, "Chemical control of the charge state of nitrogen-vacancy centers in diamond," *Phys. Rev. B - Condens. Matter Mater. Phys.*, vol. 83, no. 8, pp. 1–4, 2011.

[40] B. Grotz *et al.*, “Charge state manipulation of qubits in diamond,” *Nat. Commun.*, vol. 3, 2012.

[41] H. Yamano *et al.*, “Charge state stabilization of shallow nitrogen vacancy centers in diamond by oxygen surface modification,” *Jpn. J. Appl. Phys.*, vol. 56, no. 4, 2017.

[42] X. D. Chen, C. L. Zou, F. W. Sun, and G. C. Guo, “Optical manipulation of the charge state of nitrogen-vacancy center in diamond,” *Appl. Phys. Lett.*, vol. 103, no. 1, 2013.

[43] C. Schreyvogel, V. Polyakov, R. Wunderlich, J. Meijer, and C. E. Nebel, “Active charge state control of single NV centres in diamond by in-plane Al-Schottky junctions,” *Sci. Rep.*, vol. 5, no. July, 2015.

[44] C. Schreyvogel, M. Wolfer, H. Kato, M. Schreck, and C. E. Nebel, “Tuned NV emission by in-plane Al-Schottky junctions on hydrogen terminated diamond,” *Sci. Rep.*, vol. 4, pp. 1–6, 2014.

[45] H. Kato *et al.*, “Tunable light emission from nitrogen-vacancy centers in single crystal diamond PIN diodes,” *Appl. Phys. Lett.*, vol. 102, no. 15, pp. 1–5, 2013.

[46] R. P. Feynman, “Simulating physics with computers,” *Int. J. Theor. Phys.*, vol. 21, no. 6–7, pp. 467–488, 1982.

[47] S. McArdle, S. Endo, A. Aspuru-Guzik, S. C. Benjamin, and X. Yuan, “Quantum computational chemistry,” *Rev. Mod. Phys.*, vol. 92, no. 1, p. 15003, 2020.

[48] P. W. Shor, “Polynomial-time algorithms for prime factorization and discrete logarithms on a quantum computer,” *SIAM J. Comput.*, vol. 26, no. 5, pp. 1484–1509, 1997.

[49] C. Wetterich, “Quantum computing with classical bits,” *Nucl. Phys. B*, vol. 948, p. 114776, 2019.

[50] N. P. de Leon *et al.*, “Materials challenges and opportunities for quantum computing hardware,” *Science (80-.).*, vol. 372, no. 6539, 2021.

[51] L. Gordon, J. R. Weber, J. B. Varley, A. Janotti, D. D. Awschalom, and C. G. Van De Walle, “Quantum computing with defects,” *MRS Bull.*, vol. 38, no. 10, pp. 802–808, 2013.

[52] N. Bar-Gill, L. M. Pham, A. Jarmola, D. Budker, and R. L. Walsworth, “Solid-state electronic spin coherence time approaching one second,” *Nat. Commun.*, vol. 4, 2013.

[53] M. W. Doherty, N. B. Manson, P. Delaney, F. Jelezko, J. Wrachtrup, and L. C. L. Hollenberg, “The nitrogen-vacancy colour centre in diamond,” *Phys. Rep.*, vol. 528, no. 1, pp. 1–45, 2013.

[54] S. Prawer and A. D. Greentree, “Diamond for quantum computing,” *Science (80-.).*, vol. 320, no. 5883, pp. 1601–1602, 2008.

[55] E. Bourgeois *et al.*, “Photoelectric detection of electron spin resonance of nitrogen-vacancy centres in diamond,” *Nat. Commun.*, vol. 6, pp. 1–8, 2015.

[56] M. Gulka *et al.*, “Pulsed Photoelectric Coherent Manipulation and Detection of N-V Center Spins in Diamond,” *Phys. Rev. Appl.*, vol. 7, no. 4, pp. 1–7, 2017.

[57] T. Jung *et al.*, “Spin measurements of NV centers coupled to a photonic crystal cavity,” *APL Photonics*, vol. 4, no. 12, 2019.

[58] J. P. Hadden *et al.*, “Integrated waveguides and deterministically positioned nitrogen vacancy centers in diamond created by femtosecond laser writing,” *Opt. Lett.*, vol. 43, no. 15, p. 3586, 2018.

[59] H. J. Kimble, “The quantum internet,” *Nature*, vol. 453, no. 7198, pp. 1023–1030, 2008.

[60] H. Bernien *et al.*, “Heralded entanglement between solid-state qubits separated by three metres,” *Nature*, vol. 497, no. 7447, pp. 86–90, 2013.

[61] D. Rohner *et al.*, “(111)-Oriented, Single Crystal Diamond Tips for Nanoscale Scanning Probe Imaging of Out-of-Plane Magnetic Fields,” *Appl. Phys. Lett.*, vol. 115, no. 19, 2019.

[62] P. Maletinsky *et al.*, “A robust scanning diamond sensor for nanoscale imaging with single nitrogen-vacancy centres,” *Nat. Nanotechnol.*, vol. 7, no. 5, pp. 320–324, 2012.

[63] K. Bian *et al.*, “Nanoscale electric-field imaging based on a quantum sensor and its charge-state control under ambient condition,” *Nat. Commun.*, vol. 12, no. 1, pp. 1–9, 2021.

[64] J. Wang *et al.*, “High-sensitivity temperature sensing using an implanted single nitrogen-vacancy center array in diamond,” *Phys. Rev. B - Condens. Matter Mater. Phys.*, vol. 91, no. 15, pp. 1–9, 2015.

Chapter 3

Vertical diamond Schottky diode fabrication and experimental setup

3.1 Introduction

This chapter is divided into two parts. The first part explains the general process of the vertical diamond Schottky diode (VDSD) fabrication and how the NV center is created near the diamond sample surface. The second part discusses the instrument that will be used to characterize the diode, particularly regarding the development of an in-house optically detected magnetic resonance (ODMR) system.

3.2 Vertical diamond Schottky diode fabrication

This study focuses on the electrical control of the NV center. To achieve this electrical control method, a suitable device is required, and the vertical diamond Schottky diode structure was chosen.

3.2.1 Diamond thin film growth

The first step is to fabricate a diamond sample that consists of an NV center near the diamond surface. Figure 3-1 show the diamond's epitaxial layer growth and nitrogen-ion implantation. The diode is based on a high-pressure high-temperature type II diamond substrate (001) with dimensions $3 \times 3 \times 0.7$ mm^3. This diamond substrate has p-type conductivity with an acceptor density of 10^{20} cm^{-3}. The resistivity of this diamond sample is below 0.1 Ω which is appropriate for a vertical structure. A lightly boron-doped layer with a thickness of 1 μ was deposited onto the IIa substrate through microwave plasma-enhanced chemical vapor deposition (MPCVD).

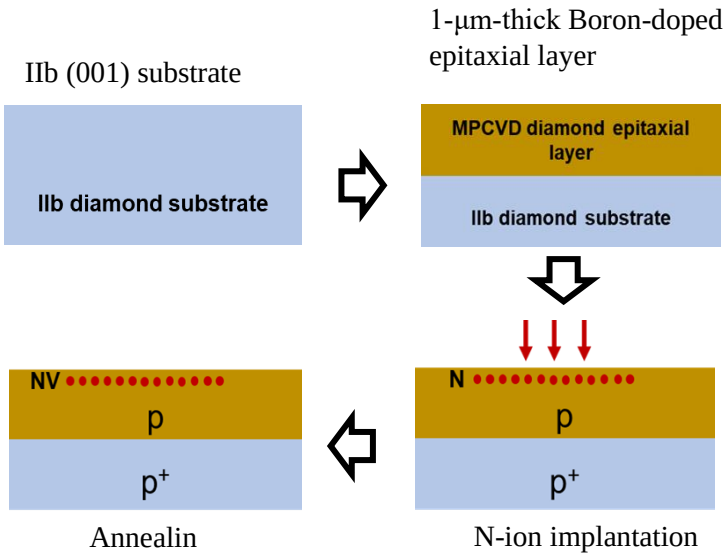

Figure 3-1. Diamond epitaxial layer and ion implantation.

3.2.2 Microwave Plasma Chemical Vapor deposition (MPCVD) process

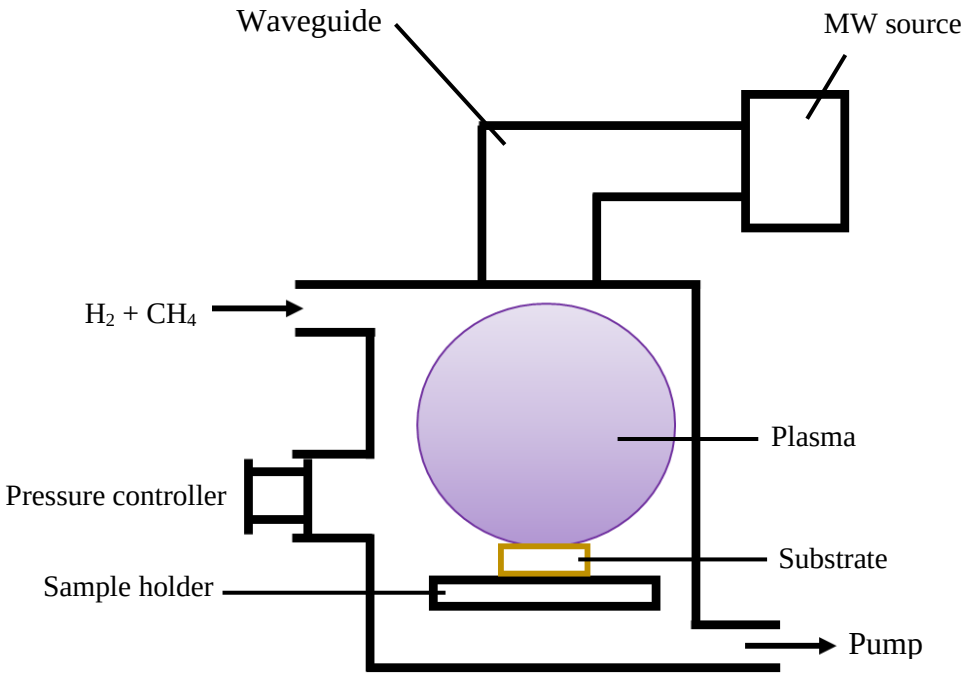

Figure 3-2 Schematic of the MPCVD system.

The CVD process uses a chemical reaction from a gas precursor to deposit desired material onto target substrates. In this thesis, only homoepitaxy growth was performed because the growth layer is the same material as the substrate material. Figure 3-2 shows a schematic of the MPCVD system used for epitaxial growth. A 2.45 GHz microwave radiation was delivered to the chamber using a waveguide.

Subsequently, the plasma was corrected such that it could be at the center of the chamber, in which the substrate was placed. The deposition was done by injecting a mixture of methane and hydrogen into the chamber [1][2]. Because the system uses MW for plasma generation, it can use various gas mixtures such as oxygen contents, chlorinate, fluorinated gases, unlike hot filament chemical vapor deposition, which may introduce impurities from the hot filament [3]. Table 3-1 lists the deposition conditions based on reference [4].

Table 3-1. Growth condition for diamond epitaxial layer

Gas sources	$B(CH_3)$, CH_4, H_2
$[CH_4]/[H_2]$	0.3 %
$[B(CH_3)_3]/[CH_4]$ ratio	5 ppm
Gas pressure	25 Torr
Microwave power	750 W
Substrate temperature	800°C

3.2.3 Nitrogen ion implantation

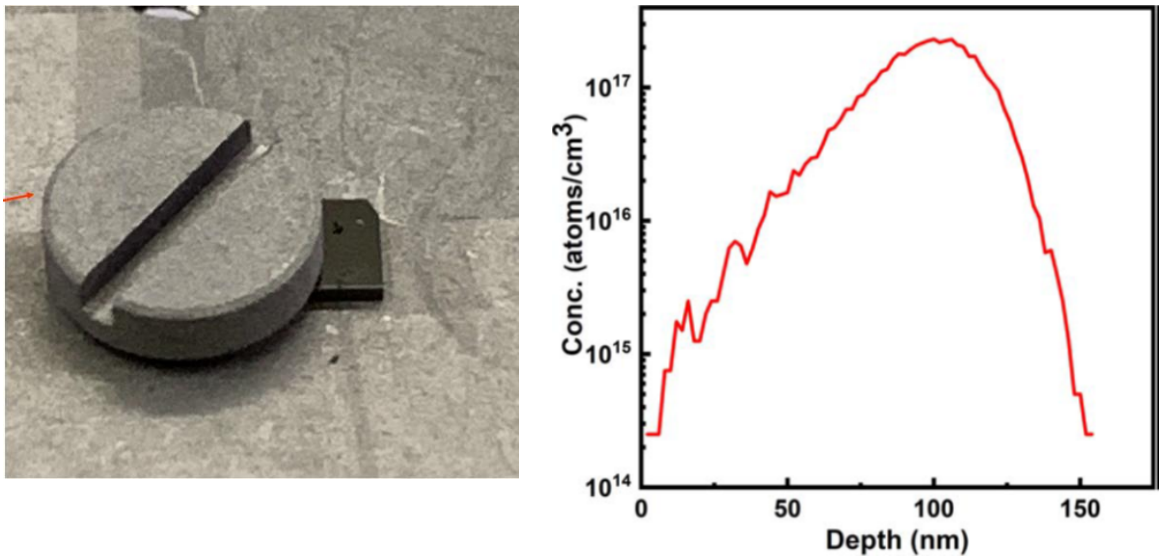

Figure 3-3 Stopping and Range of Ions in Matter (SRIM) simulation results.

Before fabricating the contact electrode, nitrogen-ion implantation was performed to create an NV center. Because this study focuses on the NV center near the diamond surfaces, it is crucial to use proper implantation dose and energy. An advantage of using this method is that the nitrogen can be implanted at a desirable location on the diamond surface, which is essential for integration with a photonic microchip or coupling to a nearby NV center [5][6][7]. To estimate the implantation depth of the nitrogen, an implantation simulation software was used known as the Stopping and Range of Ions in

Matter (SRIM). Figure 3-3 shows the SRIM result for the sample that was used in this experiment. The nitrogen dose and energy that was used for ion implantation were $10^{12}cm^{-2}$ and 80 keV, respectively. The implantation depth of this energy was 100 nm. The sample was then annealed at 1000 °C to create an NV center. Only half of the sample was irradiated for comparison purposes, as shown in figure 3-3.

3.2.4 Contact electrode fabrication

To complete the device fabrication process, it is necessary to fabricate ohmic and Schottky contact. Both contact electrodes are realized through the photolithography process. Figure 3-4 show electrode contact fabrication steps.

For the ohmic contact, a Ti(30 nm)/Pt(30 nm)/Au(100 nm) contact was fabricated on the entire backside of the diamond sample. To further enhance the ohmic characteristic, the sample was annealed at 420 °C for 30 min to form titanium carbide. Each of the different metal layers serves a specific function. The titanium (Ti) reacts with the diamond to form a titanium carbide, which results in a low contact resistance [8]. Platinum (Pt) works as a barrier to prevent Ti diffusion into the gold (Au) layer [9] and gold has good conductivity.

Before the fabrication of the Schottky contact, ultraviolet (UV) ozone treatment was performed on the diamond sample surface such that it could have an oxygen-terminated surface. As mentioned in Section 2.5.1, the charge state of the NV center near the surface can be controlled by the type of surface termination. Oxygen termination is preferable because it can convert the NV center into the NV^- state. The Schottky contact was realized from Molybdenum (Mo) with a diameter and thickness of 300 µm and 10 µm, respectively. The Mo contact was made thin to allow for optical measurements to be performed directly under the Mo electrode. Both the ohmic contact and the Schottky diode fabrication processes are shown in figure 3-4. The 10 nm Mo had more than 50% transmittance above 400 nm wavelengths [10]. The gold contact was used for wire bonding. Figures 3-5 shows the completed Schottky diode.

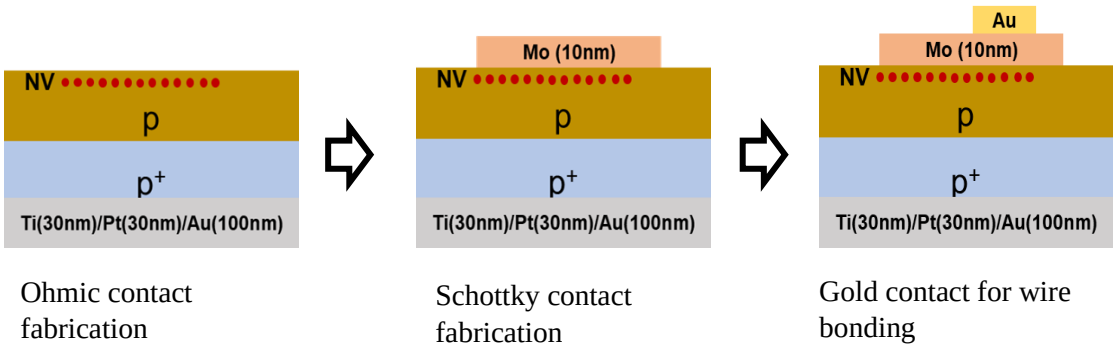

Figure 3-4 electrode fabrication steps.

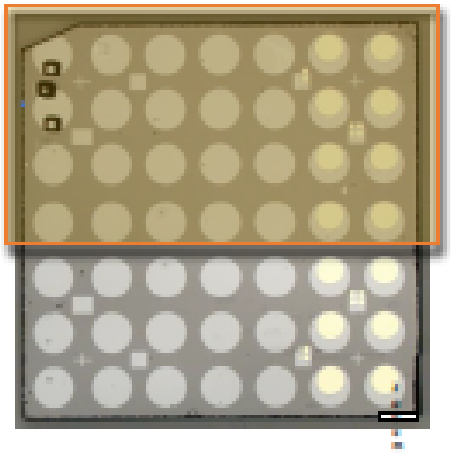

Figure 3-5 Image of a completed vertical diamond Schottky diode. The yellow box indicates the nitrogen-ion-implanted area.

3.3 Optically detected magnetic resonance setup

To study the NV center, a confocal setup was used because it provides advantages compared to a normal optical microscope. Confocal microscopes can address a single NV center and can obtain a very high signal-to-noise ratio (SNR). Before explaining in detail, the experimental setup used in this thesis, a brief introduction to confocal microscopy will be explained in the next subsection.

Optical microscopy was established in the 17th century and has mostly been used to study biological systems that are small and impossible to see with the naked eye. This microscope uses visible light and a combination of lenses to magnify the image of a small object. However, optical microscopy still has several weaknesses. Because the microscope uses visible light to view an object, the microscope cannot produce an image of the object if is smaller than the light wavelength. The diffraction barrier also hinders the microscope from resolving a very fine detail of the sample. Moreover, the microscope cannot be used to view thick samples, thus the sample is generally required to be a thin-cut section.

To overcome this problem, a new microscope, known as a confocal microscope, was developed and patented by Marvin Minsky in 1955 [11]. The confocal microscope has several advantages over the standard optical microscope, which is the abilities to collect a serial optical section of a thick sample, reduce or eliminate the background signal from the focal plane, and control the depth of the field. Figure 3-6 shows the important basic components of the confocal microscope: the objective lens, pinholes, laser excitation, and low-noise detector. Generally, a confocal microscope system works as follows: A coherent light, which is a laser beam, is used as the excitation source. The laser beam is then reflected by a dichromatic mirror. Subsequently, the reflected light ray is then focused on the sample by the objective lens. The focus light produces a small spot inside the sample. This spot has a small diameter

as the light wavelength is approximately 0.5 μm [11]. The same objective lens gathers the in-focus reflected light from the sample and focuses it on the detector.

For confocal microscopy, a coherence light source, typically a laser, is used as an excitation source. Certain lasers, such as argon and helium-neon ion laser that can provide continuous wave (CW) light at 488 and 514 nm, can be used for chromophores and fluorophores. Currently, solid-state diode lasers are becoming popular. They can emit a stable and more uniform laser light that produces less heat [12]. The type of objective lens used in the confocal setup is crucial because the lens will focus and collect the light emitted from the sample. The collection efficiency depends on the square of the numerical aperture (~N A^2). For a Gaussian beam, the minimum focal spot size d_0 is given by the following equation [13]:

$$d_0 = \frac{2\lambda}{\pi NA} \qquad 3\text{-}1$$

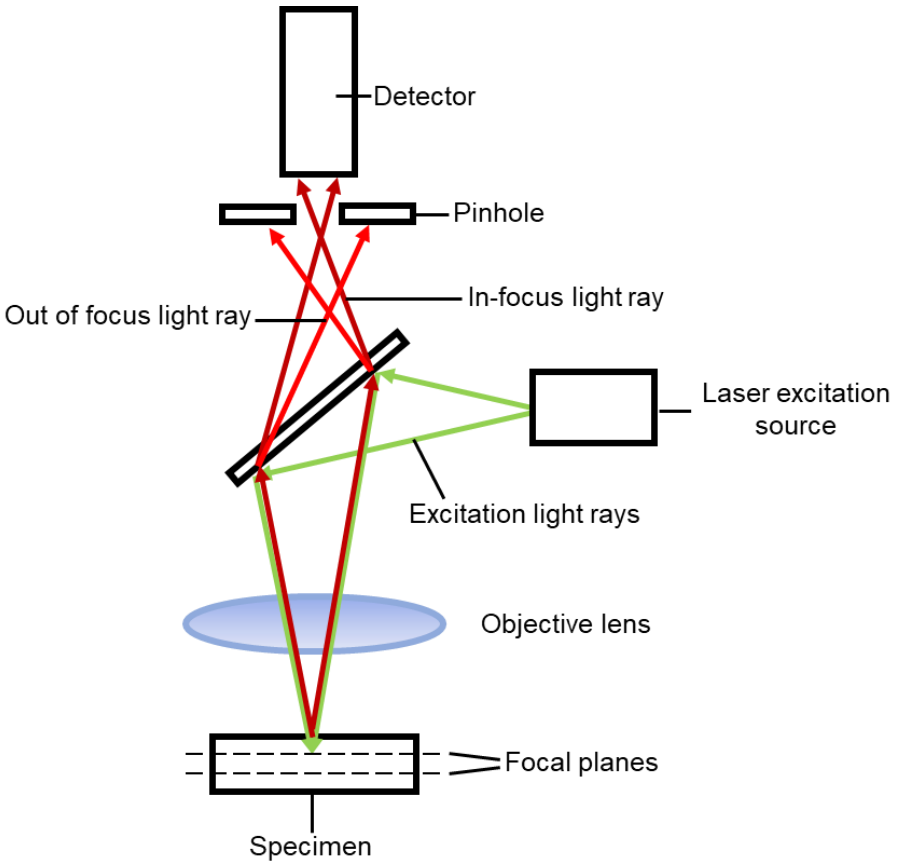

Figure 3-6 Simplified view of a confocal microscope.

where, λ is the light wavelength and NA is the numerical aperture of the lens. Equation 3-1, clearly states that the laser spot size is inversely proportional to the Na of the lens. The NA of the objective lens is defined as follows:

$$NA = n \sin \theta_D \quad 3\text{-}2$$

where, n denotes the medium refraction index and θ_D denotes the half angle of the maximum cone light that enters or exits the lens. For a lens that has NA > 0.95, it will be difficult to obtain a good image when air is used as the medium. This can be solved by using a higher refractive medium, such as oil, that is placed between the sample and the objective front lens. By using an oil-immersion lens, an NA of 1.40 can be achieved. The image resolution is determined by several parameters, for example, the objective lens numerical aperture, properties of the sample, and light wavelength

$$R_{lateral} = \frac{0.44\lambda}{NA} \quad 3\text{-}3$$

$$R_{axial} = \frac{1.5n\lambda}{NA^2} \quad 3\text{-}4$$

where R is the resolution.

3.4 Optically detected magnetic resonance (ODMR) modes

ODMR is a method used to manipulate the NV center spin by applying a laser illumination and microwave field to the NV center. Both combinations induce the NV center to make a transition between the energy levels. There are two types of ODMR measurements, CW and pulsed, and each has its advantages and disadvantages. CW ODMR is the easiest and mostly commonly used technique for spin manipulation. In this method, a continuous laser-, microwave driving-, and signal readouts are performed simultaneously, as shown in figure 3-7 [14]. However, the disadvantage of this method is that it suffers from inhomogeneous power broadening because of the combined high power of the laser and microwave and the effect is represented in figure 6 (a) reference [14].

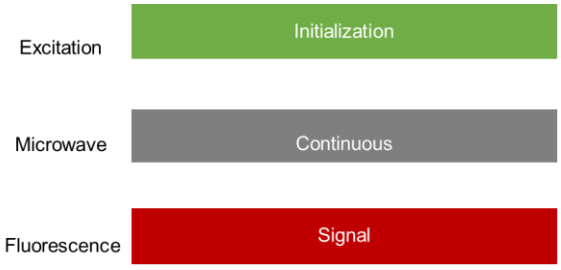

Figure 3-7 CW ODMR protocol shows the laser and microwave are applied simultaneously.

3.5 Development of experimental ODMR setup.

The ODMR setup designed and used for this experimental study is divided into two parts, hardware and the software. To detect and observe the spin state of the NV center, ODMR instruments were designed and developed. ODMR setups used in research laboratories are generally designed in-house because of the ability to add new functions to the setup. ODMR is based on confocal microscopy and offers several advantages for improving image resolution.

In this study, the system uses a 532 nm laser beam generated by a pumped solid-state laser (Nd:YVO4 diode, JUNO, by Kyocera). The laser beam passes through an objective lens and focuses on the sample. When the laser beam hits the sample, it produces a high intensity of fluorescence at a well-defined focal point. The signal from the sample enters the same objective lens, then the sample signal passes the dichroic mirror. The function of this mirror is to reflect a shorter wavelength but allow a longer wavelength to pass through. Subsequently, the signal is focused through a pinhole aperture, which removes much of the stray signal outside of the focal point [15] [11]. This is also the reason the confocal system can focus and detect in three dimensions. Finally, the signal is detected by the ANDOR charged-coupled device (CCD) camera. This optical part has two functions. First, it can be used to perform photoluminescence (PL) characterization of the NV center. Second, it detects photons for ODMR measurements.

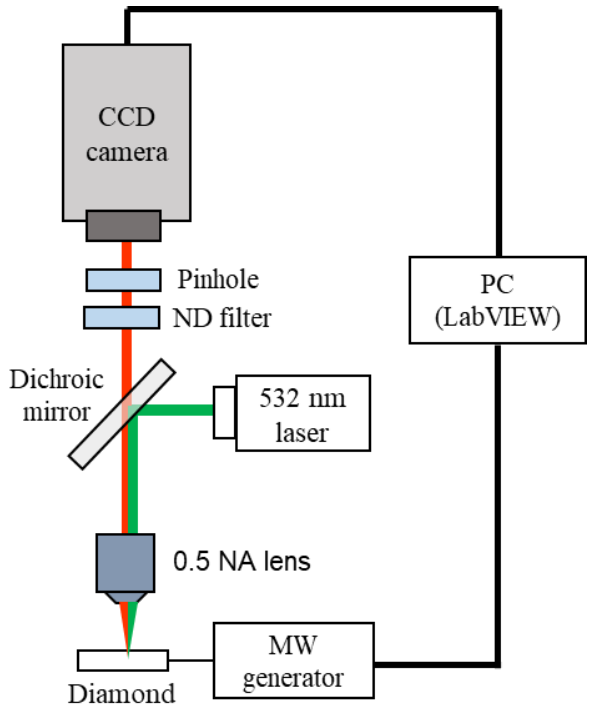

Figure 3-9 Schematic of the ODMR setup. A 532 nm laser is used as the excitation source, which is focused on the sample through a 0.5 NA objective lens. The fluorescence signal from the sample passes the same objective lens to the CCD camera.

(a) (b)

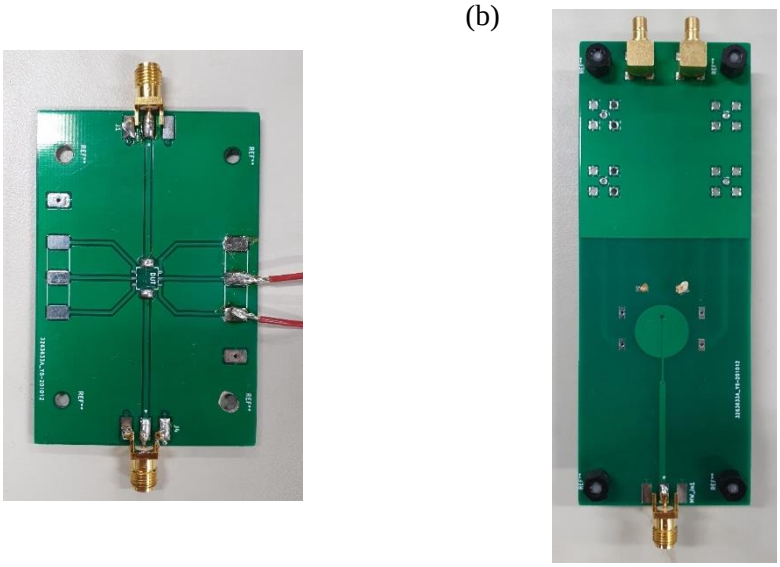

Figure 3-10 Two types of antennas: (a) thin copper wire and (b) microwave planar ring.

For NV center spin manipulation, the microwave (MW) was generated by using an R&S SMB100A, producing 25 dBm power at maximum. The MW signal was delivered to the sample using thin copper wire that was placed on top of the Schottky diode. External bias was applied to the Schottky

diode, by using a power supply (Keithley series 2280). Figure 3-9 shows an ODMR measurement setup used in this research. To deliver the microwave field to the NV center, two types of antennas were designed and fabricated on a printed circuit board (PCB). The first type is a simple thin copper wire, and the second is a microwave planar-ring antenna developed from reference [16] which is shown in figure 3-10.

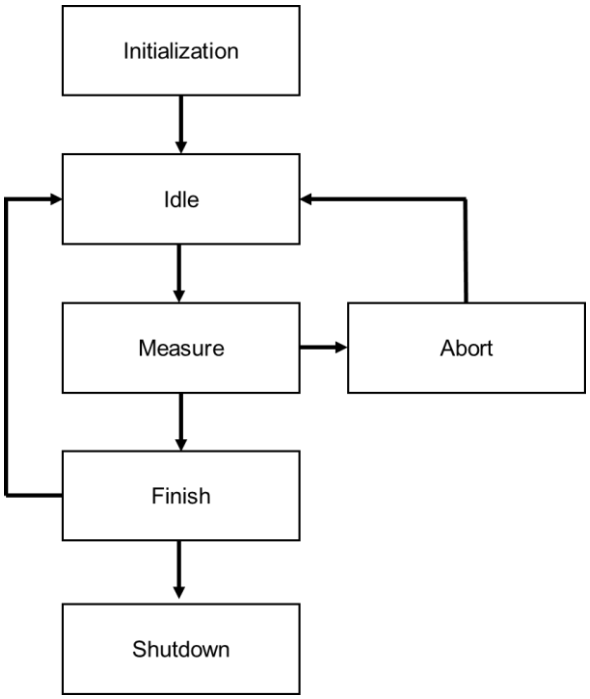

Figure 3-11 A LabVIEW program workflow.

To control all the hardware such as microwave generators and CCD cameras for spin manipulation, suitable software is required. For this purpose, LabVIEW, a graphical programming environment used to develop automated test systems for research, validation, and manufacturing, was developed. The workflow of the LabVIEW program is shown in figure 3-11. Because our setup does not require a pulse function, the software is relatively straightforward.

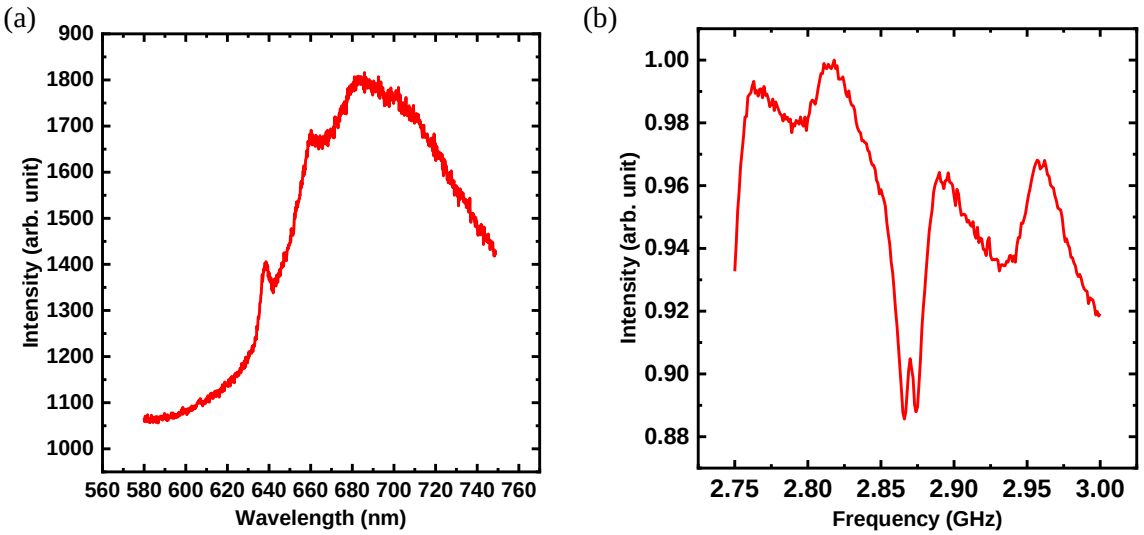

Figure 3-12 (a) NV center PL from the 1B diamond substrate. (b) NV center ODMR spectrum before the normalization protocol.

To test the ODMR instrument, a 1B diamond substrate was used as a reference sample. The diamond sample was placed on the wire-type antenna PCB. First, the photoluminescence spectrum was taken, to identify the NV center location; the spectrum is shown in figure 3-12 (a). After the confirmation of the NV center location, a microwave sweep was applied. As shown in figure 3-12 (b), an ODMR spectrum is observed, in which the ODMR dip is at 2.87 GHz, but the spectrum does not look like a typical NV center ODMR. To overcome this problem the spectrum taken during the microwave ON state is normalized to the microwave OFF state shown in figure 3-13. This protocol is repeated for each point of the measured frequency. The purpose is to eliminate contributions from slow variations during each microwave frequency [17].

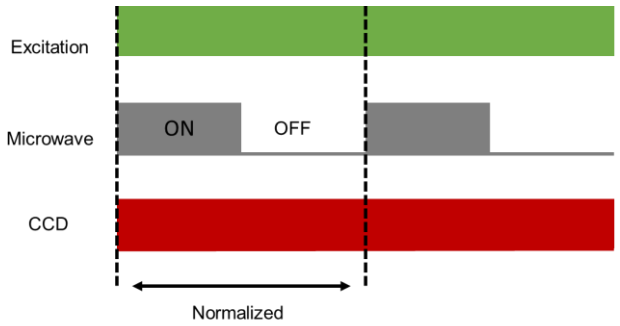

Figure 3-13 Normalization protocol to get a smooth NV center ODMR spectrum.

The experiment was repeated after applying the normalization protocol, where the ODMR spectrum showed an improved spectrum shape (figure 3-13). The NV center resonance peak center is

at 2.87 GHz accompanied by a small side resonance coming from ^{13}C. the ODMR also shows a split caused by crystal strain [18]. By applying increasing microwave power, the ODMR contrast is increased. After applying a magnetic field to the sample, the degeneracy of $m_s = \pm 1$ was lifted thus ODMR splitting was observed (figure 3-14). Two types of antennas mentioned before were also tested, and both functioned perfectly based on the observation of the NV center resonance spectrum shown in figure 3-15.

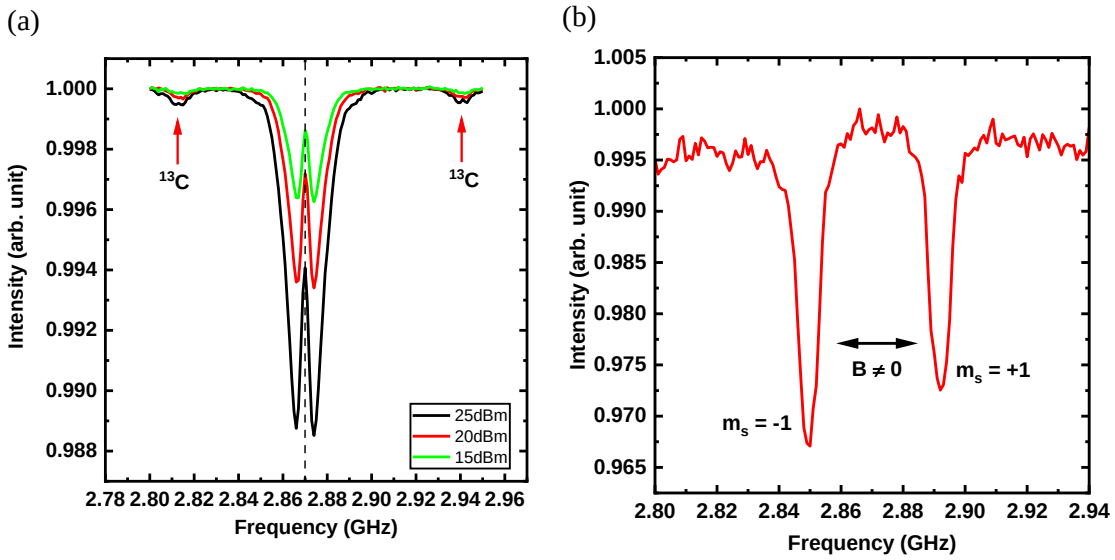

Figure 3-14 (a) Normalization protocol was applied to get a smooth NV center OMDR spectrum. (b) ODMR splitting was observed under an applied magnetic field.

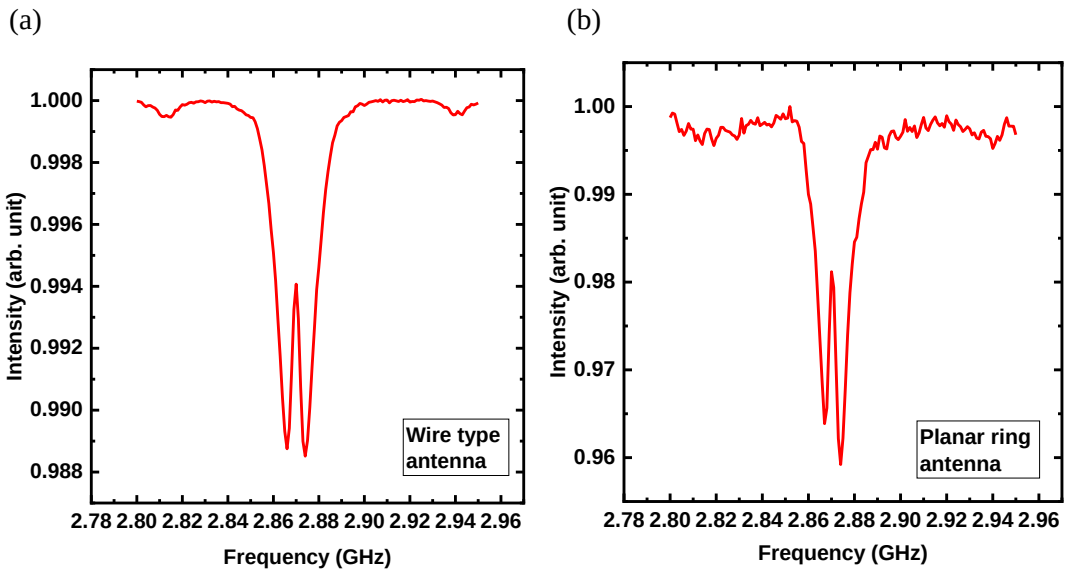

Figure 3-15 ODMR spectrum for both (a) wire-type and (b) planar-ring antennas.

3.6 Summary

This chapter describes the VDSD fabrication process and the development of a confocal ODMR setup. The nitrogen-ion implantation process was used to successfully create NV centers in the VDSDs by observing the PL spectrum characteristic. In this case, two charge states were observed, neutral (NV^0) and negatively charged (NV^-), for the same measurement spot. The NV center can be created during substrate growth or a device fabrication process. The NV center can also be created by implementing the nitrogen-ion implantation method, and it is the current method for introducing implantation atoms into diamond post-growth. Using this method, it is possible to control the NV center concentration and depth inside the bulk by adjusting the ion fluence and implantation kinetic energy [19]. Other than that, using a mask pattern such as a PMMA layer, a precise location can be chosen on the device's surface. The NV center created by ion implantation can be coupled to any photonic structure for a large-scale quantum information processing (QIP).

To study the properties of the NV center, a ODMR was designed and developed in-house. Although the setup developed in this research is relatively simple, the desired ODMR results were obtained, proving that the system works properly. Most laboratories that conduct research on NV centers use ODMR setups that were developed in-house. An in-house setup is preferable because it can be modified based on the type of measurements that will be performed. It is possible to develop the system from the ground up, from the simple ODMR CW mode to a sophisticated pulsed-sequence system such as the Rabi frequency. LabVIEW can give an intuitive user control experience for controlling the hardware. Its graphical programming environment allows users without advanced programming skills (such as python) to understand the programming flow and be able to develop the ODMR software using ‘click’ and ‘drop’.

3.7 References

[1] M. Kamo, Y. Sato, S. Matsumoto, and N. Setaka, "Diamond synthesis from gas phase in microwave plasma," *J. Cryst. Growth*, vol. 62, no. 3, pp. 642–644, 1983.

[2] I. Tanaka, H. Okubo, and Y. Harada, "Diamond synthesis on Si by plasma chemical vapor deposition using microwave sheath-voltage combination plasma," *Surf. Coatings Technol.*, vol. 423, no. May, p. 127592, 2021.

[3] P. W. May, "Diamond thin films: A 21st-century material," *Philos. Trans. R. Soc. A Math. Phys. Eng. Sci.*, vol. 358, no. 1766, pp. 473–495, 2000.

[4] J. Guo *et al.*, "Study of defects in diamond Schottky barrier diode by photocurrent spectroscopy," *Jpn. J. Appl. Phys.*, vol. 59, no. SG, 2020.

[5] S. L. Mouradian *et al.*, "Scalable integration of long-lived quantum memories into a photonic circuit," *Phys. Rev. X*, vol. 5, no. 3, 2015.

[6] T. Schröder *et al.*, "Quantum nanophotonics in diamond [Invited]," *J. Opt. Soc. Am. B*, vol. 33, no. 4, p. B65, 2016.

[7] T. Gaebel *et al.*, "Room-temperature coherent coupling of single spins in diamond," *Nat. Phys.*, vol. 2, no. 6, pp. 408–413, 2006.

[8] Y. Chen, M. Ogura, S. Yamasaki, and H. Okushi, "Ohmic contacts on p-type homoepitaxial diamond and their thermal stability," *Semicond. Sci. Technol.*, vol. 20, no. 8, pp. 860–863, 2005.

[9] H. A. Hoff *et al.*, "Ohmic contacts to semiconducting diamond using a Ti/Pt/Au trilayer metallization scheme," *Diam. Relat. Mater.*, vol. 5, no. 12, pp. 1450–1456, 1996.

[10] S. Kang, R. Nandi, J. K. Sim, J. Y. Jo, U. Chatterjee, and C. R. Lee, "Characteristics of an oxide/metal/oxide transparent conducting electrode fabricated with an intermediate Cu-Mo metal composite layer for application in efficient CIGS solar cell," *RSC Adv.*, vol. 7, no. 76, pp. 48113–48119, 2017.

[11] A. Nwaneshiudu, C. Kuschal, F. H. Sakamoto, R. Rox Anderson, K. Schwarzenberger, and R. C. Young, "Introduction to confocal microscopy," *J. Invest. Dermatol.*, vol. 132, no. 12, pp. 1–5, 2012.

[12] A. D. Elliott, "Confocal Microscopy: Principles and Modern Practices," *Curr. Protoc. Cytom.*, vol. 92, no. 1, pp. 1–18, 2020.

[13] L. Kuret, "Photo-induced ionization of the nitrogen-vacancy center," McGill University, 2015.

[14] E. V. Levine *et al.*, "Principles and techniques of the quantum diamond microscope," *Nanophotonics*, vol. 8, no. 11, pp. 1945–1973, 2019.

[15] J. A. Drazba, "Introduction to confocal microscopy," *Microsc. Microanal.*, vol. 12, no. SUPPL. 2, pp. 1756–1757, 2006.

[16] K. Sasaki *et al.*, “Broadband, large-area microwave antenna for optically detected magnetic resonance of nitrogen-vacancy centers in diamond,” *Rev. Sci. Instrum.*, vol. 87, no. 5, 2016.

[17] H. L. Stern *et al.*, “Room-temperature optically detected magnetic resonance of single defects in hexagonal boron nitride,” *Nat. Commun.*, vol. 13, no. 1, pp. 1–9, 2022.

[18] M. Mrózek, J. Mlynarczyk, D. S. Rudnicki, and W. Gawlik, “Circularly polarized microwaves for magnetic resonance study in the GHz range: Application to nitrogen-vacancy in diamonds,” *Appl. Phys. Lett.*, vol. 107, no. 1, 2015.

[19] S. Sangtawesin, T. O. Brundage, Z. J. Atkins, and J. R. Petta, “Highly tunable formation of nitrogen-vacancy centers via ion implantation,” *Appl. Phys. Lett.*, vol. 105, no. 6, 2014.

Chapter 4

Investigation of the nitrogen-vacancy center inside a Schottky diode using optically detected magnetic resonance

4.1 Introduction

In this chapter, the results of the experiment are presented, which are basic electrical characterization, photoluminescence (PL) spectrocopy, and optically detected magnetic resonance (ODMR). Measurements were performed to characterize the basic properties of VDSDs, and the results were used as reference data for subsequent experiments.

4.1.1 Electrical characterization

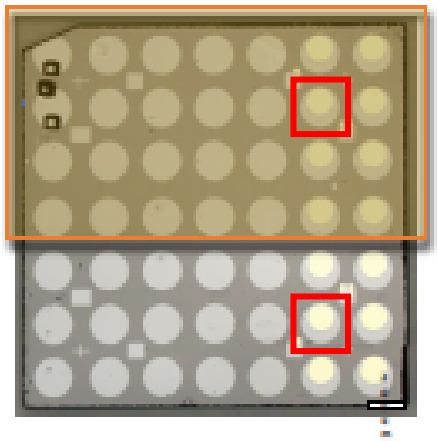

Figure 4-1. Top view of the VDSD The bigger yellow box indicates the area containing implanted ions. The small red box indicates the location for electrical characterization.

The details explanation of the current-voltage (I-V) and capacitance-voltage (C-V) measurements of the VDSD used in this study that were reported in reference [1]. Two measurements were taken at the implanted and non-implanted areas as shown in figure 4-1. The I-V measurements are shown in figure 4-2 (a). Rectification behavior was achieved for both areas, but there was a difference between forward and leakage currents. The ion implantation has introduced a higher defect density, which caused the forward current in the implanted area to become lower than that in the non-implanted

area. This was due to the change in series resistance and effective carrier concentration. The electrical properties of the VDSD have been degraded after ion implantation, and this can be related to the damage caused during the implantation process. Although ion implantation is good in creating NV centers, it does come with disadvantages. Implantation damages the diamond crystal lattice, and this side effect is inevitable.

The ideality factor can be calculated from the logarithmic plot slope from figure 4-2 (b) and the following equation.

$$n = \frac{q}{kT}\frac{dV}{dlnI} \tag{4.1}$$

The diode ideality factor is a measurement of how closely the diode follows the ideal diode equation. The ideality factor of an ideal diode is equal to 1. However, the ideality factor will always larger than one because of certain diode conditions, such as a series resistance. The zero-bias barrier height is determined by using the following equation:

$$\phi_B = \frac{kT}{q}(lnAA^* - lnI_0) \tag{4.2}$$

Figure 4-2 (b) shows the C-V and $1/C^2$-V measurements for both implanted and non-implanted areas. The capacitance difference between these two areas is related to changes in the thickness of the depletion layer because of the nitrogen-ion introduction into the boron-doped diamond film [2]). The difference in the capacitance between these two areas can be related to changes in the depletion layer thickness because of the nitrogen ion introduction into the boron-doped diamond film [3]. Other parameters of the VDSDs were also determined, and the values are presented in Table 4-1.

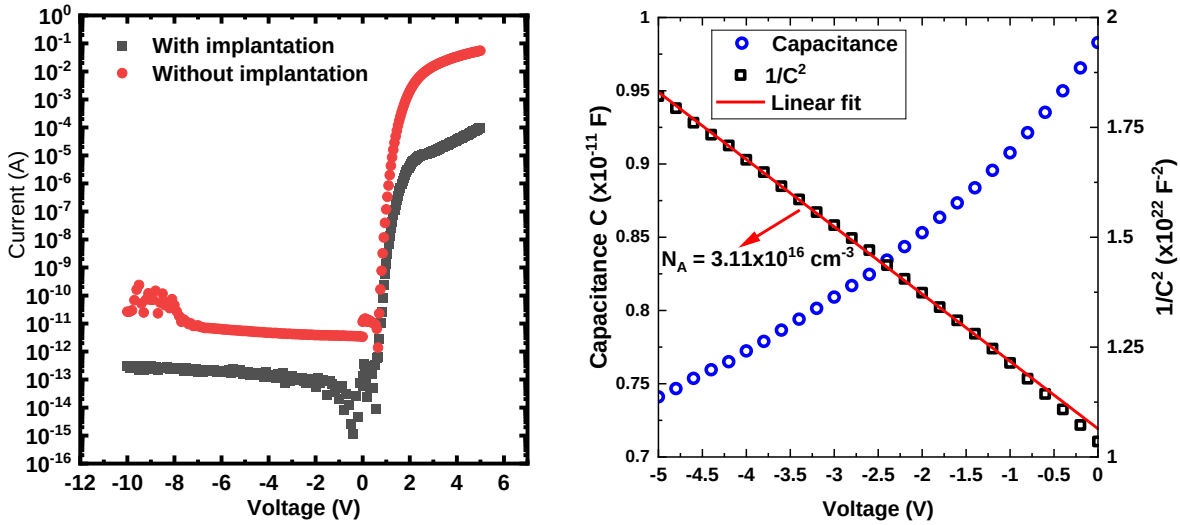

Figure 4-2 (a) IV characteristic of the VDSDs for the implanted and non-implanted area (b) C-V characteristic of the implanted area.

Table 4-1. VDSDs electrical characteristic for implanted and non-implanted area [1]

	Leakage current (A)	Series resistance (Ω)	Ideality factor	Depletion layer width at 0V (nm)	Barrier height (eV)
Non-implantation area	4.9×10^{-14}	29.2	1.3	120.4	1.3
implantation area	2.4×10^{-13}	1015.3	1.7	362.8	1.4

4.1.2 Optical characterization

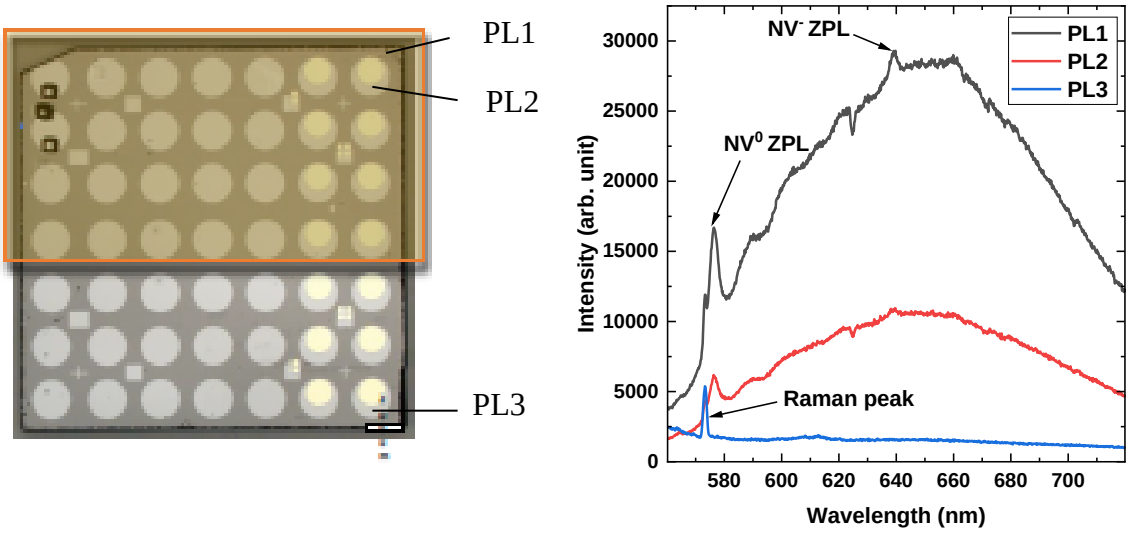

Figure 4-3 (a) Three different PL measurement points: PL1, PL2, and PL3. (b) Measured PL spectra for PL1 and PL2, which show the NV center characteristic curve, while for PL3, only the Raman peak was observed.

PL spectroscopy was performed to identify the NV centers created inside the VDSDs. Three different positions were chosen to be able to compare the implanted and non-implanted areas. These three positions are labeled as PL1 and PL2 for the implanted area PL3 for the non-implanted area, as shown in figure 4-3 (a). The NV center PL spectrum characteristics are shown for both PL1 and PL2 areas in figure 4-3 (b). Three sharp peaks are present for both spectra 572 nm, 575 nm, and 637 nm, which are first-order Raman peaks, NV^0 and NV^- ZPLs [4] [5][6]. The appearances of the NV center PL spectra show that the ion implantation and subsequent annealing have successfully created the NV center. The PL spectrum intensity of PL2 was reduced by the thin Mo electrode that reflected or scattered the photon signal of the NV center, which was located directly below the electrode. However, this thin Mo

electrode did not affect the NV center's PL spectrum characteristic. As expected, the PL spectrum of the NV center was not observed for non-implanted areas, due to the absence of the NV center. Only a first-order Raman peak at 572 nm was observed. The PL signal appeared after ion implantation and annealing because at high annealing temperatures, the vacancy becomes mobile in the diamond crystal lattice and combines with a nitrogen atom to form the NV center [7].

Both ZPL peaks appear in the same spectrum, meaning NV^0 and NV^- coexist. This NV center was mainly created mainly from the implantation process because the PL spectrum of the NV center was not observed from the non-implanted area. There could be several reasons for the coexistence of the NV center charge states. First, based on the SRIM simulation, the average depth of the implanted nitrogen is 100 nm, and it is close to the diamond surface. Ion implantations introduce graphitic defects, which can act as an acceptor layer, thus trapping the free electron and being unable to be captured by NV^0. According to a previous study, NV centers created near the surface (within 200 nm) of a highly pure diamond are found to be in a neutral state [8]. Second, a 532 nm laser beam used for excitation can convert part of the NV^0 into NV^-. Laser irradiation ionizes the substitutional nitrogen atoms, and the released electron is captured by a nearby NV center, then it is converted into NV^- [9][10][11]. Other than contributions from the donor, during laser irradiation, the NV center alternates between the neutral and negatively charged states [12]. This can be the reason the NV^- PL spectrum characteristic appears. Third, the boron-doped diamond, which can also act as an acceptor causes the NV center to be in a neutral state [13]. For this VDSDs, the NV centers created by ion implantation exist in two charge states. However, for application, only NV^- is required, thus the NV center should be negatively charged.

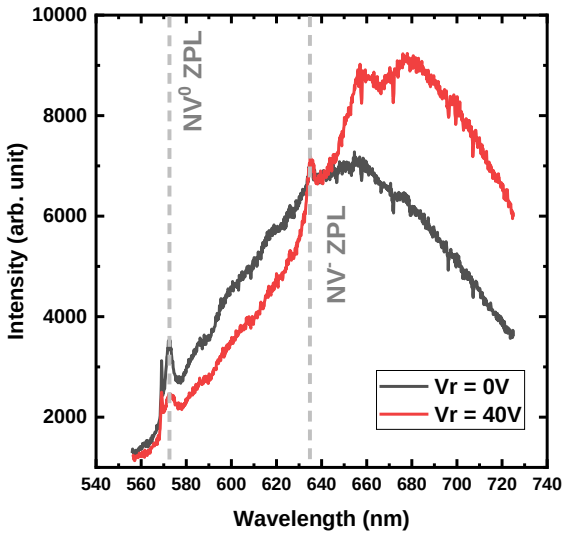

Figure 4-4 At a higher bias, the NV^- ZPL intensity is almost maintained, where all the emission come from the PBS.

At high Vr, the NV^- ZPL intensity is maintained, but the PBS is increased indicating that most of the converted NV^- emission goes to PBS emission (figure 4-4). ZPL is described as a direct emission from the excited state down to the ground state. Ninety-seven percent of the light is emitted from a broad emission that is associated with the photon and phonon. The ZPL is a good emission part, because this is the part where the light has not interacted with the crystal.

4.1.3 ODMR using wire-type and planar-ring antennas

In this thesis, two types of antennas were designed and fabricated: thin copper wire and planar ring-type, as mentioned in chapter 3.

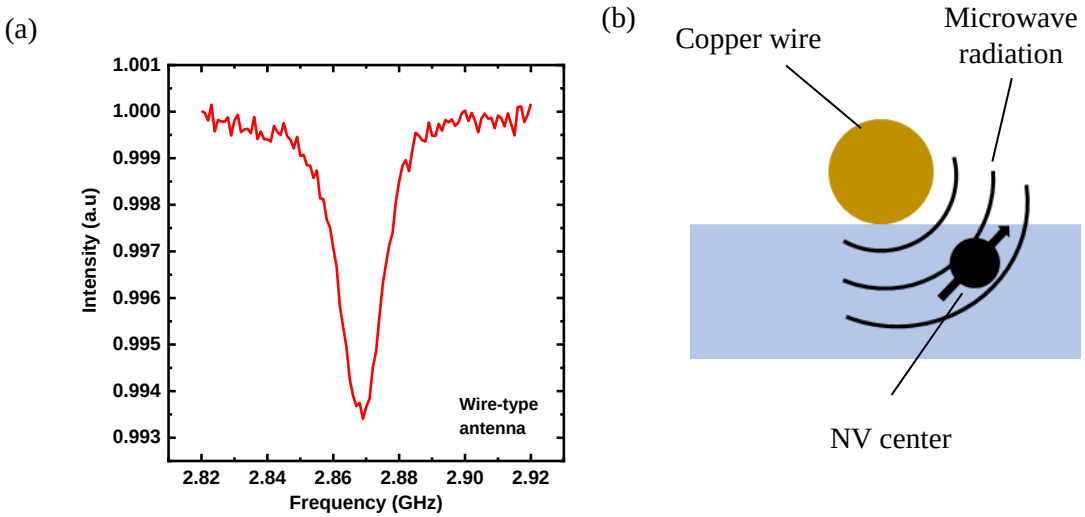

Figure 4-5 (a) ODMR spectrum of the Schottky diode using a wire-type antenna, and (b) the antenna placed close to the NV center for efficient manipulation.

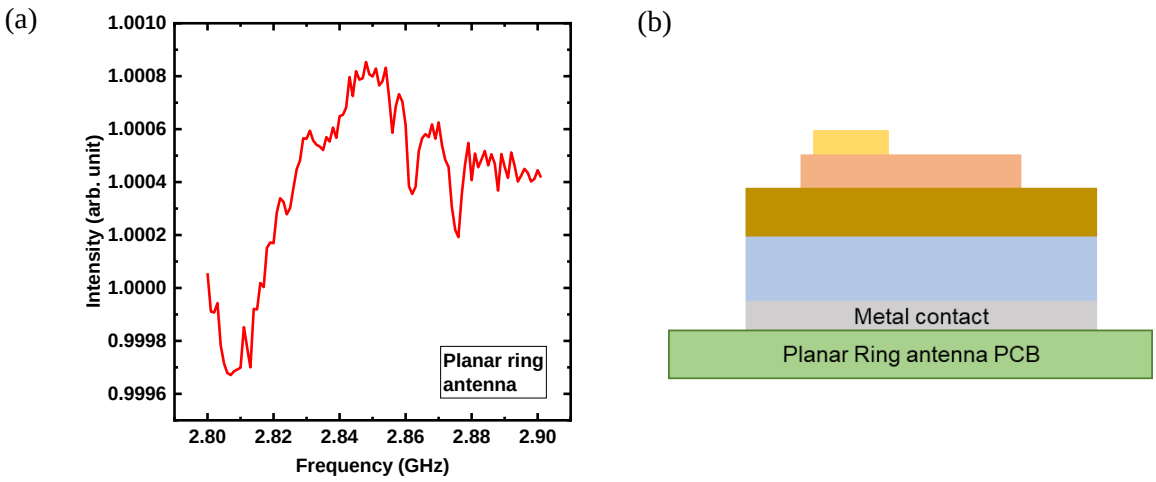

Figure 4-6 (a) ODMR spectrum of the Schottky diode using a wire-type antenna, and (b) the metal contact acting as a thin metal sheet that blocks the incoming microwave signal from the planar-ring antenna.

Thin copper wire (normally 20 μm in diameter) is the most common type of antenna that is used for spin manipulation. The key advantage is the simple design, but it has major drawbacks, such as complicated welding, easily disconnecting, and microwave radiation decreasing rapidly with distance. Conversely, the planar-ring antenna provides a better solution. Although the design is more complicated, it can avoid damage, and a smaller design can be made [14]. The planar-ring antenna produces uniform microwave distribution in a larger area, compared to the wire-type antenna, which is ideal for addressing many qubits simultaneously.

Figure 4-5 (a) shows the VDSD ODMR spectrum using the wire-type antenna, and an ODMR dip is observed, showing that it works well. However, when using the wire-type antenna, the wire must be positioned close to the NV center (shown in figure 4-5 (b)). Conversely, no ODMR dip is observed for the planar-ring-type antenna (figure 4-6 (a)). The measurements were repeated for many points within the Mo electrode area, and the results were consistent. Microwave radiation can be reflected by a metal sheet like how light is reflected by a mirror. In the case of the VDSDs, the bottom electrode acts as very thin metal sheet (figure 4-6 (b)). Any metallic structure, such as a metal wire array, has a shielding effect on microwave radiation [15] [16]. Although the ring-type antenna is preferable for exciting the NV center for a large area, the final decision is based on the diamond device structure. The ring-type antenna is not suitable for the VDSD structure used in this study; therefore, wire-type antennas were used.

4.2 Bias dependence on nitrogen-vacancy center photoluminescence spectrum

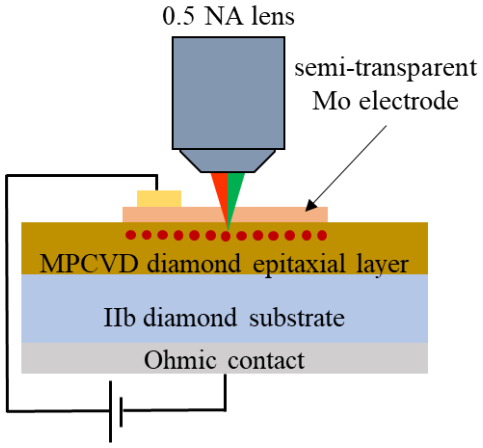

Figure 4-7 NV center located under the Mo contact. The MO is very thin to allow the excitation laser beam and the measured signal to pass through.

By using PL spectroscopy, the charge state of the NV center under different biases can be observed. The target area for the measurement of the VDSDs was under the Molybdenum (Mo) Schottky contact, where the NV center was located. This location was chosen because the NV center is directly under the influence of an electric field, as shown in figure 4-7. Because the thickness of the Mo contact is 10 nm, the excitation laser beam and measured signal can easily pass through.

.

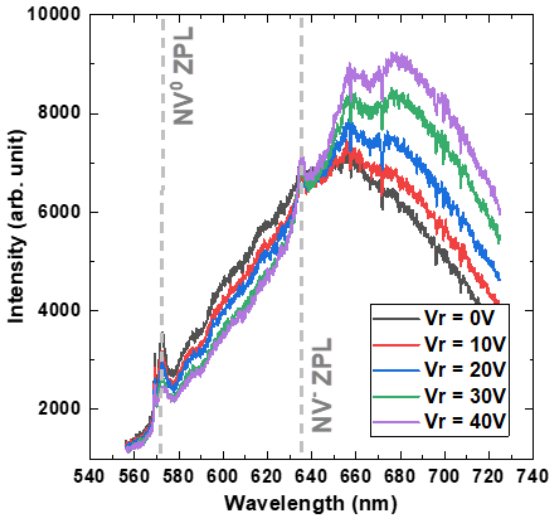

Figure 4-8 NV center PL spectrum at increasing Vr. The NV^0 PL spectrum intensity is decreasing while NV^- PL spectrum intensity is increasing.

In figure 4.3, the NV center exist in two charge states, NV^0 and NV^-. In this subsection, the electrical control of the charge state is realized. Figure 4-7 shows the effect of Vr on the VDSD PL spectrum. At 0 V, NV^0 and NV^- had zero-phonon lines (ZPL) sharp peaks of 575 nm and 637 nm and phonon sideband (PBSs) of 580–620 nm and 640–720 nm, respectively). Upon applying Vr > 0, the NV^0 ZPL and its PBS spectrum decreased, while the NV^- ZPL and its PBS increased steadily. At 0V, both NV^0 and NV^- were present, but most of the NV center was in the neutral state. This can be explained by the higher intensity count of NV^0 ZPL and PBS. By increasing Vr, most NV^0 were converted into NV^- and contributed to showing a high PL intensity of NV^- ZPL and PBS.

Figure 4-9 shows the NV^0/NV^- ratio, in which the changes in the NV center PL spectrum characteristics were caused by NV^0 that were gradually ionized into NV^- at a higher Vr, which increased the NV^- population. The NV center ratio was determined by finding the deconvoluted area of the PL spectrum that contained both NV^0 and NV^-. The ration is defined by using the following equation:

$$\boldsymbol{model} = \boldsymbol{a} \times \boldsymbol{A1}[\boldsymbol{x}] + \boldsymbol{b} \times \boldsymbol{A2}[\boldsymbol{x}] \tag{4.3}$$

where, a denotes the value of NV^0 and b denotes the value of NV^-. This conversion was related to the Fermi level shift toward the NV^- energy level, thus leading to the ionization of NV^0 into NV^-[4][18][1].

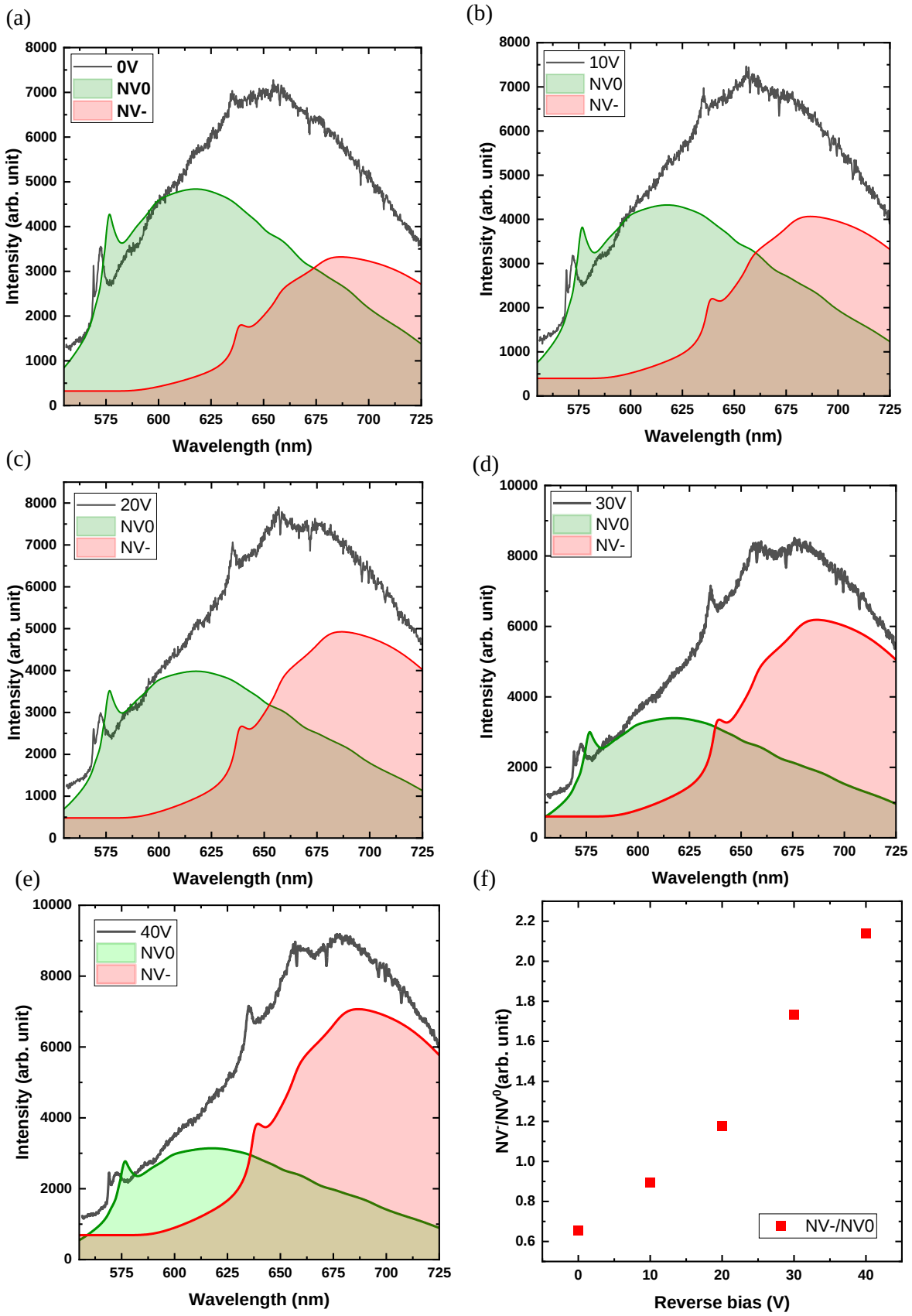

Figure 4-9 (a)–(e) NV center PL spectrum fitting results for different Vr values. The fitting was achieved by using pure NV^0 and NV^- PL spectra. (f) NV^0/NV^- ratio shows that the NV^- the population has increased at a higher Vr.

The changes of the NV center ratio indicate that NV^0 gradually changes into NV^- at higher Vr values. The charge state of the defects that exist in the semiconductor depends on the position of the Fermi level with respect to the defect-charge-transition level. This transition levels are defined as the energy levels at which the defects acquired or lost an electron [19]. For example, the $NV^{0/-}$ level indicates the defect transition from the neutral state into the negatively charge state. When the Fermi level moves above this transition levels, electrons are captured, and when it moves below it, electrons are released. The $NV^{0/-}$ charge-transition level corresponds to the NV^- ground state. The NV^- level is located in the diamond bandgap, which is 2.94 eV above the valence band maximum (VBM), and it is stable for Fermi levels between 2.8 eV and 5.2 eV [20][21]. Other than the $NV^{0/-}$ level, another charge-level transition also exists, known as $NV^{+/0}$, which is located below the $NV^{0/-}$, and it is 1.2 eV above VBM [20]. The charge-transition level is depicted in figure 4-10.

By using the charge-transition level concept, the changes in the PL spectrum of the NV center can be explained. The charge conversion of the NV center for VDSDs was actively controlled by applying biases. The bias shifted the Fermi level near the diamond surface electrically, which simultaneously introduced the surface-band bending. The applied Vr shifted the Fermi level upwards inside the depletion region, crossed the NV^- transition level, and finally converted majority of NV^0 into NV^-. Increasing Vr caused the depletion region to extend into the bulk, thus converted more NV^0 into NV^-. Therefore, the NV^- spectrum intensity increased at a higher Vr. Figure 4-10 shows the effect of Vr on the Fermi level inside the VDSD's depletion region. Figure 4-11 shows the effect of Vr on the fermi level inside the VDSDs depletion region.

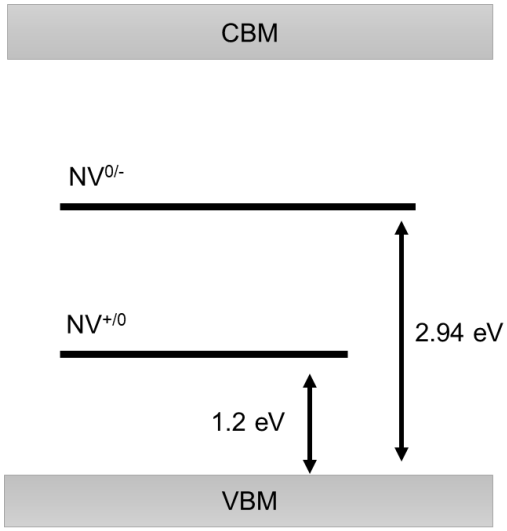

Figure 4-10 Energy level diagram of the NV center charge transition state. The $NV^{+/0}$ and $NV^{0/-}$ are located above the VBM at 1.2 eV and 2.94 eV respectively.

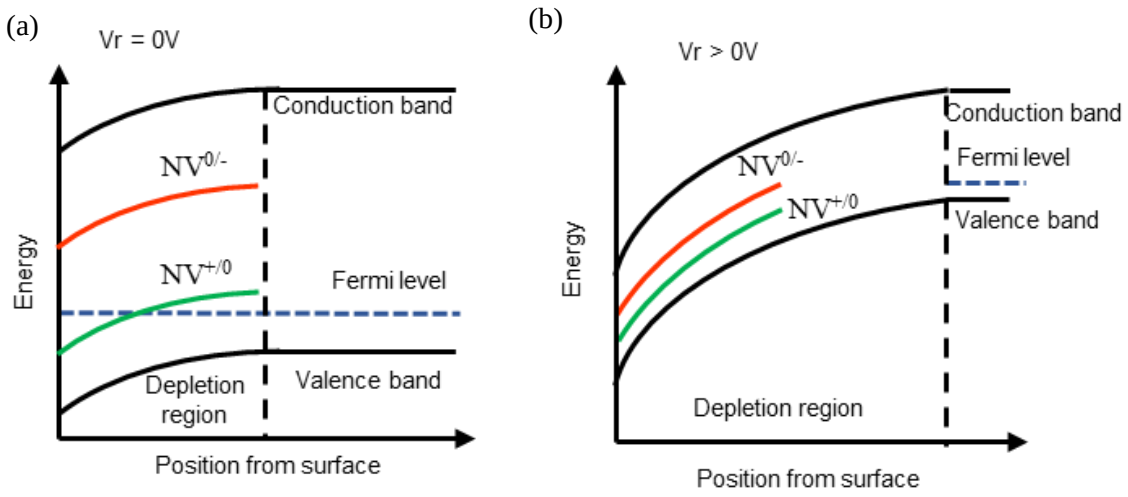

Figure 4-11 (a) NV center PL spectrum at Vr = 0V. (b) Fermi level changes inside the diode's depletion region when the applied Vr > 0V. The Fermi level crosses the NV center's charge-transition level, and this changes the charge state of the NV center. The red and green lines represent $NV^{0/-}$ and $NV^{+/0}$ charge state transition levels, respectively (The figure is modified from [2]).

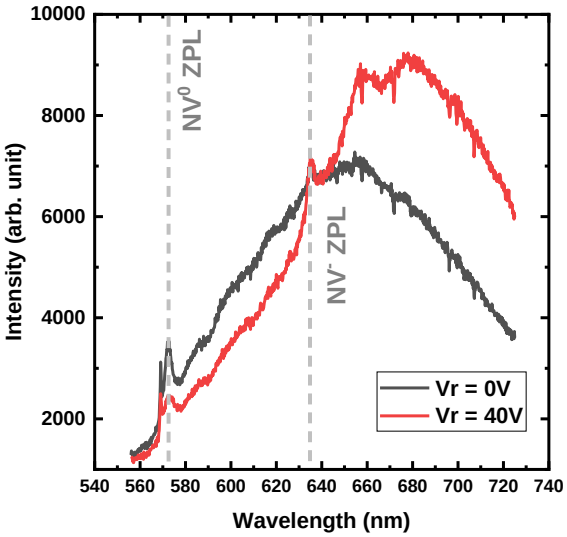

Figure 4-12 Schematic energy level diagram of the NV center's charge-transition state. $NV^{+/0}$ and $NV^{0/-}$ are located above the VBM at 1.2 eV and 2.94 eV, respectively.

Although the electrical control has succeeded in converting the charge state of the NV center, at a high Vr, the NV^- ZPL intensity is maintained, but the PBS is increased, indicating that most of the converted NV^- emission goes to PBS emission. ZPL is described as a direct emission from the electronic excited state down to the ground state. Ninety-seven percent of the light is emitted from the broad emission that is associated with the photon and phonon. The broad and strong phonon-sideband

emission is disadvantageous for the optical-based quantum system because the possibility to make a transition to the PBS is much higher compared with the ZPL transition in a two-level system. Reference [22] shows that this resonance optical transition (~637 nm) of the NV center at a low temperature (9 K) indicates that the NV center fluorescence reveals that spectrally resolved lines relate to the transition originating from specific electronic spin.

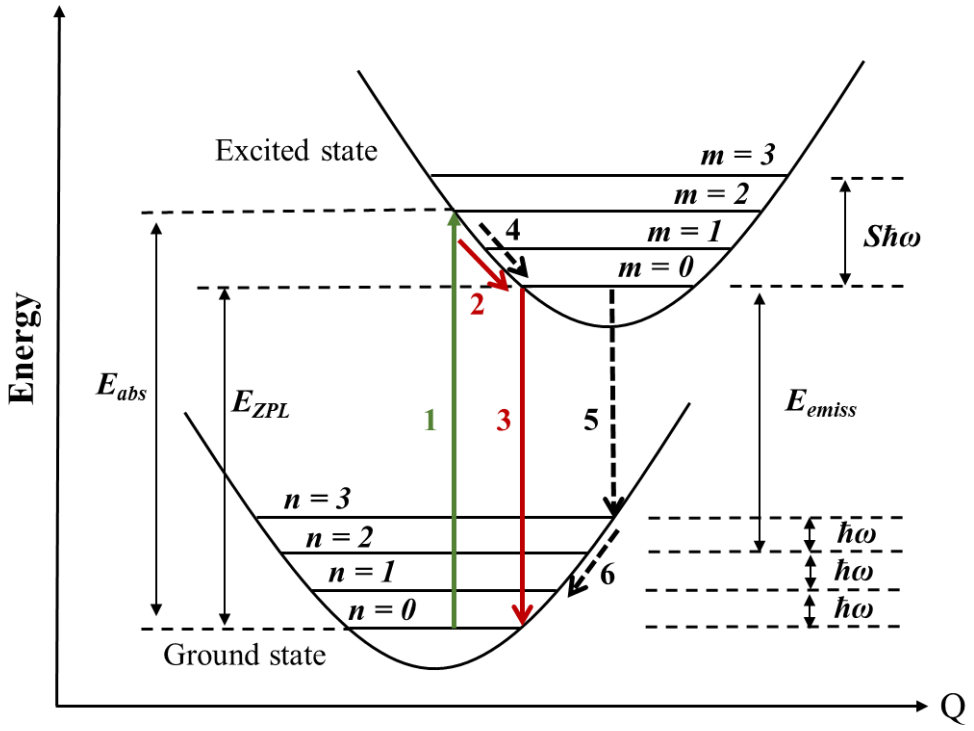

Figure 4-13 Shows the electronic structure of the NV center. For ZPLs transition process is described as process 1- 3 and for the PBS is described as transition 1, 4-6. (the diagram is modified from ref [23])

The electronic transition process in the NV center can be explained through figure 4- and normal coordinate Q represents the change in the lattice coordinate. During laser excitation, the NV center electrons will gain enough energy E_{abs} and make a transition from the ground state to a higher state (process 1). Because of the diamond crystal's thermal energy vibration, the excited electrons will release $S\hbar\omega$ energy in the form of phonons to reach the minimum excited state ($m = 0$); where, S represents the Huang-Rhys factor (process 2). The excited electron will become unstable and transition back to the ground state to recombine and release energy. If the electron makes a transition from $m = 0$ of the excited state to the $n = 0$ ground state, the ZPL of the NV center will be obtained (process 3), which determines the ZPL position in the PL spectrum. In the case of phonon emission, the excited electrons transition back to the ground state to recombine, and E_{emiss} energy will be released in the form of light (process 5). Subsequently, the ground electron can emit n phonons to release $n\hbar\omega$ energy and finally reach the most stable state (process 6). This transition process (1 until 6) explains how electrons

transition between ground and excited states [23]. Equations 4-4, and the energy relationship of the ZPLs and their phonon sideband is defined by Equations 4-5:

$$E_{abs} = E_{emiss} + S\hbar\omega + n\hbar\omega \tag{4-4}$$

$$E_{ZPL} = E_{emiss} + n\hbar\omega \tag{4-5}$$

4.3 Bias dependence on the nitrogen-vacancy center through optically detected magnetic resonance

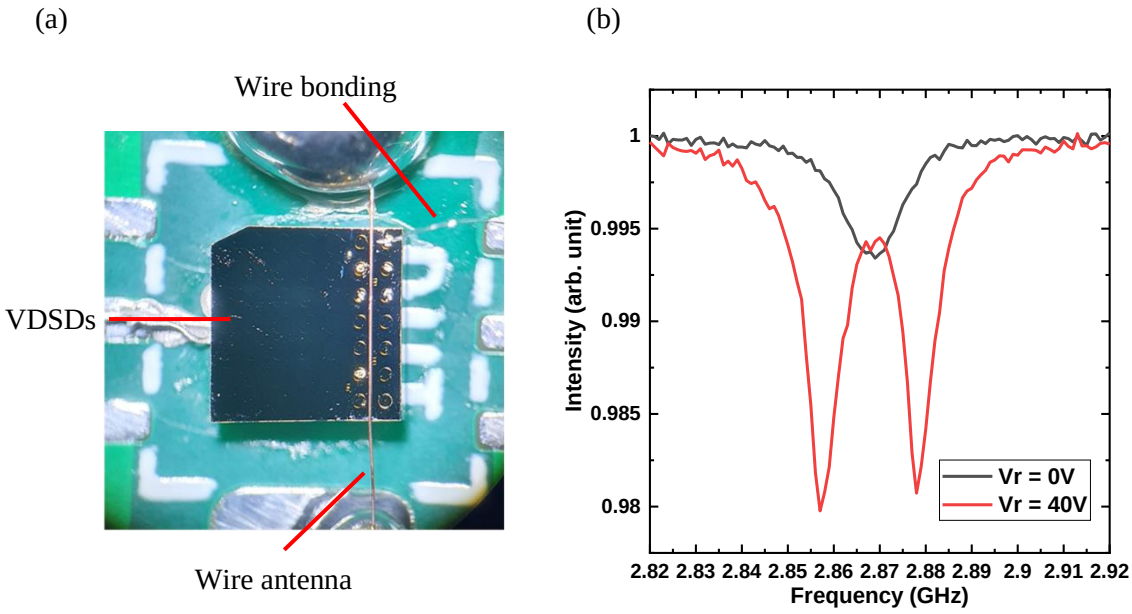

Figure 4-14 (a) VDSD with a wire-type antenna on the top part. The antenna is placed near the measuring electrode to manipulate the NV center spin. (b) Comparison of the ODMR spectrum between Vr = 0 V and 40 V, which shows a higher contrast at Vr = 40 V.

The NV center that is located inside the VDSD experience an electric field, and this can observe on the ODMR spectrum. ODMR measurements were performed and PL measurements were taken at the same location. The ODMR spectrum was measured by integrating the PL spectrum from 580 nm to 750 nm. Figure 4-14 (a) shows wire-type antenna was used for NV center spin manipulation. Figures 4-14 (b) shows the result of Vr on the ODMR spectrum. Under a high Vr value, the ODMR contrast

increased, and two distinct resonance dips were observed. The existence of these two resonance dips was related to the effect of the electric field because no magnetic field was applied during the ODMR measurements[24][25][26][27]. Moreover, the resonance contrast was related to the NV^- photoluminescence. Under high Vr, more NV^0 were converted into NV^-, thus increasing the NV^- population. Therefore, the emitted light intensity related to NV^- increased, and the ODMR contrast increased accordingly.

The NV center spin triplet ground state is sensitive to perturbations such as the magnetic field (Zeeman effect) and an electric field (Stark effect). The NV center ground state Hamiltonian under the influence of magnetic (**B** = B_x, B_y, B_z)), electrical (**E** = E_x, E_y, E_z), and strain ($\sigma = \sigma_x, \sigma_y, \sigma_z$) are described as follows [28][26]:

$$H_{gs} = H_{0gs} + H_{Bgs} + H_{Egs} + H_{\sigma gs} \tag{4.6}$$

$$\begin{aligned} H_{gs} = \left(D_{gs} + k_{Egs}^{\parallel} E_z + k_{\sigma gs}^{\parallel} \sigma_z\right) S_z^2 + \gamma_{\mu B}\, \mathrm{S.B} \\ - \left(k_{Egs}^{\perp} E_x + k_{\sigma gs}^{\perp} \sigma_x\right)\left(S_x^2 - S_y^2\right) \\ + \left(k_{Egs}^{\perp} E_y + k_{\sigma gs}^{\perp} \sigma_y\right)\left(S_x S_y - S_y S_x\right) \end{aligned} \tag{4.7}$$

where, D_{gs} = 2.88 GHz is the ground state zero field-splitting, $\gamma_{\mu B}$ = 28 $GHzT^{-1}$ is the gyromagnetic ratio, and **S** = S_x, S_y, S_z is the S = 1 spin operator. In the above equation, the magnetic, electric, and strain field vectors are oriented such that the z-axis is parallel to the symmetry axis of the NV center. Research done by Oort has determined that the electric field dipole moment (or electric field susceptibilities) for an electric field that is parallel or perpendicular to the NV center is $k_{Egs}^{\parallel}$ = 0.35 ± 0.02 Hz cm v^{-1} and $k_{Egs}^{\perp}$ = 17 ± 3 Hz cm v^{-1}, respectively. From the electric dipole moment value, the electric field perpendicular to the NV center axis will show a stronger interaction.

The ODMR split is normally related to the Zeeman effect when the NV center is under the influence of a magnetic field (example shown in the figure for 1B substrate). The interaction between the NV center triplet ground level and external magnetic field $\boldsymbol{B}$ is represented as the following Hamiltonian equation:

$$\frac{H_{int}}{h} = \frac{g_e \mu_B}{h}(\boldsymbol{B} \cdot \boldsymbol{S}) = \gamma_{NV}(\boldsymbol{B} \cdot \boldsymbol{S}) \tag{4.8}$$

where, g_e= 2.003 denotes the NV electronic Lande factor, μ_B denotes the Bohr magneton, and h is the Planck constant. The z-direction refers to the quantization axis for the NV center, which is along the nitrogen vacancy. Applying a static magnetic field $\boldsymbol{B}$ to the NV center lifted the degeneracy between $m_s = \pm 1$, and the splitting width increased with increasing magnetic field strength.

Under the influence of a magnetic field oriented along the N-V axis, where, $\boldsymbol{B_z} = (0, 0, \boldsymbol{B_z})$, the Hamiltonian is represented in matrix form as follows:

$$\frac{H_{Zeeman}}{h} = \begin{pmatrix} D + \frac{g_e \mu_B}{h} \boldsymbol{B_z} & 0 & 0 \\ 0 & 0 & 0 \\ 0 & 0 & D + \frac{g_e \mu_B}{h} \boldsymbol{B_z} \end{pmatrix} \tag{4.9}$$

with the eigenstates $m_s = 0$, $m_s = -1$, and $m_s = +1$ and magnetic field-dependent transition frequencies. When the magnetic field is applied along the z-axis, which is the nitrogen-vacancy axis, the frequency split is symmetrical and can be expressed as

$$\Delta v = \frac{2 g_e \mu_B}{h} B_z = 2 \gamma_{NV} B_z \tag{4.10}$$

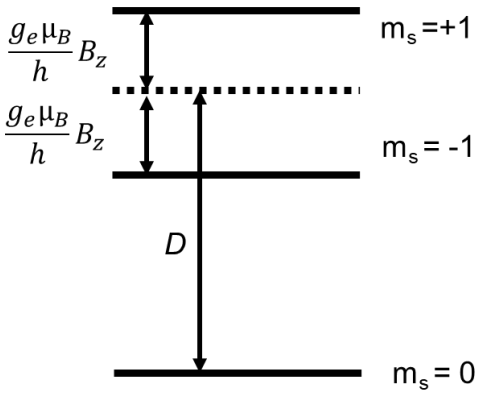

Figure 4-15 NV^- ground-energy level diagram under the influence of an external magnetic field along the N-V axis defined by Equation (4.9) resulting in symmetrical splitting of the $m_s = \pm 1$ level. (Figure modified from Reference [29])

According to reference [30], the relationship between the frequency splitting Δv and magnetic field $\boldsymbol{B_z}$ only relies on the fundamental constants, which are similar for each NV center, thus the experiment can be reproduced without the need calibrate sensors before the experiment. A large value of $2\gamma_{NV}$ also makes the NV center sensitive to a small magnetic field perturbations and can cause a measurable frequency for a magnetic field in the militesla range. When the introduced magnetic field is not along the NV center axis, the magnetic field is contributed from both the axial component ($\boldsymbol{B_z}$) and strong transverse component ($\boldsymbol{B_x}$) the splitting will be no longer be symmetrical, and the frequencies associated with the $m_s = 0$ and $m_s = \pm 1$ transitions are given (here up to the third in α) in reference [30]

$$\nu_{\pm} = D\left[1 \pm \left(\alpha\, cos\theta_B + \frac{\alpha^2}{2} 3sin^2\theta_B \pm \alpha^3\left(\frac{1}{8}sin^3\theta_B tan\theta_B - \frac{1}{2}sin^2\theta_B cos\theta_B\right)\right)\right] \tag{4.11}$$

where, $\alpha = \gamma_{NV} B/D$ and $tan\theta_B = B_x/B_z$. Recording the exact value for both frequencies, the amplitude and the orientation of the applied magnetic field can be determined, which is useful for the external magnetic field full-vector analysis.

The Stark effect occurs when there is a perturbation to the electronic orbitals because of an electric field. Like the Zeeman effect, the Stark effect causes the energy level to be split, and the effect can be observed in figure 4-14 (b). For the ODMR spectrum, no hyperfine peak was related to the 14N as reported in refence [31] [32], thus the assumption is that the splitting is caused by the electron m_s = ±1 level. One of the possible reasons is that the measurement was taken on an NV center ensemble for the VDSDs, compared to the measurement performed on a single center as done in reference[31] [32]. Nevertheless, the following equation is used to determine *E* experienced by the ensemble NV center inside the VDSDs.

For m_l = ±1

$$E_{m=\pm1,+} = \frac{1}{2}\left[2D + h_+ + h_- + \sqrt{4\left(d_{gs}^{\perp}\Pi_x\right)^2 + 4\left(d_{gs}^{\perp}\Pi_y\right)^2 + (h_- - h_+)^2}\right] \tag{4.12}$$

$$= S + P + \sqrt{\left(d_{gs}^{\perp}\Pi_{x\perp}\right)^2 + A_{\parallel}} \tag{4.13}$$

$$E_{m=\pm1,-} = \frac{1}{2}\left[2D + h_+ + h_- - \sqrt{4\left(d_{gs}^{\perp}\Pi_x\right)^2 + 4\left(d_{gs}^{\perp}\Pi_y\right)^2 + (h_- - h_+)^2}\right] \tag{4.14}$$

$$= S + P - \sqrt{\left(d_{gs}^{\perp}\Pi_{x\perp}\right)^2 + A_{\parallel}} \tag{4.15}$$

where, D denotes the ZFS, $h_+ = P + A_\parallel$, and $h_- = P - A_\parallel$. For, $m_l = 0$, the obtained splitting (W_0) of the magnetic resonant lines in the ODMR spectrum is expressed as:

$$hW_0 = E_{m=0,+} - E_{m=0,-} = 2d_{gs}^{\perp}\Pi_{\perp} \tag{4.16}$$

Thus, the final equation shows the relationship between the transverse electric field and the split width

$$\frac{d_{gs}^{\perp}\Pi_{\perp}}{h} = \frac{1}{2}W_0 \tag{4.17}$$

where, $\Pi = E + \sigma$ is the total electric field, E is the applied electric field, σ is the strain in the lattice, d_{gs} is the parallel electric dipole moment provided $d_{gs}{}^{\perp}$ to the N-V axis, and h is the Planck constant. Figure 4-16 (a) shows the ODMR spectra measured for Vr ranging from 0–40 V. The ODMR spectra exhibited resonance dips for Vr ≥ 10 V. The splitting of the resonance dip is often induced by the Zeeman effect from the magnetic field, but because there is no magnetic field applied, the splitting is caused by the electric field known as the Stark effect [33][34][35]. The Stark effect happens when there is a perturbation to the electronic orbitals due to an electric field [24]. The electric field is known to induce a shift of the optical resonance line and this phenomenon can be observed for quantum dots in the solid state, single atoms, and also single molecules [36]. The orientation of the N-V axis determines the shape of the ODMR spectrum. If the electric field is perpendicular to the N-V axis (transverse $E_\perp$), the ODMR resonance spectrum will be split, and if the electric field is parallel along the N-V axis (axial E_z), the resonance peak center will be shifted [28]. The effect of $E_\perp$on the N-V center axis is smaller than that of E_z.

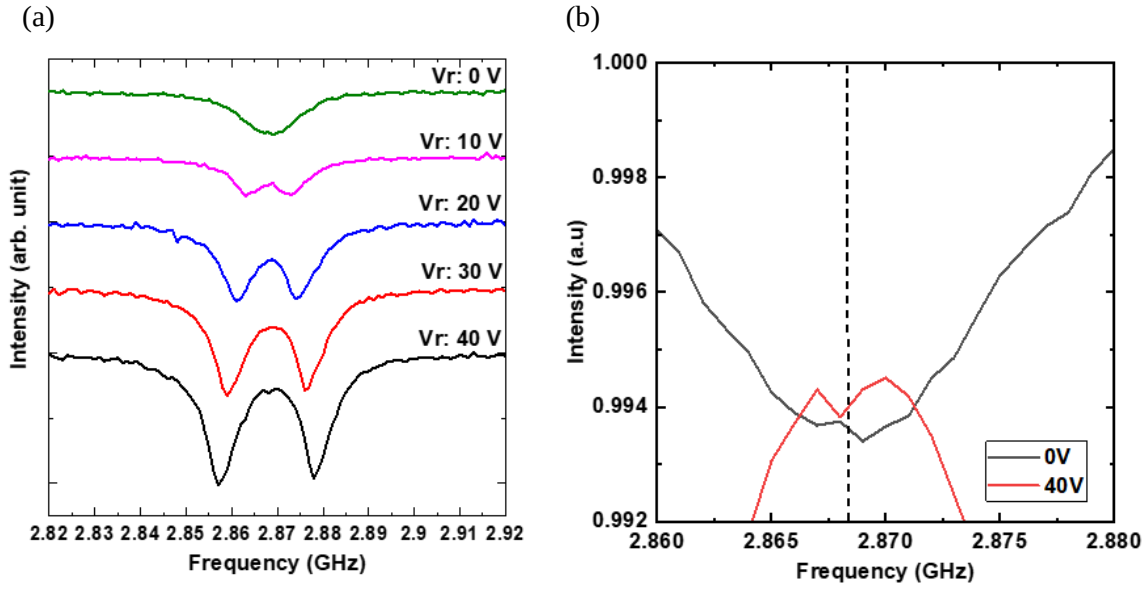

Figure 4-16 (a) ODMR spectra split into two peaks due to the Stark effect. The split becomes wider at larger Vr values. (b) the center peak shifted to a lower frequency.

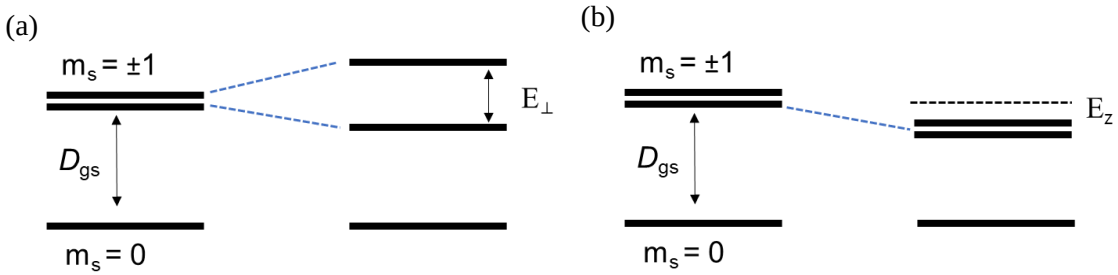

Figure 4-17 Split energy level due to a perpendicular electric field. (b) Energy level shift due to a parallel electric field.

Other than the splitting of the ODMR peak, the center peak was also shifted to a shorter frequency (figure 4-16 (b)). The shift meant that the NV center experienced an electric field that was both perpendicular and parallel to its axis [31][37]. Vr was increased to cause the internal electric field of diamond Schottky diodes to enhance the Stark effect, thus leading to the splitting of the ODMR dip [24]. The splitting of the ODMR peak and the ODMR center peak shift can be related to the splitting and shifting energy level of the NV center $m_s = \pm 1$ ground state as shown in figure 4-13 [38]. Conversely, the width of the splitting increased with Vr**.** The relationship between the splitting width and electric field is given by the following equation [31]. Because the applied electric field is much larger than the effect of the strain, the strain value is not determined. For the ODMR spectrum, no hyperfine peak was observed related to the $m_I = 0$ and $m_I = \pm 1$ of ^{14}N as reported in reference [31] [32] thus the assumption

that is made is that the splitting is caused by the NV center $m_s = \pm 1$ ground state level. The dips splitting width depends on the electric field magnitude, which depends on Vr. The electric field increased with Vr. Therefore, the dip splitting width increased with Vr as shown in figure 4-16.

The ODMR spectrum for the VDSDs is mainly caused by the external electric field, thus it is difficult to observe the effect caused by the strain. However, an explanation will be given to explain the effect of the strain on the ODMR spectrum. Other than the electric field applied externally, the internal environment of the diamond crystal can also produce a minuscule electric field near the NV center. Based on figure 3-14 (a), the 1B diamond ODMR spectrum shows a peak splitting. This splitting is commonly associated with the presence of a lattice strain [39][32]. However, another study conducted by Mittiga et al [38] mentioned that there could be another factor affecting the ODMR splitting. From his experiment, first, he observed that the line shape of the resonance is asymmetric and cannot be fitted by either Lorentzian or Gaussian. Second, the central feature between the resonance is sharper than the inhomogeneous linewidth. Third, in the presence of strong splitting, there is almost no shift of the NV center's overall spectrum. Based on this observation, he developed a microscopic charge model based on the randomly positioned charges inside the diamond lattice. The reason behind this model is that each NV^- behaves as an electron acceptor and a positively charged electron donor (positive P1 center). These charges will create an electric field (behaving like strain) and couple to the $m_s = \pm 1$ states, leading to the splitting of the eigenstates. Based on this assumption, he developed a technique to image the local charge surrounding the NV center

Using Equation 4-6, we estimated the electric field sensed by the NV centers. This calculation was performed by considering the mismatch between the NV center's axis (111 direction) and the electric field direction (001) as shown in Figure 4-18. An offset angle of θ (54.7°) exists between the electric field direction and the NV centers axis (see Figure 4-16) [40]. Thus, the real value of the electric field is given by $E = E\perp/sin\,(\theta)$.

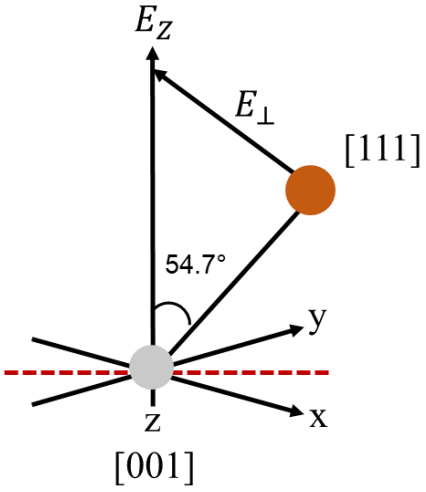

Figure 4-18 Relationship between the NV center axis and electric field $\vec{E}$ direction. The gray and orange circles represent the vacancy and nitrogen atom, respectively.

Figure 4-19 shows the electric field sensing of NV centers, calculated using the Stark effect. The measured E_{ODMR} from ODMR has been compared to the electric field (E_{CV}) extracted using capacitance (C-V) measurements.

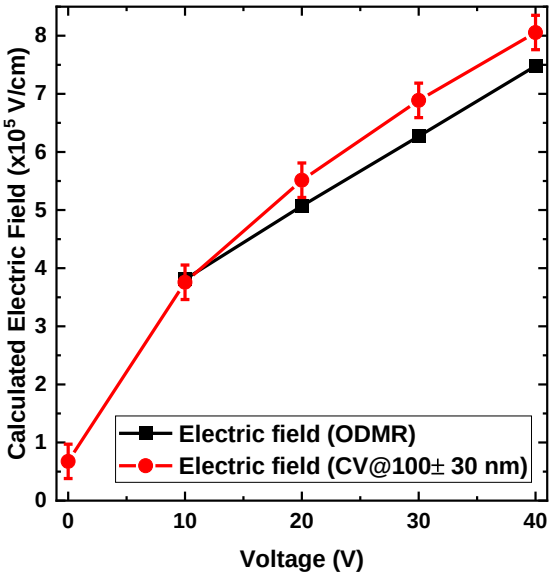

Figure 4-19 Electric field calculation comparison from Stark effect and CV measurement.

E_{CV} was calculated using the following equation:

$$E_{CV}(x) = \frac{qN_A}{\varepsilon_0\varepsilon_r}(W - x), \qquad 4\text{-}18$$

where, W is the depletion width, x is the position depth of the NV centers, $\varepsilon_0 = 8.85\times10^{-14}$ F/cm^2 is the vacuum permittivity, $\varepsilon_r = 5.7$ is the diamond permittivity, Vr is the applied reverse voltage, V_{bi} = 1.4 eV is the built-in potential barrier of the diamond Schottky diode [1], $q = 1.6 \times 10^{-19}$ C is the electron charge, and N_A is the effective acceptor's density. Moreover, the depletion W is defined by:

$$W = \sqrt{\frac{2\varepsilon_0\varepsilon_r(V_r + V_{bi})}{qN_A}} \qquad 4\text{-}19$$

By substituting Equation (2) into Equation (3), the following equation is derived:

$$E_{CV}(x) = \frac{qN_A}{\varepsilon_0\varepsilon_r}\left[\sqrt{\frac{\varepsilon_0\varepsilon_r(V_r+V_{bi})}{qN_A}} - x\right], \qquad 4\text{-}20$$

Thus, the parameters needed to calculate the electric field E_{CV} were N_A and V_r. N_A of approximately 3.11×10^{16} cm^{-3} was estimated using the 1/C^2 -V characteristics (see figure 4-2).

Based on the SRIM simulation, most NV centers are assumed to be located 100 nm below the Mo Schottky electrode. The calculated E_{CV} at 100 nm was close to the value extracted using the ODMR spectrum. Assuming an error of 30 nm on the position of NV centers, i.e. 100 ±30 nm, the small difference between E_{ODMR} and E_{CV} can be explained. This difference was close to the error bar related to the uncertainty of the NV center's exact position. Moreover, the difference between E_{ODMR} and E_{CV} could be related to several factors. In Equation (1), the total electric field Π is a combination of the applied electric field E and the strain σ of the NV center. E_{ODMR} shown in 4-10 included the effect strain on the NV centers. Moreover, Nitrogen-ion implantation introduced additional nitrogen-related defects that could affect the electric field locally in the vicinity of NV centers [1]. Furthermore, E_{ODMR} was calculated based on the assumption that the NV center was located at 100 nm in bulk, but the nitrogen-ion implantation could lead to the creation of vacancies, and the post-implantation annealing could make the nitrogen atoms and vacancies diffuse deeply into the bulk [17][41]. Thus, ODMR splitting from figure 4-11 may not measure the electric field exactly at 100 nm depth.

4.4 Conclusion

In summary, PL spectroscopy and ODMR were performed on a nitrogen-ion-implanted VDSD simple structure.

Two charges state can be observed for this sample, which are NV^0 and NV^-. The existence of the NV^0 states may be caused by the side effect of surface-defect damage during ion implantation. For spin manipulation, only NV^- is needed, thus electrical characterization was performed to increase the NV^- state population. NV^0 is converted into NV^- at a higher bias, contributing more to PL emission. The NV^0 PL spectrum still appears even though the depletion region extends beyond the ion-implantation layer. The reason for this is still unclear, but it is assumed that a small part of NV^- has been ionized by the laser excitation during constant illumination in the CW mode. The vertical-type Schottky diode that was used in this study can control the NV center charge state, and the thin electrode design allow the excitation laser beam and PL signal to pass through.

ODMR splitting has been observed due to the effect of the electric field that exists inside the VDSD's depletion region. The NV center Hamiltonian ground state demonstrates that the NV center can be affected by an electrical influence and cause the splitting and shift of the energy level. The estimated electric field value calculated from ODMR splitting shows an almost similar value to the C–V measurement. The ODMR spectrum consisted of an ensemble NV center that can affect the ODMR spectrum by broadening or shifting the frequency, which may affect the real measured value. By increasing the concentration of NV^- near the surface, it is possible to increase the NV center's device sensitivity [42].

The first silicon-based solid-state quantum was proposed by Kane from the University of New South Wales in 1998 [43]. He proposed that in ion implantation, the donor atom, which is phosphorus, is implanted into an array formation into the silicon chip. These phosphorus atoms become the basic building blocks of qubits. An electrode that acts as a "gate" to control the spin is fabricated directly on top of the embedded phosphorus atoms. The overall structure is quite simple, as shown in figure 1 from reference [43]. Because diamond is also considered a solid-state material, a standard silicon nanofabrication process can be applied to diamonds. Similar to the vertical type used in this study, the NV center's charge state is directly controlled by the electrode on the top. By using a mask, it is possible to make a small aperture hole such that only few NVs are created during the implantation process. According to reference [43], a mask with a diameter hole of 2.5 μm creates an NV center with an average number of five, and a diameter hole of 1.5 μm creates an NV center with an average number of 1-2. The nitrogen can be implanted into an array to form a quantum register. Using the standard nanofabrication technique, a miniature electrode can be fabricated on the array of the NV center for charge state manipulation or electrical readout. An antenna for spin manipulation can also be fabricated near the proximity of the NV center. Indeed, the vertical-type diode has many advantages for quantum applications.

4.6 References

[1] J. Guo *et al.*, "Study of ion-implanted nitrogen related defects in diamond Schottky barrier diode by transient photocapacitance and photoluminescence spectroscopy," *Jpn. J. Appl. Phys.*, vol. 60, 2021.

[2] J. Guo, "Study of nitrogen-vacancy centers in diamond Schottky barrier diode," University of Tsukuba, 2022.

[3] A. Nawawi, K. J. Tseng, Rusli, G. A. J. Amaratunga, H. Umezawa, and S. Shikata, "Characterization of vertical Mo/diamond Schottky barrier diode from non-ideal I-V and C-V measurements based on MIS model," *Diam. Relat. Mater.*, vol. 35, pp. 1–6, 2013.

[4] C. Schreyvogel, V. Polyakov, R. Wunderlich, J. Meijer, and C. E. Nebel, "Active charge state control of single NV centres in diamond by in-plane Al-Schottky junctions," *Sci. Rep.*, vol. 5, no. July, 2015.

[5] F. Jelezko and J. Wrachtrup, "Single defect centres in diamond: A review," *Phys. Status Solidi Appl. Mater. Sci.*, vol. 203, no. 13, pp. 3207–3225, 2006.

[6] M. W. Doherty, N. B. Manson, P. Delaney, F. Jelezko, J. Wrachtrup, and L. C. L. Hollenberg, "The nitrogen-vacancy colour centre in diamond," *Phys. Rep.*, vol. 528, no. 1, pp. 1–45, 2013.

[7] J. W. Steeds and S. Kohn, "Annealing of electron radiation damage in a wide range of Ib and IIa diamond samples," *Diam. Relat. Mater.*, vol. 50, pp. 110–122, 2014.

[8] A. You, M. A. Y. Be, and I. In, "Conversion of neutral nitrogen-vacancy centers to negatively charged nitrogen- vacancy centers through selective oxidation," vol. 121907, no. 2010, pp. 1–4, 2012.

[9] F. Gorrini *et al.*, "Photoconversion of shallow nitrogen-vacancy centers in flat and nanostructured diamond under high-power laser irradiation," *arXiv Prepr. arXiv2105.04939*, pp. 1–18, 2021.

[10] T. Gaebel *et al.*, "Photochromism in single nitrogen-vacancy defect in diamond," *Appl. Phys. B Lasers Opt.*, vol. 82, no. 2 SPEC. ISS., pp. 243–246, 2006.

[11] C. Santori, P. E. Barclay, K. M. C. Fu, and R. G. Beausoleil, "Vertical distribution of nitrogen-vacancy centers in diamond formed by ion implantation and annealing," *Phys. Rev. B - Condens. Matter Mater. Phys.*, vol. 79, no. 12, pp. 1–8, 2009.

[12] R. Löfgren, S. Öberg, and J. A. Larsson, "A theoretical study of de-charging excitations of the NV-center in diamond involving a nitrogen donor," *New J. Phys.*,

vol. 22, no. 12, 2020.

[13] K. Groot-Berning *et al.*, “Passive charge state control of nitrogen-vacancy centres in diamond using phosphorous and boron doping,” *Phys. Status Solidi Appl. Mater. Sci.*, vol. 211, no. 10, pp. 2268–2273, 2014.

[14] L. Qin *et al.*, “Near-field microwave radiation function on spin assembly of nitrogen vacancy centers in diamond with copper wire and ring microstrip antennas,” *Jpn. J. Appl. Phys.*, vol. 57, no. 7, 2018.

[15] T. Tsutaoka, U. Hasanah, A. Tsurunaga, T. Umeda, and K. Shimizu, “Demonstration of Electromagnetic Shielding Using Metal Wire Array Composite Structures.”

[16] S. Bhattacharjee, “Protective Measures to Minimize the,” *Adv. Electron. Electr. Eng.*, vol. 4, no. 4, pp. 375–380, 2014.

[17] A. Haque and S. Sumaiya, “An Overview on the Formation and Processing of Nitrogen-Vacancy Photonic Centers in Diamond by Ion Implantation,” *J. Manuf. Mater. Process.*, vol. 1, no. 1, p. 6, 2017.

[18] C. Schreyvogel, M. Wolfer, H. Kato, M. Schreck, and C. E. Nebel, “Tuned NV emission by in-plane Al-Schottky junctions on hydrogen terminated diamond,” *Sci. Rep.*, vol. 4, pp. 1–6, 2014.

[19] B. Grotz *et al.*, “Charge state manipulation of qubits in diamond,” *Nat. Commun.*, vol. 3, 2012.

[20] C. Schreyvogel, V. Polyakov, R. Wunderlich, J. Meijer, and C. E. Nebel, “Active charge state control of single NV centres in diamond by in-plane Al-Schottky junctions,” *Sci. Rep.*, vol. 5, pp. 1–12, 2015.

[21] J. R. Weber *et al.*, “Quantum computing with defects,” *Proc. Natl. Acad. Sci. U. S. A.*, vol. 107, no. 19, pp. 8513–8518, 2010.

[22] L. Childress and R. Hanson, “Diamond NV centers for quantum computing and quantum networks,” *MRS Bull.*, vol. 38, no. 2, pp. 134–138, 2013.

[23] R. Guo, K. Wang, Y. Tian, and H. Wang, “Nitrogen vacancy luminescence and their phonon sidebands characteristics in nitrogen-doped diamond,” *J. Alloys Compd.*, vol. 924, 2022.

[24] E. Van Oort and M. Glasbeek, “Electric-field-induced modulation of spin echoes of N-V centers in diamond,” *Chem. Phys. Lett.*, vol. 168, no. 6, pp. 529–532, 1990.

[25] D. Rohner *et al.*, “(111)-Oriented, Single Crystal Diamond Tips for Nanoscale Scanning Probe Imaging of Out-of-Plane Magnetic Fields,” *Appl. Phys. Lett.*, vol. 115, no. 19, 2019.

[26] M. W. Doherty *et al.*, “Theory of the ground-state spin of the NV - center in diamond,” *Phys. Rev. B - Condens. Matter Mater. Phys.*, vol. 85, no. 20, pp. 1–21, 2012.

[27] K. Bian *et al.*, “Nanoscale electric-field imaging based on a quantum sensor and its charge-state control under ambient condition,” *Nat. Commun.*, vol. 12, no. 1, pp. 1–9, 2021.

[28] F. Dolde *et al.*, “Electric-field sensing using single diamond spins,” *Nat. Phys.*, vol. 7, no. 6, pp. 459–463, 2011.

[29] P. Kehayias *et al.*, “Imaging crystal stress in diamond using ensembles of nitrogen-vacancy centers,” *Phys. Rev. B*, vol. 100, no. 17, pp. 1–8, 2019.

[30] Technical Note, “Fundamentals of magnetic field measurement with NV centers in diamond Related products: Qnami ProteusQ™, Quantilever™MX,” no. December, pp. 1–6, 2020.

[31] T. Iwasaki *et al.*, “Direct Nanoscale Sensing of the Internal Electric Field in Operating Semiconductor Devices Using Single Electron Spins,” *ACS Nano*, vol. 11, no. 2, pp. 1238–1245, 2017.

[32] S. Knauer, J. P. Hadden, and J. G. Rarity, “In-situ measurements of fabrication induced strain in diamond photonic-structures using intrinsic colour centres,” *npj Quantum Inf.*, vol. 6, no. 1, pp. 2–7, 2020.

[33] P. Neumann *et al.*, “Excited-state spectroscopy of single NV defects in diamond using optically detected magnetic resonance,” *New J. Phys.*, vol. 11, 2009.

[34] L. M. Pham *et al.*, “Enhanced metrology using preferential orientation of nitrogen-vacancy centers in diamond,” *Phys. Rev. B - Condens. Matter Mater. Phys.*, vol. 86, no. 12, pp. 1–5, 2012.

[35] N. Diep Lai, D. Zheng, F. Treussart, and J.-F. Roch, “Optical determination and magnetic manipulation of a single nitrogen-vacancy color center in diamond nanocrystal,” *Adv. Nat. Sci. Nanosci. Nanotechnol.*, vol. 1, no. 1, p. 015014, 2010.

[36] P. Tamarat *et al.*, “Stark shift control of single optical centers in diamond,” *Phys. Rev. Lett.*, vol. 97, no. 8, pp. 1–4, 2006.

[37] F. Dolde *et al.*, “Electric-field sensing using single diamond spins,” *Nat. Phys.*, vol. 7, no. 6, pp. 459–463, 2011.

[38] T. Mittiga *et al.*, “Imaging the Local Charge Environment of Nitrogen-Vacancy Centers in Diamond,” *Phys. Rev. Lett.*, vol. 121, no. 24, pp. 1–12, 2018.

[39] M. Simanovskaia, K. Jensen, A. Jarmola, K. Aulenbacher, N. Manson, and D. Budker, “Sidebands in optically detected magnetic resonance signals of nitrogen vacancy

centers in diamond," *Phys. Rev. B - Condens. Matter Mater. Phys.*, vol. 87, no. 22, pp. 1–11, 2013.

[40] S. Pezzagna, B. Naydenov, F. Jelezko, J. Wrachtrup, and J. Meijer, "Creation efficiency of nitrogen-vacancy centres in diamond," *New J. Phys.*, vol. 12, 2010.

[41] J. O. Orwa *et al.*, "Engineering of nitrogen-vacancy color centers in high purity diamond by ion implantation and annealing," *J. Appl. Phys.*, vol. 109, no. 8, 2011.

[42] A. Bhaumik, R. Sachan, and J. Narayan, "Tunable charge states of nitrogen-vacancy centers in diamond for ultrafast quantum devices," *Carbon N. Y.*, vol. 142, pp. 662–672, 2019.

[43] B. E. Kane, "A silicon-based nuclear spin quantum computer," *Nature*, vol. 393, no. 6681, pp. 133–137, 1998.

Chapter 5

Low-temperature Schottky diode ODMR measurement

5.1 Introduction

In this chapter, a low-temperature experiment was performed to study the behavior of the VDSD's NV center in a cryogenic environment. Temperature can affect semiconductor behavior in a sense of thermal energy, and it can excite the electrons from the valence band to the conduction band, which can lead to an increased nonradiative transition. This nonradiative transition also can lead to the creation of phonons. These phonons, also known as lattice vibration, can interact with charge carriers and broaden the material energy levels and thus make it hard to study and understand the materials. At low temperatures, the PL signal of the studied material can strongly increase and narrow spectrally.

5.2 Low-temperature experiment setup

A low-temperature experiment can be conducted by placing the samples inside a closed-cycle cryostat, which is like a refrigerator. The coolant used in our setup is liquid helium. the lowest temperature that we can obtain for our setup is 30 K. To conduct ODMR, an MW signal is required for spin manipulation, but the cryostat that we used in our setup was not designed to deliver MW into the cryostat chamber. Thus, a new method is required to deliver the MW signal as efficiently as possible.

5.2.1 Resonance inductive coupling concept

One of the best methods is to wirelessly transfer the MW signal into the cryostat chamber from the outside by using the concept of "resonance inductive coupling" (RIC). Compared with the simple wire-type antenna, which is simple and easy to use, the RIC method requires several parameters that need to be considered for efficient MW power delivery which is 1) The transmitter and receiver ring size, 2) distance between the coils, 3) obstacle between the coil, 4) the alignment between the coil and 5) available power.

Wireless power transfer can be classified into two, nonradiative (short-range transmission: such as capacitive coupling techniques, magnetic inductive coupling, and RIC) and radiative (long-range transmission: using MW and light wave techniques) [1][2]. This research will only focus on RIC because it has a longer transmission distance and better efficiency, compared to other nonradiative techniques. RIC delivers energy by through the concept of magnetic field induction between two coils, which are the transmitter coil (L_1) and the receiver coil (L_2).

5.2.2 Designing the MW resonators geometry

The structure of resonators used in this research is based on a split-ring resonator with a single large loop that carries the inductive load L and a gap that supplies capacitive load C for resonance frequency and represented by the following equation [3]:

$$f = \frac{1}{2\pi\sqrt{LC}} \tag{5.1}$$

The resonators are operated at the same resonance frequency for maximizing power transfer between the MW transmitter and receiver. The diameter of the resonator is determined according to the operating distance between the MW transmitter and receiver.

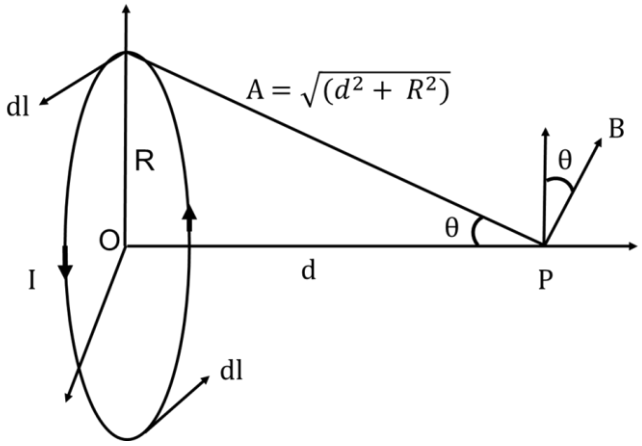

Figure 5-1 Determining the magnetic field at point P along the axis perpendicular to the wire loop.

According to the Biot-Savart law, the magnitude of a magnetic field for a single coil is represented by the following equation.

$$H = \frac{I_{MW}R^2}{2\sqrt{(R^2 + d^2)^3}} \tag{5.2}$$

where R is the average radius of the loop, I_{MW} is the MW current flowing in the loop and d is the current flowing through the loop. By deriving equation 5.1, the best radius to produce the highest magnetic field from the MW receiver is represented by the following equation:

$$H = \frac{I_{MW}R^2}{(R^2 + d^2)^{3/2}} + \frac{3I_{MW}R^3}{2(R^2 + d^2)^{5/2}} \tag{5.2}$$

which is solved for

$$R = \sqrt{2}d \tag{5.3}$$

By using equation 5.3 it is found that the MW receiver can be placed at a distance d ~ 6 -12 mm (shown in figure 5.2), for the loop diameter of $2R$ = 17- 34 mm.

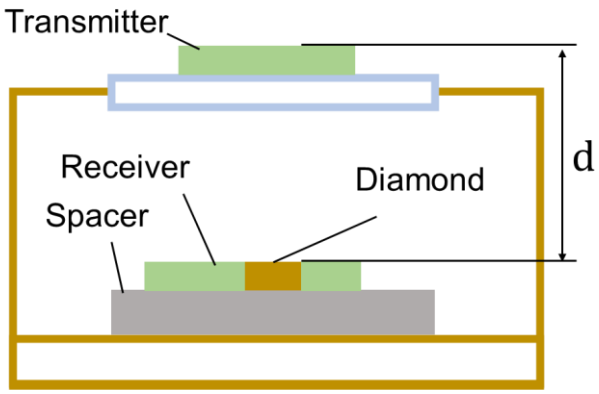

Figure 5-2 shows the distance between the MW transmitter and the MW receiver.

5.3 MW transmitter and MW receiver parameter

The cryostat window used in the setup has a diameter of 20 mm, which limits the diameter size of the MW transmitter. The MW transmitter is based on a double-gap ring resonator with a diameter of 15.4 mm [4]. The double gap behaves as a capacitor. Figure 4.3 shows both the MW transmitter and receiver fabricated from an RF4 printed circuit board (PCB). The MW transmitter and receiver have thicknesses of 1.6 mm and 0.6 mm, respectively. A square hole with 3 × 3 × 3 mm^3 dimensions was made near the thin trace for the MW receiver to accommodate the diamond substrate. The thin trace, which has a width of 0.15 mm, can emit a high MW magnetic field to excite the NV center in the diamond substrate that was placed near this thin trace because of its half-length, where the magnetic field intensity is maximum. The measured resonance frequencies for both the MW transmitter and receiver are 2.867 GHz and 2.880 GHz, respectively [4].

(a) (b)

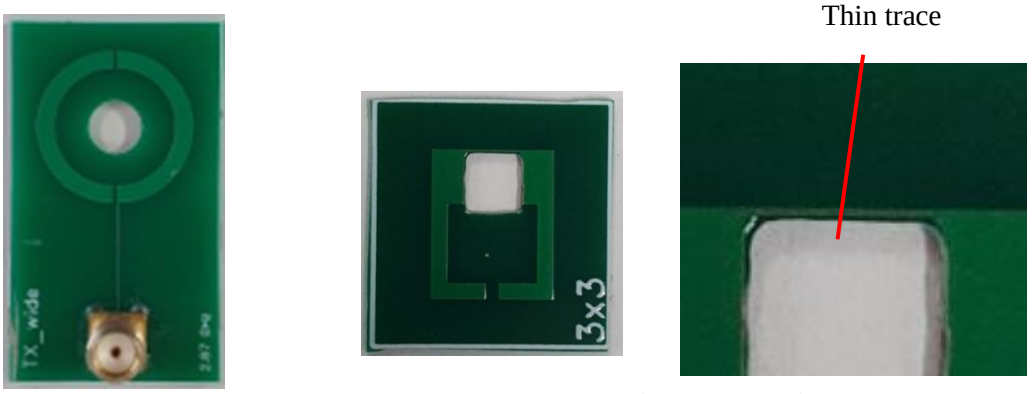

(MW transmitter) (MW receiver)

Figure 5-3 (a) Picture of the MW transmitter and MW receiver that were fabricated from FR-4 PCB with a permittivity of 4.5. (b) the zoom-in picture of the MW receiver shows a square hole that accommodates the diamond sample and the thin trace that emits a high magnetic field.

To test both MW resonators, a PL and ODMR spectrum of the 1B diamond substrate was measured as a reference. The experiment setup is shown in figure 5-4 (a), and the experiment was conducted at room temperature. A spacer with thicknesses of 1, 2, 3, 4, 5, and 6 mm was used to study the effect of the sample height on the coupling strength between both resonators. In figure 5-4 (b), it is shown that the PL intensity increased when the sample height increased from the cryostat stage because of better photon-collection efficiency when the sample is near the objective lens. The ODMR spectrum was also observed with an increasing intensity, which is shown in figure 5-4 (b). The high photon-collection efficiency contributed to a higher ODMR contrast. The obtained ODMR spectrum showed that both MW resonators function properly.

(a)

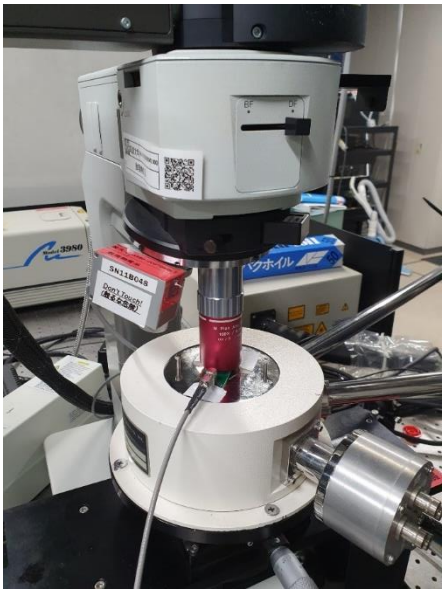

(b)

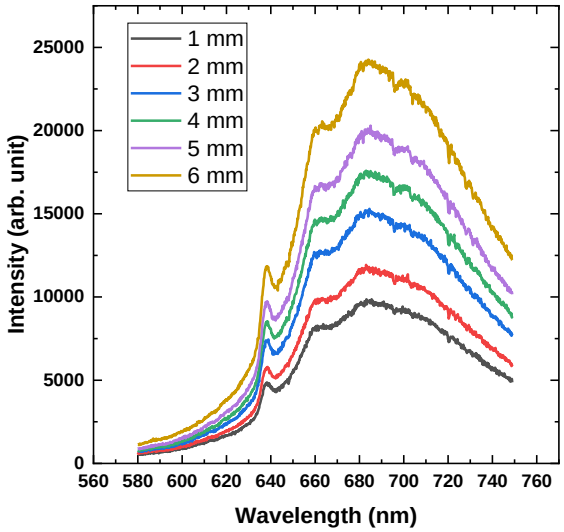

(c)

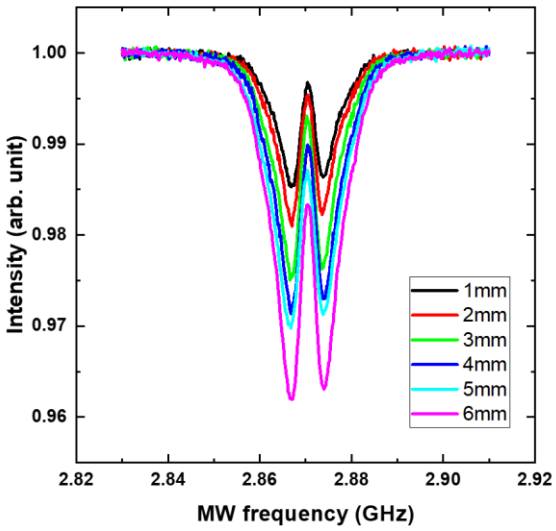

Figure 5-4 (a) ODMR setup for the cryostat. (b) the 1B diamond substrate PL spectrum with different sample positions (height range from 1, 2, 3, 4, 5, and 6 mm) from the cryostat stage. (c) ZFS ODMR of the 1B diamond substrate.

5.4 Schottky diode low-temperature experiment

For the Schottky diode low-temperature measurement, a similar 1B diamond substrate experimental setup was used but this time the 1B diamond substrate was replaced with VDSDs. The VDSDs were wire-bonded to the gold substrate. The normal wire was used to connect the gold substrate to the diode electrical pins as shown in the figure 5-4.

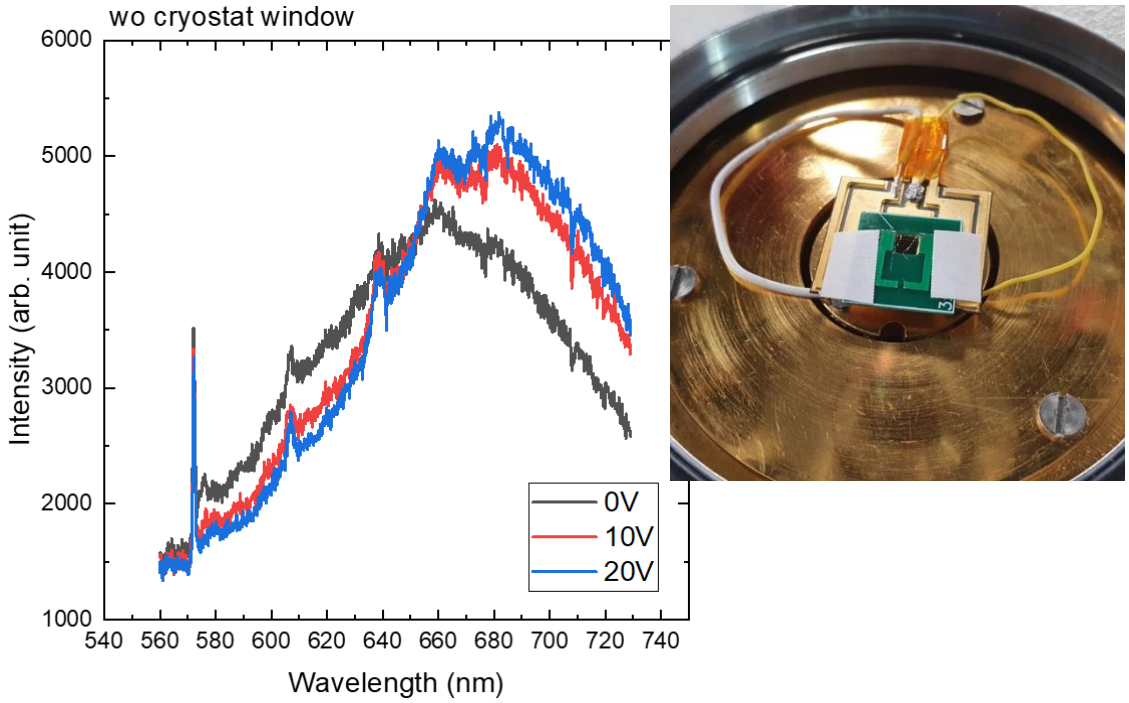

Figure 5-4 VDSD placed inside the MW receiver hole and wire-bonded to a gold substrate for electrical contact with the normal wire used to connect the gold substrate to the cryostat electrical pin. Inset shows VDSDs with wire connection.

Measurements for PL and ODMR were taken at the electrode with a nitrogen-ion-implanted region. The VDSD's PL spectrum under different Vr values was taken to observe the NV center's PL characteristics under open conditions (without a cryostat window), and the results are shown in figures 5-5. The results show that the PL spectrum changed when the NV^- PBS increased, and NV^0 PBS decreased when Vr was applied from 0 V until 20 V, meaning that the electrical connection is in good condition.

Then cryostat window was placed on top of the cryostat, then the PL spectrum was measured again at Vr = 0 V and 20 V at RT to observe the effect of the cryostat window transparency. As shown in figures 4-5 (a) the PL change is not significant between 0 V and 20 V. This result mean that the cryostat window significantly reduces the PL. ODMR was performed at the same location where the PL was taken but no ODMR spectrum was observed. ODMR measurements are based on the collection of the NV^- photon emission but because of a very low PL intensity (figure 4-5(a)) this could be a factor affecting the ODMR measurements.

(a)

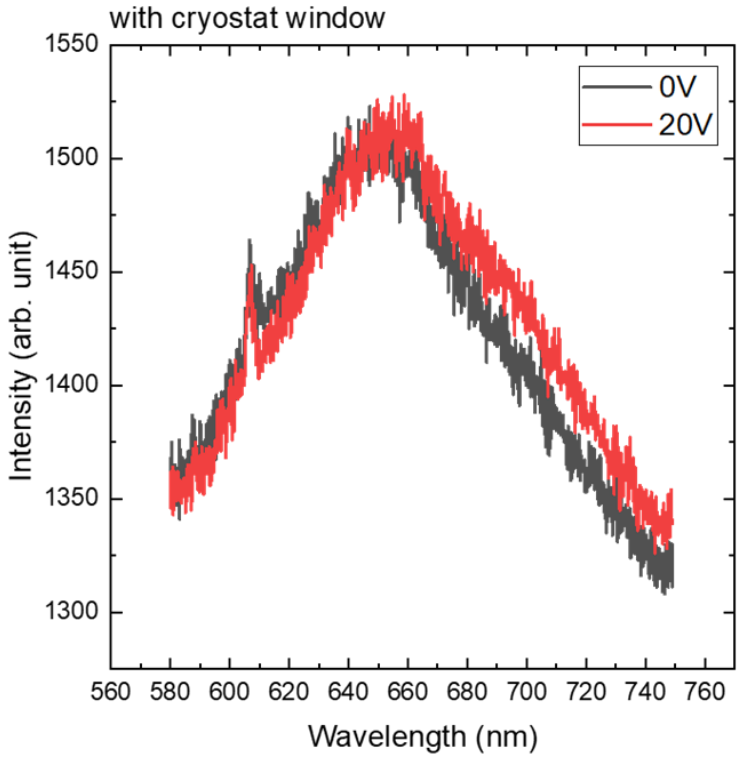

(b)

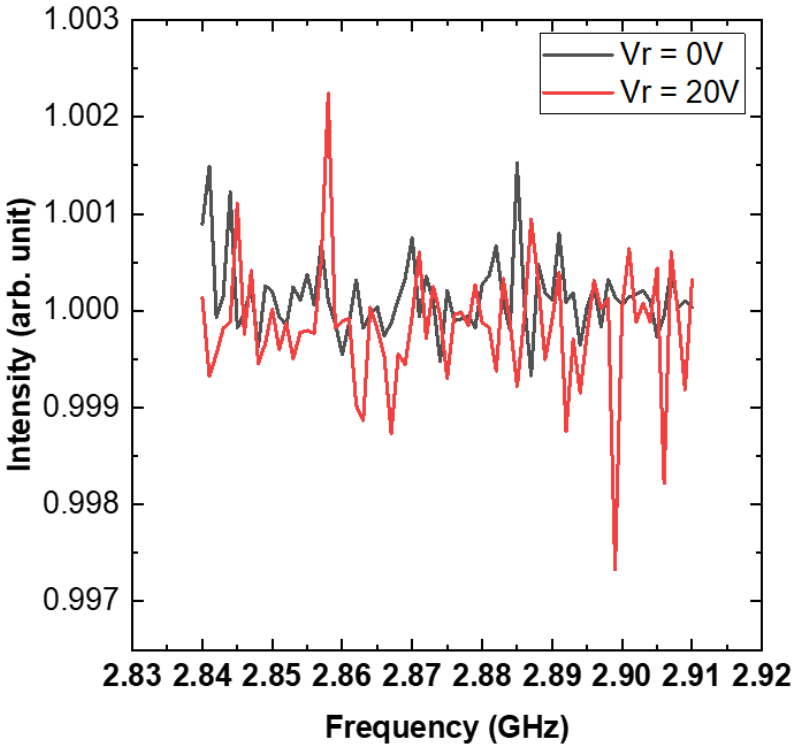

Figure 5-5 (a) shows the VDSDs PL spectrum inside the cryostat with a window that shows reduce PL signal. (b) no ODMR spectrum was observed even at Vr = 20V.

Previously, the VDSDs PL spectrum at RT has a low intensity. The PL shape and intensity can be increased at low temperatures. Figure 4-6 shows the temperature-dependent PL measurement that

was performed at the ion-implanted electrode. As expected, at 300 K, the PL intensity is low with a broad-spectrum characteristic. This can be related to the suppression of NV center fluorescence emission caused by strong phonon scattering [5]. Two peaks were observed: at 572 nm, corresponding to the first-order Raman peak, and 608 nm, which cannot be identified [6]. When the temperature slowly decreased to 54 K, the PL characteristic started to change. The NV^0 and NV^- ZPL peaks, which were at 572 nm and 573 nm started to appear [7][8]. The NV^0 ZPL shows the highest intensity until it overlaps with the Raman, peak whereas the NV^- ZPL only shows small intensity changes. A small peak also appeared at 608 nm. This peak is related to a phonon-related photon sideband of NV^0 with an energy shift of 45 meV [5].

At low temperatures, the NV center PL slightly increases; therefore, another ODMR measurement was performed at the same position, and the results are shown in figure 4-7. Although the PL intensity increased, the ODMR pattern was still not observed. It is not clear why no ODMR spectrum was observed, but it is likely caused by several reasons. First, the NV center fluorescence is not enough for ODMR detection. Second, the MW signal is too weak to excite the NV center. Last, the Mo electrode absorbs or blocks the incoming MW signal.

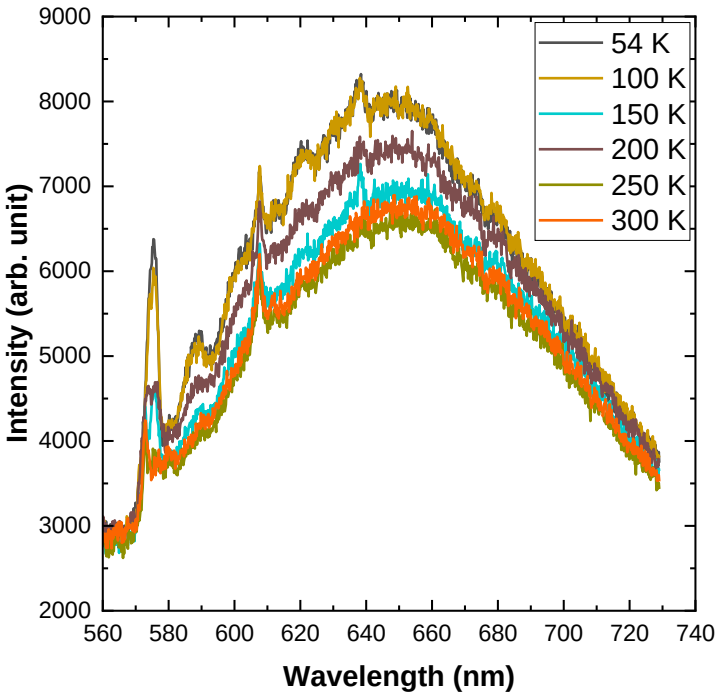

Figure 5-6 show the temperature-depended PL from 54 K to 300 K..

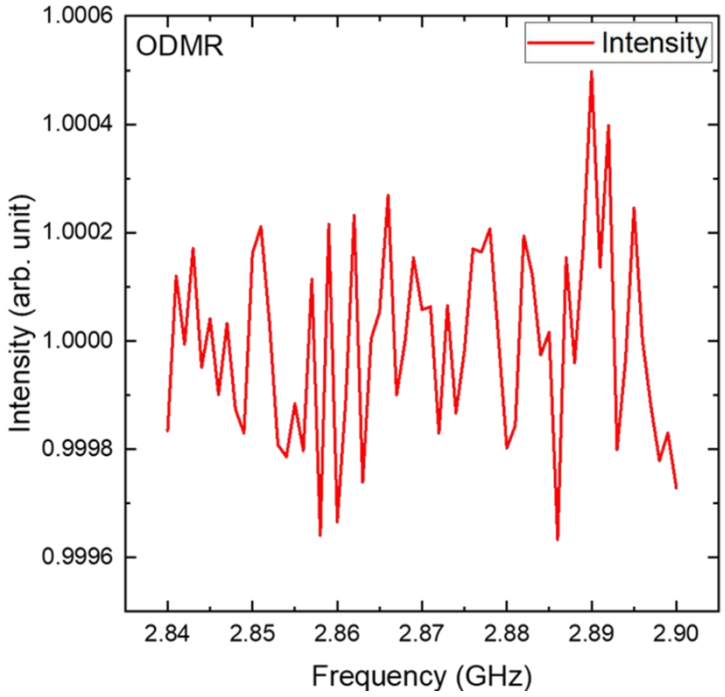

Figure 5-7 VDSDs at the 54 K ODMR graph. No resonance spectrum was observed.

5.5 Conclusion

At low temperatures, phonon scattering can be reduced and makes the PL spectrum characteristics of the NV center to become more obvious. Most of the experiments performed at cryogenic temperatures focused on the NV center that existed in the diamond substrate. It has been reported that the NV center's PL intensity and the ZPL highly depend on the surrounding temperature [5]. Reference [9] reported that there is a nonlinear shift of the zero field splitting (ZFS) parameter *D* spectrum for temperatures ranging from 5.6 K to 295 K. This shift can reduce the fidelity of quantum control. It will be interesting to study the behavior of NV^- under a constant electrical field at cryogenic temperatures.

For a cryogenic experiment, the sample should be placed inside a cryostat chamber. However, one of the challenges of the current chamber is that it does not have a proper line for MW delivery. A new MW signal delivery system was designed to wirelessly transfer the MW signal to the sample placed inside the cryostat. The system is has a transceiver and receiver based on a split-ring design. Moreover, when a wireless system is used, a fluctuation of heat can be avoided, compared to using a traditional wire-type antenna connector from outside the chamber [4]. An ODMR spectrum for the 1B diamond substrate was observed, and this proves that this wireless system works properly. However, when the experiment was performed on the VDSDs at cryogenic temperature, no ODMR desired results were obtained. This can be caused by the low NV center intensity, which is not enough for photon collection

compared with the 1B diamond substrate. The setup could work if the number of NV centers in the VDSDs were increased until a significant characteristic of NV centers could be observed (for example in figure 4-4 (a)). This wireless MW signal delivery system is a unique system for future low-temperature experiments.

5.6 References

[1] J. Dai and D. C. Ludois, "A Survey of Wireless Power Transfer and a Critical Comparison of Inductive and Capacitive Coupling for Small Gap Applications," *IEEE Trans. Power Electron.*, vol. 30, no. 11, pp. 6017–6029, 2015.

[2] Z. Mustapa, S. Saat, and Y. Yusof, "A new design of capacitive power transfer based on hybrid approach for biomedical implantable device," *Int. J. Electr. Comput. Eng.*, vol. 9, no. 4, pp. 2365–2376, 2019.

[3] S. Rajawat, M. Hübner, L. Kempen, and W. Lang, "Flexible passive LC resonator for wireless measurement during curing of thermosets," *J. Phys. Conf. Ser.*, vol. 1837, no. 1, 2021.

[4] G. Mariani, "Measurement systems for the control of the electron spins in nitrogen-vacancy centers in diamond at room and low temperature," University of Tsukuba, 2022.

[5] M. Yang *et al.*, "A diamond temperature sensor based on the energy level shift of nitrogen-vacancy color centers," *Nanomaterials*, vol. 9, no. 11, 2019.

[6] C. Schreyvogel, V. Polyakov, R. Wunderlich, J. Meijer, and C. E. Nebel, "Active charge state control of single NV centres in diamond by in-plane Al-Schottky junctions," *Sci. Rep.*, vol. 5, pp. 1–12, 2015.

[7] F. Jelezko and J. Wrachtrup, "Single defect centres in diamond: A review," *Phys. Status Solidi Appl. Mater. Sci.*, vol. 203, no. 13, pp. 3207–3225, 2006.

[8] M. W. Doherty, N. B. Manson, P. Delaney, F. Jelezko, J. Wrachtrup, and L. C. L. Hollenberg, "The nitrogen-vacancy colour centre in diamond," *Phys. Rep.*, vol. 528, no. 1, pp. 1–45, 2013.

[9] X. D. Chen *et al.*, "Temperature dependent energy level shifts of nitrogen-vacancy centers in diamond," *Appl. Phys. Lett.*, vol. 99, no. 16, pp. 1–4, 2011.

Chapter 6

Conclusion

6.1 Conclusion

The main objective of this thesis is to study the electrical control of NV center charge state created by ion-implantation technic by using vertical type Schottky diode. Ion-implantation is one of the best methods to create NV center inside the diamond lattice which can be observed by PL measurement in this study. By controlling the implantation kinetic energy, the penetration depth into the bulk can be control. Two charge states have been observed which is NV^0 and NV^-. An electrical control of the NV center was done to see the effect of reverse bias on the NV center charge state population and spin control of the vertical diamond Schottky. Electrical control is one of the promising methods to control the NV center on demand.

By applying reverse bias, it is possible to convert the NV center charge state from NV^0 to NV^- and vice versa. The changes in the NV center charge states are affected by the changes in the Fermi level that crosses the NV center charge transition level in the VDSDs depletion region. High NV^- concentration contributes to higher fluorescence which can increase the device sensitivity. By applying the MW signal to VDSDs, the NV center located directly under the transparent Mo electrode can be manipulated. The NV center is sensitive to its surrounding. In this case the NV center experience an electric field inside the diode depletion region which causes splitting and shifting of the energy level known as Stark effect. By calculating the split width, it is possible to determine the magnitude of electric filed experience by the NV center.

A wireless MW signal transfer also was developed for a cryostat. Normally a thin copper wire was used for MW delivery which is good if the setup is simple, and the experiment is carried out at room temperature. But when the experiment needs to be done at cryogenic temperature, or the cryogenic chamber dies not have proper line for MW delivery, a wireless system is one of the best options. In chapter 4, a wireless MW system has been developed to tackle this problem. The resonance spectrum from the 1B diamond substrate proved that the system could work well. At low temperatures, the phonon scattering was suppressed and the NV center ZPL is increased. The ZPL transition is where the electron can relax back without any disturbance from phonon vibration and can be used for applications. But when the wireless MW is applied to VDSDs, no ODMR spectrum was observed. The exact reason is still unclear. Perhaps the low collection of photon from NV center or the VDSDs electrode somehow ineterfere the MW signal.

6.2 Perspective and future work

Diamond now has become famous material among researchers as a quantum material. Compared to other quantum systems (eg, trapped ion, single electron transistor) that need to be cool down at cryogenic temperature, the NV center in a diamond can show its quantum properties even at room temperature. Being a solid-state material meaning that a standard nanofabrication process can be applied to diamonds for fabricating any kind of structure on top of it.

In chapter 4, it is proved that the NV center charge state can be manipulated by electrical control. It's also interesting to study the effect of the applied bias on the Rabi oscillation to see if it can affect the spin coherence time. The ODMR splitting due to the Stark effect maybe can be reduced if the sample [111] direction is used. Most of the reported applications are based on the NV^- that exists in the diamond substrate, but in this study, the NV^- is converted from NV^0 by electrical method thus it is interesting to see its effect when this NV^- is used to measure for example magnetic field, temperature, or any other parameters. Perhaps by fabricating the MW antenna directly on top of the device near the electrode by a photolithography method, it's possible to deliver the MW signal more efficiently. According to the reference, the NV center charge state can be manipulated because of the change in the Fermi level inside the diode depletion layer. But for the sample that was used in this research, the NV^0 PL spectrum is still visible even though Vr is applied until 40V. It is interesting to study why the NV^0 signal still appears eventhough the NV center located at 100 nm depth experiences an electric field in the depletion region. the assumption that we can make is that the continuous excitation laser ionizes the NV^- into NV^0 or perhaps because of Quasi-Fermi level interaction at the depletion region.

Currently, the most common way to read-out the NV center spin state is by optical read-out. In the future, by utilizing this device structure, it is possible to develop a new technique for NV center readout by using capacitance.

Achievements

Publications

[1] M. H. Bin Abu Bakar *et al.*, “Optically detected magnetic resonance of nitrogen-vacancy centers in vertical diamond Schottky diodes,” *Jpn. J. Appl. Phys.*, vol. 61, no. SC, 2022.

ACKNOWLEDGMENT

It is almost five years since I came to Japan and became a member of the Sakurai laboratory. A lot of things happened during this time and finally, I finished my Ph.D. journey.

Firstly, I want to express my sincere gratitude and appreciation to my supervisor, Professor Takeaki Sakurai for accepting me to be his Ph.D. student. He also helped me by applying for a scholarship so that I can come and live in Japan without worrying about monetary problems. Under his supervision, support, and ideas he guided me in the right direction so that I can do my best in my Ph.D. journey. Under his guidance, I obtained a new research skill that I can use in my future career.

I am also very grateful to Professor Traore for his teaching. I still remember when I first become a Ph.D. student, I do not know the technical matter and diamond power semiconductor material and it makes me struggle in my first year of the Ph.D. program. Professor Traore was very kind by guiding me in the correct direction such as giving tips on how to develop LabVIEW software and instrumentation that I used during my research and also teaching me about power semiconductor physics. Other than that, he also teaches me how to write a good journal article, and thanks to that I had published one journal. I also want to express my gratitude to Professor Monirul Islam for giving me advice so that I can improve my research. Also thank you very much to Professor Makino and Professor Yamazaki from AIST because providing me with samples for my experiment and idea on how to improve my research.

I also wanted to thank all my friends at Sakurai Laboratory. All of them a very supportive of me when I had trouble with my research and made our lab a happy place to be where we can talk about random stuff and always laugh together. I also want to thank Giacomo-san, for his help and opinion about my research. I will never forget the memories we made all these years. Other than my lab mates I also wanted to express my thank to all my Malaysian friends especially Ezral, Zul hilmi, Amir, Shakir, and Syahir. They always are there when I had trouble with my daily life, and give moral support and advice so that I can be strong to finish my Ph.D.

Finally, I would like to express my gratitude to the most important people, which is my family, especially my parents who sacrificed and give me support for me to get an education so that I can be a better person in the future.

I will treasure the beautiful memories that I made during my Ph.D. journey in Japan and I wish good luck to my lab mates in their research.

Muhammad Hafiz bin Abu Bakar
20 October 2022

List of Figures